Modeling and Verification of Valve Train Dynamics in Engines

by

M Husselman

Thesis presented at the University of Stellenbosch in
partial fulfilment of the requirements for the degree of

Master of Science in Mechanical Engineering

Department of Mechanical Engineering
Stellenbosch University
Private Bag X1, 7602 Matieland, South Africa

Study leader: Mr. K. van der Westhuizen
Dr. A.B. Taylor

December 2005

Declaration

I, the undersigned, hereby declare that the work contained in this thesis is my own original work and that I have not previously in its entirety or in part submitted it at any university for a degree.

Signature: ....
M. Husselman

Date: ....

Abstract

Modeling and Verification of Valve Train Dynamics in Engines

M. Husselman
Department of Mechanical Engineering
Stellenbosch University
Private Bag X1, 7602 Matieland, South Africa

Thesis: MScEng (Mech)
December 2005

This study involved the modeling and verification of the finger follower valve train arrangement with the focus on the non-linear behaviour of high speed valve springs.

The project was divided into three phases namely; the measuring of valve train dynamics, modeling of the valve train and the verification of the dynamic models by comparing the results from the two aforementioned two phases.

Acceleration and force were measured on a running engine. A force transducer was specially developed for this purpose. Digital signal processing was used in the analysis and implementation of all measured data.

The spring model was developed systematically from a solid model, into a finite element model, and finally into a dynamic model. All development steps were continually checked with experiments and calculations. The primary concept used in the spring modeling lends itself to modal analysis theory in conjunction with the superimposing of non-linearities onto a linear model.

The dynamic model was verified and good correlations were found, especially at high engine speeds where valve train dynamics play an important role. Parameter adjustments could be made in the dynamic model and the effect that some engine mechanisms, such as engine oil aeration, had on the valve train dynamics were identified.

The project was concluded with a case study of a cam profile optimisation project. Dynamic problems were found that would normally not have been identified without the dynamic model.

Uittreksel

Modellering en Verifiëring van Klep stelsel Dinamika in Enjins

M. Husselman
Departement Meganiese Ingenieurswese
Universiteit van Stellenbosch
Privaatsak X1, 7602 Matieland, Suid-Afrika

Tesis: MScIng (Meg)
Desember 2005

Hierdie studie behels die modellering en verifiëring van die hefboom volger klep stelsel rangskikking met die fokus gemik op die nie-liniêre gedrag van hoë spoed klepvere.

Die projek was opgedeel in drie fases naamlik; die meting van die klep stelsel dinamika, modellering van die klep stelsel komponente en die verifiëring van die dinamiese model deur vergelyking van die resultate van die twee eersgenoemde fases.

Versnelling en kragte metings was geneem op ’n werkende enjin. ’n Las sel moes spesifiek vir hierdie doel ontwikkel word. Daar was gebruik gemaak van digitale sein prosessering vir die analise van alle gemete data.

Die veer model was stapsgewys ontwikkel vanuit ’n soliede model in ’n eindige element model, en uiteindelik in ’n dinamiese model. Alle stappe was voortdurend deur middel van eksperimente en berekeninge geverifieer. Die primêre konsep wat in die veer modellering gebruik was, leen homself toe aan modale analise teorie in samewerking met die super ponering van nie-liniêre eienskappe op ’n liniêre model.

Die dinamiese model was geverifieer en goeie korrelasie was gevind, veral by hoë enjin spoed waar klep stelsel dinamika ’n belangrike rol speel. Parameter verstellings kon in die dinamiese model gemaak word en die effek wat sekere enjin meganismes, soos enjin olie lug inhoud, op die klep stelsel dinamika gehad het, was geïdentifiseer.

Die projek was afgesluit met ’n gevalle studie van ’n nok profiel optimering projek. Dinamika probleme is gevind wat normaalweg nie sonder die dinamiese model geïdentifiseer sou kon wees nie.

Acknowledgements

First of all, I would like to thank Dr. Taylor for his motivation, visionary guidance and continual support for all young aspiring automotive engineers. Without his persistence this project would be impossible.

The many specialist employees at Stellenbosch Automotive Engineering (CAE) always nearby and willing to assist in the many challenges faced in this project. These, almost daily, inputs from all engineering disciplines were unmistakably the backbone of this project.

The staff and artisans at SMD for performing all mechanical services, and Ferdie and Cobus Zietsman for their patience and assistance. Dr. Terry Terblanche and Ockert Strydom for assisting in my experiments by applying their skills and expertise in experimental techniques.

My study leader, Kobus van der Westhuizen, for his continual guidance and inputs. Also for his approachability, motivation and friendship.

Many friends, co-students and colleagues for their support and understanding.

Lastly, my mother and father for creating a study friendly environment at home, financial support, love and motivation. My sister and brother for their priceless friendship and love and a very special lady, Leah, for her support and motivation during the final stages of this project's documentation.

Dedications

I dedicate this to my beautiful mother. She redefines unconditional love and dedication to her family.

Contents

List of Figures

List of Tables

Nomenclature

A	Elastic body area
A_p^{vis}	Side area of the plunger
A_p^{base}	Area of the plunger base
a_n	Fourier series coefficient
a_0	Fourier series coefficient
b	Annular slot width
b_n	Fourier series coefficient
C	Spring index
$C_{1,2}$	Constants used when integrating the momentum equation
c	Speed of wave propagation used in wave equation
D	Mean spring coil diameter
D_i	Inner spring coil diameter
d	Spring wire diameter
E	Young's modulus of elasticity
E_{air}	Bulk modulus of air
E_{oil}	Bulk modulus of oil
E_s	Wheatstone bridge voltage source
E_0	Constant determining influence of oil pressure on bulk modulus of oil
e_s	Error using $\frac{1}{3}$ Simpson's rule for numerical integration
F	Total force acting on elastic bodies
F_{cc}	Coil clash force used in the multi-mass discrete model
F_{cv}^{prs}	Oil pressure force
F_{cv}^{vis}	Viscous friction force
F_0	Pre-load force exerted by spring in its compressed length

f	General sinusoidal frequency in Hertz
f_c	Cut-off frequency of windowed-sinc low-pass filter
f_d	Discharge coefficient of the check valve passage opening
f_e	Discharge coefficient of the check valve passage opening
f_n	Natural frequency in hertz
f_s	Sampling frequency
G	Young's modulus of rigidity
g	Gravitational constant
h	Subinterval size used in $\frac{1}{3}$ Simpson's rule and Taylor series
h_e	Boundary layer height at annular section S_e
h_g	Passage height of the gap
h_{oilres}	Boundary layer height at entrance of annular section on the oil reservoir side
$h(t)$	Valve displacement at retainer in terms of time
$h(\phi)$	Valve displacement at retainer in terms of cam angle
$\ddot{h}(\phi)$	Valve acceleration at retainer in terms of cam angle
I	Mass matrix, discrete mass model
I_g	Wheatstone bridge arm current
$I_{1,2}$	Wheatstone bridge currents
$ImX[i]$	Imaginary part of the Fourier transform of discrete signal $x[i]$
$ImX(f)$	Imaginary part of the Fourier transform of continuous function $x(t)$
i_g	Number of coils
J	Polar second moment of area
K_{total}	Single stiffness coefficient representing multi-mass spring model
$\bar{K}$	Stiffness matrix, discrete mass model
k	Spring constant
k_{cc}	Additional spring constant during contact between two neighbouring springs coils
L	Spring installed length
L_{BL}	Spring solid/blocked length
L_0	Spring free length

l	Length of elastic body
M	Number of points in the Windowed-sinc kernel, or kernel length
$Mag\,X[i]$	Magnitude part of the Fourier transform of discrete signal $x[i]$
m	Mass of spring
m_{cv}	Mass of check valve
N	Number of coils
N_a	Active number of coils
O'''	Order of third derivative
O''''	Order of fourth derivative
n	Mode number
$Phase\,X[i]$	Magnitude part of the Fourier transform of discrete signal $x[i]$
p	Fluid pressure
p_{hps}	High pressure chamber pressure
p_n	Fourier series coefficient
p_{oilres}	Oil reservoir pressure
$\dot{Q}_{moving}$	Volume flow rate between parallel plates due to a moving boundary
$\dot{Q}_{pas}$	Volume flow rate through the annular slot caused by the gap between the plunger and tappet
$\dot{Q}_{prsgrad}$	Volume flow rate between parallel plates due to a pressure gradient
$\dot{Q}_{cv}$	Volume flow rate through the check valve
q_n	Fourier series coefficient
Re	Reynolds number with regards to diameter
$ReX[i]$	Real part of the Fourier transform of discrete signal $x[i]$
$ReX(f)$	Real part of the Fourier transform of continuous function $x(t)$
$R_{1,2,3,4}$	Wheatstone bridge resistors
r_{cv}	Check valve ball radius
r_h	Check valve passage radius
r_p	Outside radius of plunger
S	Spring installation displacement
S_e	Annular section opened by check valve displacement
S_{oilres}	Annular section on the oil reservoir side

s	Static spring displacement
s_{cv}	Check valve displacement
s_{osc}	Oscillating amplitude
$\dot{s}_{cv}$	Check valve velocity
$\ddot{s}_{cv}$	Check valve acceleration
T	Torque acting on elastic bodies
T_p	Time period of continuous periodic signals
t	Time
U	Strain or potential energy
U_e	Fluid speed at annular section S_e
U_{oilres}	Fluid speed at entrance of annular section on the oil reservoir side
U_p	Plunger velocity
u	x-component of fluid velocity vector $\boldsymbol{V}$
V	Volume
$\boldsymbol{V}$	Fluid velocity vector
$V_{bc,db,dc}$	Wheatstone bridge voltage differences
V_{cv}	Volume of oil passing through the check valve
V_{pas}	Volume of oil passing through the annular slot caused by the gap between the plunger and tappet
V_{vol}	Volume of high pressure chamber
v	y-component of fluid velocity vector $\boldsymbol{V}$
w	z-component of fluid velocity vector $\boldsymbol{V}$
$X(f)$	Function of frequency and Fourier transform pair of time function $x(t)$
X_i	Distance of free space between two neighbouring spring coils
$x(t)$	Function representing signals or waveforms in the time domain
y	Displacement coordinate along the length of an elastic body or spring
$\ddot{y}$	Acceleration coordinate along the length of an elastic body or spring
β	Constant determining influence of oil pressure on bulk modulus of oil
β_i	Generalised coordinates
δ	Elongation of elastic body
ε	Strain

λ	Array of eigenvalues, discrete mass model
γ	Shear strain
μ	Dynamic deviation of spring particle
μ_{mix}	Viscosity of oil and air mixture
ν	Poisson's ratio
ω	General angular velocity, radians per second
ω_{cs}	Camshaft rotation frequency
ω_n	Natural frequency
ω_{osc}	Oscillating frequency
ϕ	Cam angle
ϕ_{air}	Volume fraction of air
ϕ_{oil}	Volume fraction of oil
ψ	Motion of any particle at distance y
ρ	Density
ρ_{air}	Density of air
ρ_{oil}	Density of oil
σ	Stress
τ	Shear stress on elastic bodies
τ_p	Plunger shear stress

Acronyms

AMA	Acoustic Modal Analysis
CAD	Computer Aided Design
CAE	Computer Aided Engineering
CST	Constant Strain Triangle
DFT	Discrete Fourier Transform
DSP	Digital Signal Processing
d.o.f.	degrees of freedom
EMA	Experimental Modal Analysis
FE	Finite Element
FEM	Finite Element Method
FFT	Fast Fourier Transform
FRF	Frequency Response Function
FWT	Force Washer Transducer
HLA	Hydraulic Lash Adjuster
IC	Internal Combustion
IGES	Initial Graphics Exchange Specification
KVL	Kirchhoff's Voltage Law
LST	Linear strain triangle

LVDT	Linear Variable Differential Transformer
MPC	Multi point constraint
OHC	Overhead camshaft
RBE2	Rigid Body Element, type 2
RBE3	Rigid Body Element, type 3
SAE	Society of Automotive Engineering
SCF	Single component force
SI	Systeme International
VVT	Variable valve timing
VVL	Variable valve lift

Chapter 1

Introduction

When designing valve train systems there is generally a conflict between the demand for fast opening and closing valves, which means large valve accelerations, and the requirement of limiting loads, which means small accelerations. To optimise the design within these constraints, one has to consider several aspects of the valve train; moving mass, kinematic characteristics, and dynamic characteristics of the components such as the hydraulic lash adjuster and the valve spring.

Keeping the moving mass and the kinematic characteristics of the valve train components in control is relatively simple compared to the design and analysis of the valve train dynamics. The cam profile is the primary input parameter which determines the valve train dynamics and each time its lift curve's shape is altered, the valve train dynamics are bound to change.

It was during such a development project that the impact which the alteration of the cam curve had on the dynamics of the valve train was questioned. The ability to analyse the valve train dynamics cost effectively and in house did not exist at that time and the need for this project was identified. In short the project objectives were to develop a dynamic valve train model and verify its accuracy through experiments.

It became clear early on that the primary valve train components were the *Hydraulic Lash Adjuster* (HLA) and even more importantly, the valve spring. The valve spring had the lowest stiffness and the lowest natural frequency of all the components in the valve train. Additionally the dynamic response of the valve spring is substantially different from its static response due to its internal dynamics.

The most prominent behaviour of valve springs is their non-linear stiffness, primarily caused by contact between neighbouring spring coils. When contact occurs, the spring's number of active coils reduces and causes a change in stiffness. Coil contact under dynamic conditions is referred to as coil clash and occurs when external excitation cause waves progressing through the spring with amplitudes high enough for adjacent windings to touch. This causes undesired force responses and also has a negative impact on the durability of the spring.

The focus of this project was directed at the accurate modeling of high speed valve springs with the objective to capture its non-linear behaviour. Similar attention to the dynamic behaviour of the HLA was given as it was found that its influence on the dynamics of the valve train system could not be ignored either.

Previous work done in the field of modeling valve train dynamics could be divided into two classes. The first class includes purely mathematical models and forms the majority of research done in the past. These models capture most of the dynamics of valve springs, but exclude non-linearities. Only the most recent mathematical models include non-linearities, but incorporate them by using discretisation techniques and numerical methods.

The second class includes highly sophisticated and expensive software packages. These packages are normally based on well known mathematical models and concepts, but also include dynamic, non-linear finite element theory and iterative processes. These models are cutting edge, but financially impractical for most organisations.

The model developed in this project made use of the latest concepts in mathematical models and incorporated it into a basic software package. Thus, by understanding the dynamics of springs, a sophisticated model was created and constructed in a relatively simple software package.

With regards to the experimental work done in this project a major limitation was found with valve train dynamics measurement devices. Measuring valve train dynamics entails measuring relatively large information amplitudes (e.g. large forces, accelerations, etc.), with small sensors (small spaces available) in harsh environments (e.g. high temperatures, oils, etc) at high speeds (e.g. cam events at 6000 rpm lasts 20 ms).

Previous investigators measured accelerations and forces, amongst others, with success and these were decided to be the measured parameters for this project. Although commercially available accelerometers could be used, a force measurement transducer had to be developed specifically for this project. It was called the Force Washer Transducer, or FWT, and was used successfully up to maximum engine speeds and formed the basis of this project's experimental work.

Comparisons were made between the measurements from an actual engine and the results from the dynamic model. Good results were found, especially at high engine speeds where valve train dynamics play an important role. The successful verification of the dynamic model led to illustrating its capabilities by applying it to a case study.

The study was based on an actual project involving cam profile optimisation. Dynamic problems were found that would normally not have been detected without the use of a dynamic model. This demonstration of the dynamic model's capability fulfills the project's original needs.

Chapter 2

Project Overview

This project could be divided into three phases; valve train measurements, valve train dynamics modeling, and valve train dynamic model verification. The following sections discuss an overview of the project in light of these phases.

2.1 Valve train dynamics measurements

The first experiment performed was a quasi-static compression of the spring. This was used to characterise the first spring parameters needed in the dynamic modeling process. Much time and effort was then put into the design and development of a valve train test rig that was intended to operate without combustion and driven by an electric motor. The quality of the measurements sampled on this mobile test rig was disappointing and these experiments were abandoned and replicated with measurements taken on a complete running engine in a conventional engine test cell.

Two experiments were planned to be performed on the test engine. Firstly, accelerations were measured with commercially available accelerometers and these experiments were relatively simple.

Secondly, spring reaction forces were measured at the seating location of the spring. No suitable transducer could be found for this specialised measurement and a force transducer was developed specifically for the use in this project. It was used up to maximum engine speed with success and produced good measurements which were used as the basis of the model verification process.

Measuring high speed dynamics in a noisy environment, particularly measuring accelerations, made data processing a necessity. Although hardware filters were used, the primary data processing was done with *Digital Signal Processing* (DSP) theory. Numerous mathematical programs were written to analyse measured data. Amongst these were Fourier analysis programs and a digital low pass filter.

Fourier theory were applied to calculating cam profile harmonics and performing frequency spectrum analysis on the measured data. The spectral information was used to determine cut-off frequencies used in the design of the digital filter.

2.2 Valve train modeling

Although commercial software packages were used extensively in this project, mathematical models were also investigated and applied in order to understand the dynamics of the valve spring and HLA.

Three models are discussed. Firstly a brief description of the simplest model, the dual mass spring model, is given.

Secondly, the surge model, based on the wave equation, is discussed in detail. This model has been used by many investigators with success and forms the basis from which much research has been done. This model includes the use of modal analysis and is therefore also popular in modern software packages. The model is illustrated with a simple example calculation and its shortfalls are pointed out.

Thirdly, the multi-mass discrete model is discussed and is referred to as the basic concept of the dynamic model used in this project.

A detailed model of the HLA and its functioning were studied and dissected. During this study it was found that the properties of the HLA influenced the dynamics of the entire valve train system and could not be treated as a rigid body. Some simplifications of the model were made in order to implement the HLA into the dynamic model of this project. By understanding the intricacies of the HLA, these simplifications could be evaluated and confidently judged. Some interesting dynamic phenomena of HLA is also discussed.

After the review of existing mathematical valve train models, as well as that of the HLA, was concluded, attention was focussed on the valve spring. The basic equations for spring stiffness and natural frequencies were derived from first principles and with this the fundamental natural frequency of the spring was calculated. This value was later successfully confirmed with the spring model developed in this project.

What follows is the core of the project; the actual valve train model development. The modeling process was again divided into three phases; ProEngineer was used for all solid modeling of all the components, MSC PATRAN/NASTRAN was used for the *Finite Element Method* (FEM) modeling of the valve spring and MSC ADAMS was used for the construction and development of the complete valve train dynamic model. (Pro-Engineer is essentially a Boolean-based solid modeling package. MSC PATRAN is a pre-/post processor (*Finite Element* (FE) modeling) package used in conjunction with MSC NASTRAN. MSC NASTRAN is the FE solver package and all elements chosen in the MSC PATRAN environment during modeling are from the MSC NASTRAN element library. All analysis result files are MSC NASTRAN files. MSC ADAMS is a dynamics and mechanisms analysis package.)

The solid modeling is briefly described and consists of work done creating the valve train components in the three-dimensional environment of *Computer Aided Design* (CAD). This discussion leads to the second phase of the modeling process, referred to as the FEM model.

It should be noted that a FEM model was developed for the valve spring only. Some simplifications were made in order to define the scope of the project more clearly of which the most important was that valve spring dynamics would form the primary objective of this study. All the other components, with the exception of the HLA model, were modeled as solid, rigid components.

The spring FEM model was first developed as a detailed model of which the results were used to construct a more efficient model, referred to as the "equivalent model". The detailed model was developed with meticulous geometric accuracy. A specific element mesh was planned with boundary conditions, modeling of contact, and integration into the dynamic model being kept in mind. The detailed model was characterised through the results of the quasi-static spring compression and confirmed with the theoretical calculation of the spring's fundamental natural frequency.

The equivalent model was constructed through discretising the detailed model and extracting force-deflection relations from it for each of the 22 spring elements that resulted. These force-deflection relations were extracted from a MSC NASTRAN analysis output file with the aid of a data processing program written specifically for this purpose.

The one-dimensional equivalent model was numerically much smaller, more efficient and less sophisticated than the detailed spring model, but contained identical dynamic characteristics. By confirming the accuracy of the equivalent model through direct comparison, the equivalent model was integrated into the dynamic model.

Once the FEM modeling process was completed, the development of the dynamic model commenced. Firstly, the detail operation of the actual engine valve train system is discussed, whereafter the simplifications made to implement it into a dynamic model follows.

A mathematical model of the HLA was incorporated into the dynamic model and proved to be essential for the successful correlation of measured data to the dynamic models. Therefore one of the most important features of the dynamic model was the capability of oil aeration variation. The FEM spring models were developed with the spring in its free, uncompressed length and the approach taken to include it into the dynamic model as compressed is discussed. The dynamic model is then summarised and the model verification process commenced.

2.3 Valve train dynamic model verification

Once the dynamic models and experimentation were completed, model verification commenced. The first step taken in the model verification process was to illustrate the effects the building complexity of the spring model had on the valve train dynamics. It is shown that all spring mechanisms were necessary to find a good model-measurement correlation.

The dynamic model had various parameters that could be modified until good measurement data correlation was reached. The valve train dynamics were particularly sensitive to alteration of the percentage of oil aeration of the HLA. Contact stiffness, -restitution and -damping values between contacting surfaces could also be optimised. The measurements to be compared first were the acceleration measurements. From this first initial comparisons, all spring internal damping had to be eliminated in order to have good correlation.

Secondly, the *Force Washer Transducer* (FWT) measurements were compared with force calculations from the model. Excellent comparisons were found at high engine speeds, which is the more important valve train operating range. Eventually, a good overall approximation was found.

Finally, the model's capability was illustrated by performing a case study on an actual commercial engine project. The effect that the alteration of the cam profile had on the valve train dynamics are investigated and back to back comparisons were modeled. Dynamic problems were identified which would not have been identified without the bebefit of the dynamic model.

Chapter 3

Valve Train Dynamics Measurements

The scope of this project included the verification of valve train models by measuring the valve train dynamics experimentally. These measurements are often limited to the measurement of valve displacement or strain in rocker and camshaft bearing caps. Some investigators have directly measured velocities and/or accelerations at various points in the valve train.

Bakonyi (1968) measured velocities of the valve head in motored *Overhead camshaft* (OHC) engines and numerically differentiated and integrated to obtain valve acceleration and displacement respectively. Taylor & Campbell (1989) attached a piezoelectric accelerometer to the rocker arm and obtained acceleration measurements in a running diesel engine. Roskilly (1986) measured the acceleration of the valve head in a motored engine and Seidlitz (1991) attached nine accelerometers to various parts of the valve train as well as strain gauges on the pushrods and springs in a motored engine. Kreuter & Maas (1987) measured forces, valve acceleration and hydrodynamic oil film thickness in a motored engine and observed that forces and accelerations are the most important criteria to evaluate valve train dynamics.

References to the above investigators have shown the advantages of acceleration measurements for dynamic analysis. There are two fundamental reasons for this:

1. Accelerometers typically have broader bandwidth than velocity transducers, displacement transducers or strain gauges, and
2. higher derivatives of a function tend to exaggerate the system's dynamic behaviour.

It was thus decided to verify the valve train dynamics through two measurements; valve accelerations and spring force measurements. The spring force measurement was performed with a specially designed force transducer, while the valve acceleration measurement used commercially available sensors and also necessitated rthe use of DSP theory in the project.

At first it was decided to perform the measurements in a non-combustion environment. For this purpose, a cylinder head test rig was designed and built. Unfortunately the results were undesirable and this measurement procedure was exchanged for a running engine setup on a dynamometer test bed. In addition to accelerations measured in a running engine, the spring force measurement was also performed on the same engine under identical operating conditions.

The first experiment though, was a quasi-static compression of the spring used to verify the flexible spring model. The following sections discuss the above experiments in detail.

3.1 Static spring deflection

The first experiment of verifying the spring characteristics was the static spring deflection test. This experiment was relatively simple and quick and was used as a basis to verify the FE model's geometry and material specification, such as the Young's modulus of elasticity and the Poisson's ratio.

Two similar valve springs were sampled. Each spring's force and displacement data were measured for one compression and expansion stroke resulting in 4 sets of data. The expansion of the spring was measured to gain extra data that could be used to average the effect that the measurement equipment might have on the measurement accuracy.

The springs were compressed in an Amsler tensile test machine. The load was measured with a 1 ton $DMD20$ load cell and the displacement was measured with a *Linear Variable Differential Transformer* (LVDT). The data was amplified and calibrated using an HBM bridge amplifier. The load cell was calibrated to display 1 N/mV and the LVDT was calibrated to display 1 mm/0,1 mV. The data was captured with an Eagle 30F I/O card sampling at 32 Hz. Figure 3.1.1 graphically illustrates the test setup.

The data was sampled for two minutes to allow slow compression and expansion in order to represent a quasi-static process. Therefore all dynamic effects could be ignored. Figure 3.1.2 illustrates the result of the two spring compression tests.

After completion of this first experiment, the development of the FEM model could be started (section 6.4). The next experiment planned was the measurement of the valve

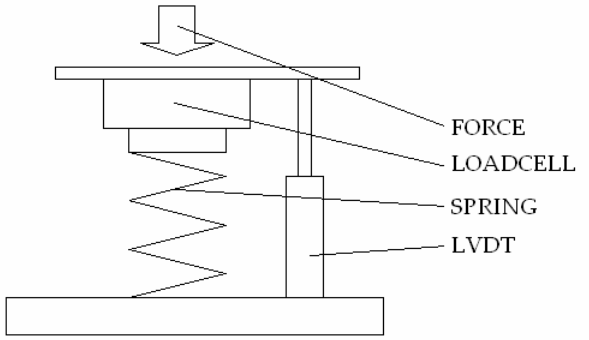

Figure 3.1.1: Spring static compression test rig and setup.

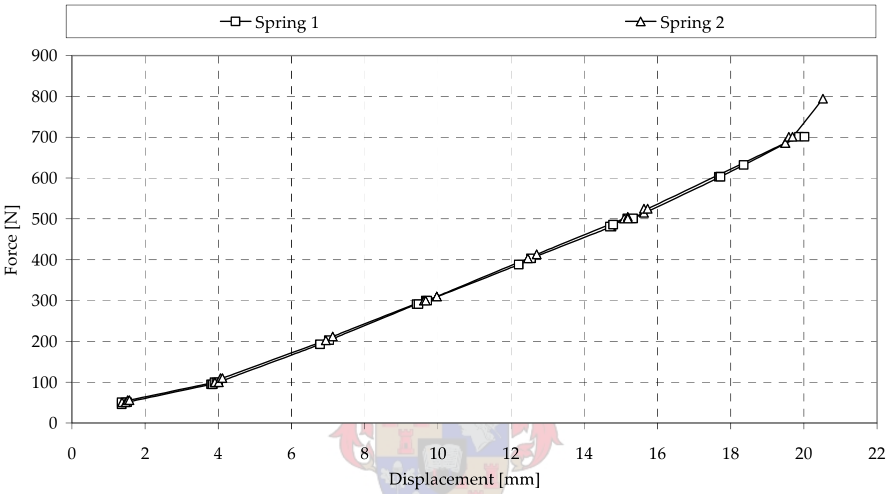

Figure 3.1.2: Spring static compression measurement results.

spring forces and the valve accelerations. The next section discusses the development of the cylinder head test rig, which was initially planned to be used to perform the aforementioned measurements.

3.2 Cylinder head test rig

Both the valve spring forces and the valve accelerations were initially planned to be measured on a non-combustion cylinder head test rig specifically designed for this project. In short, this approach was abandoned due to the unsatisfactory acceleration data measured. Nonetheless, the cylinder head test rig is briefly discussed here and concluded with possible reasons for the failure of the experiment and also suggested improvements necessary for future work on the test rig.

The reasons for initially using a non-combustion cylinder head test rig were:

1. Measuring the friction of the valve train was possible with a non-combustion test rig which contained the cylinder head only, as will be discussed shortly,
2. the test rig as an integrated system would be less technically demanding than a combustion driven engine. A fully integrated running engine needed engine and dynamometer control systems, fire safety systems, cooling and fuel systems, exhaust systems, etc.,
3. the cylinder head would be electrically driven and the noise and vibration caused by combustion and other accessories would not influence the measurements,
4. sensor placement was more favourable with an exposed cylinder head face, and
5. the less harsh environment meant greater sensor durability.

As illustrated schematically in figure 3.2.1, the cylinder head test rig consisted of the cylinder head, an electric motor and speed controller, external oil circuit including an hydraulic oil pump, oil sump, oil pressure gauge and a 3-way valve, and various sensors and data acquisition equipment.

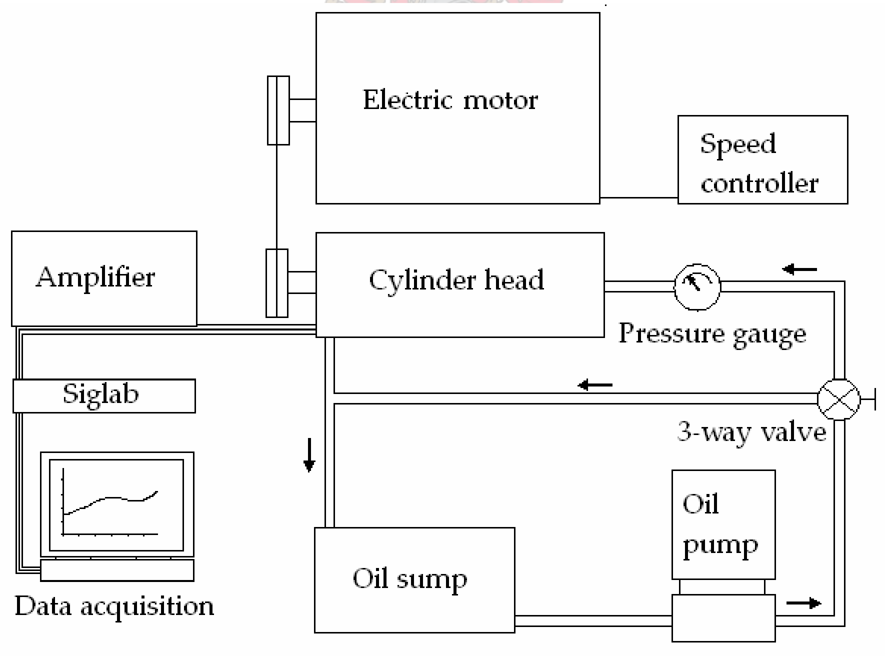

Figure 3.2.1: Valve train test rig schematic lay-out.

The fact that the Ford cylinder head had an internal cam chain, instead of the more common external cam belt, complicated the design of the test rig. The reason for this was that in the case of an external cam belt system, the cam drive mechanism runs dry and the lubrication system is separated from it. In the case of the internal cam chain, the oil return from the cylinder head flows over the cam chain back into the sump.

To accommodate this valve train drive arrangement a sump was designed to encapsulate the cam chain and electric motor sprocket. This then also served as the oil return sump schematically represented in illustrated in figure 3.2.2.

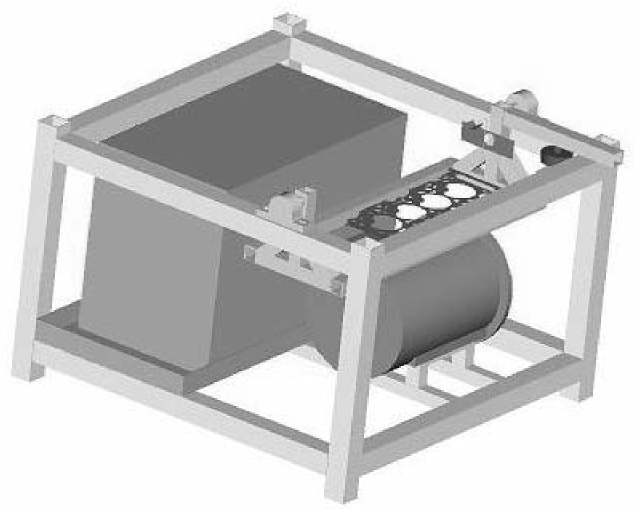

Figure 3.2.2: Test rig arrangement of main components.

As mentioned earlier, the principle reason for choosing this testing procedure was to measure the friction of the valve train system. If the torque needed to drive the camshaft could be measured, the dynamic model could be developed further by including friction between contacting metal surfaces, as for example the hydrodynamic bearings of the camshaft.

Torque was measured through a load cell that was loaded by a lever arm. The lever arm was part of a swivel bed onto which the cylinder head was bolted and driven by the electric motor. For convenient torque calculations, the point of rotation of the lever arm and swivel bed coincided with the centre axis of the camshaft. The torque necessary to overcome the camshaft friction was thus simply the force measured at the load cell multiplied by the lever arm length. Figure 3.2.2 also illustrates this concept and the placement of the swivel bed.

Two other sensors were used to capture additional data. PCB accelerometers, weighing three grams each and capable of measuring 500 g, were located on the valve face of the intake valve of cylinder one and four respectively. A standard Ford camshaft phasing sensor was used to measure and record camshaft rotation speed accurately. The latter measurement was also used to distinguish between different cam events.

An HBM bridge amplifier was used to amplify the signal from the load cell. A DSP Siglab spectrum analyser unit was used to power the accelerometers and capture the data from all four sensors including the load cell, cam phase sensor and the two accelerometers. All measurements were recorded at 25,6 kHz to ensure the recording of at least four cam events.

The test rig design had one flaw: At first, the 5,5 kW electric motor did not seem powerful enough to drive the camshaft. The electric motor would open the valve sufficiently, but during the valve event, severe valve acceleration oscillation was measured. It became clear that the electric motor was being accelerated and decelerated by the closing and opening of the valves throughout the valve train system. These accelerations would superimpose throughout the remainder of the valve event and cause a dramatic closure of the valve. This increased valve closing velocity and valve closing impact forces. Unrealistic accelerations and valve bouncing resulted. Even at low engine speeds, the accelerometers were over-loading (saturating) upon valve closing. These higher valve impact forces caused vibrations to ripple through the cylinder head and test rig and the acceleration data captured was noisy to the extent that it did not represent any acceleration curves.

This problem however was not caused by an insufficient electric motor power, but it is believed that the electric motor has less inertia than the completely assembled engine. This was also worsened by the fact that the standard cam chain and cam chain tensioning mechanisms could not be used.

Figure 3.2.3 illustrates a comparison between the kinematic valve lift profile and one of the result sets measured at 1000 rpm. The raw data, sampled at 25,6 kHz, was filtered with a Windowed-Sinc low pass filter with a cut-off frequency of 896 Hz. (This filter and other DSP related theory such as the *Discrete Fourier Transform* (DFT) are discussed in appendix A.)

The kinematic profile was calculated by performing a three-point forward difference formula calculation (based on the Taylor series expansion) on the discrete valve lift data. (Refer to appendix B for brief overview of this three-point forward-difference formula.) The valve lift data was found by constructing a simple kinematic ADAMS model that only incorporated the dimensions of the valve train system. No dynamics were included

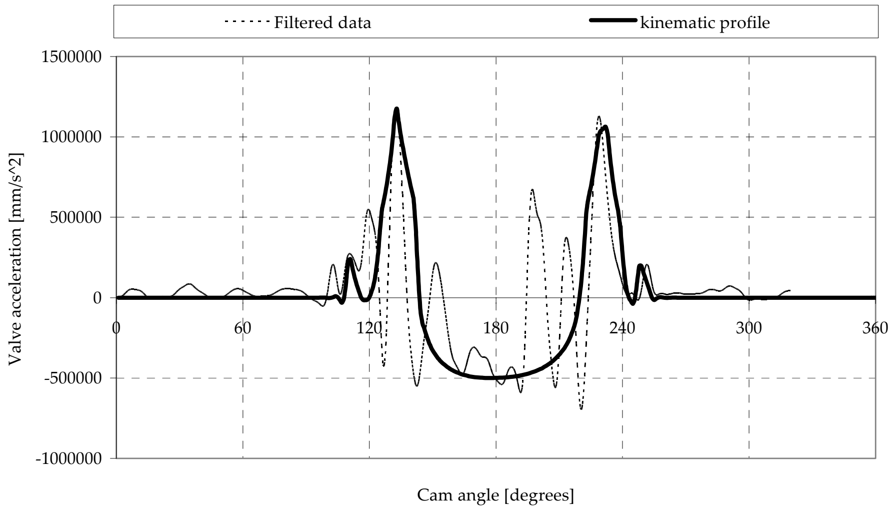

Figure 3.2.3: A comparison between the kinematic and measured valve acceleration data at 1000 rpm.

in this model.

From figure 3.2.3 it can be seen that some correlation between modelled and test data exists. Both lift-off and seating acceleration peaks correlate well, as well as the maximum acceleration peaks. The negative acceleration phase however contains large oscillations. These oscillations were expected, when considering valve spring oscillation in this area, but the amplitude of the oscillations are too severe.

With further data analysis, it is believed that some sense could be made from the test rig's measured data. However, at this point in time, the project was reviewed and the test rig testing procedure was abandoned with the aim to use a complete running engine. Unfortunately, valve train friction could not be measured in this situation, but it was felt that a much more realistic engine operation justified the change of the project objective and direction.

In case of future use of the cylinder head test rig, the angular momentum of the electric motor could be increased by adding a flywheel to the cam drive system. Ideally, the electric motor rotor and test rig flywheel assembly should have identical moment of inertia as that of the standard Ford crankshaft and Ford flywheel assembly. This should minimise speed fluctuation and result in more realistic valve closing behaviour.

3.3 Valve acceleration measurements in running engine

After valve acceleration measurements on the cylinder head test rig were abandoned, performing these measurements on a running engine was investigated. Unfortunately, the accelerometer could not be positioned on the valve head anymore, but was rather located on the follower above the valve tip. This location caused the accelerometer to move in a slightly arced path with the radius of the arc defined by the follower's instantaneous lever length. Thus, the acceleromoter had a two dimensional movement compared to the one dimensional movement of the valve. This difference was insignificant, because the virtual sensor created in the dynamic model, was located at the identical position as the actual sensor during the experiment. Therefore a direct comparison could be made between measured and modelled values.

A PCB accelerometer identical to the ones used on the cylinder head test rig was used. This accelerometer weighed three grams and was placed onto the finger follower, directly above the valve tip (refer to figure 3.3.1). In order to fasten it securely to the follower, a small piece of mild steel was welded onto the follower and a hole drilled and tapped through it. Excess metal was machined away to minimise the weight of the follower. The accelerometer was screwed into the small block of mild steel and a plastic washer was inserted in between. The total additional mass added to the follower was 5,6 grams.

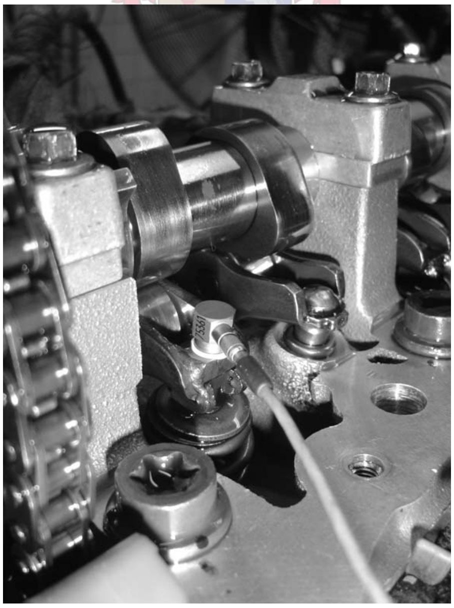

Figure 3.3.1: Accelerometer placement on finger follower in running engine.

Again the camshaft phasing sensor was used to calculate the exact engine speed at the time of measurement. It was also used to recognise specific cam events individually within a set of measured data.

All measurements were performed with the Siglab spectrum analyser and measured at the maximum hardware sampling frequency of 51,2 kHz. An anti-aliasing filter was used. Unfortunately again, the accelerometer was over-loading (saturating) severely above 3000 rpm and only three good measurements were recorded at 1000 rpm, 2000 rpm and 3000 rpm respectively.

The first step was simply to look at the data in the time domain. Figure 3.3.2 illustrates how noisy the original measured data was. This data was imported into the MATLAB program written to analyse all measured data. The program's first calculation was to multiply the original data with the Hamming window to improve the frequency resolution by minimising spectral leakage.

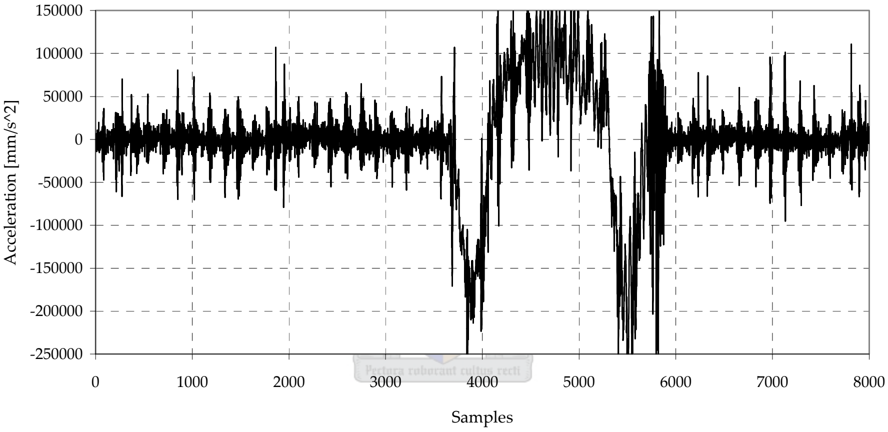

Figure 3.3.2: Original follower accelerometer data with high noise content at 1000 rpm engine speed.

Next, the frequency domain of the acceleration data was then calculated with the DFT. (Refer to section A.1.2 for a brief overview on DFT theory.) After that the frequency domain was converted into polar notation. The complete frequency range is illustrated in figure 3.3.3.

By looking closer at these frequencies in the frequency domain (figure 3.3.4), it is noted that throughout the entire frequency domain a signal with a relatively flat region is present, just below a normalised amplitude of 0,05 · This is called white noise because

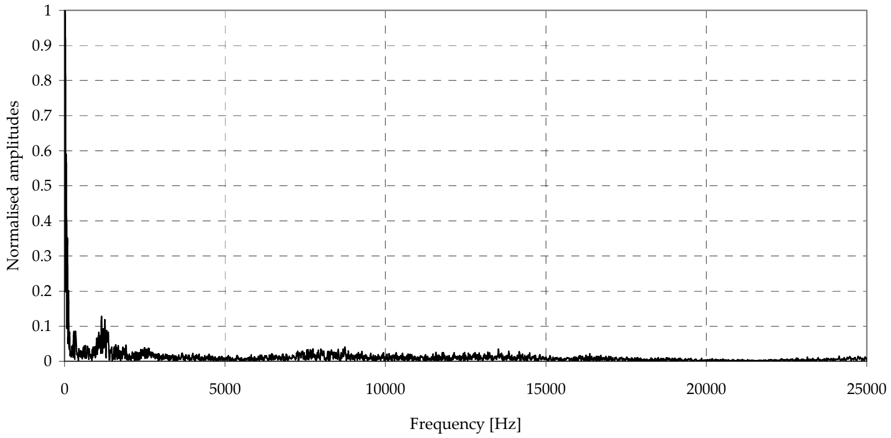

Figure 3.3.3: Complete DFT frequency domain of acceleration data at 1000 rpm engine speed.

it roughly contains an equal amount of all frequencies, the same as white light (Smith (1999)). The white noise could be originating from fuel combustion noise, other mechanical components in the engine, electrical interference noise, ground vibrations from other test cells in close proximity, etc.

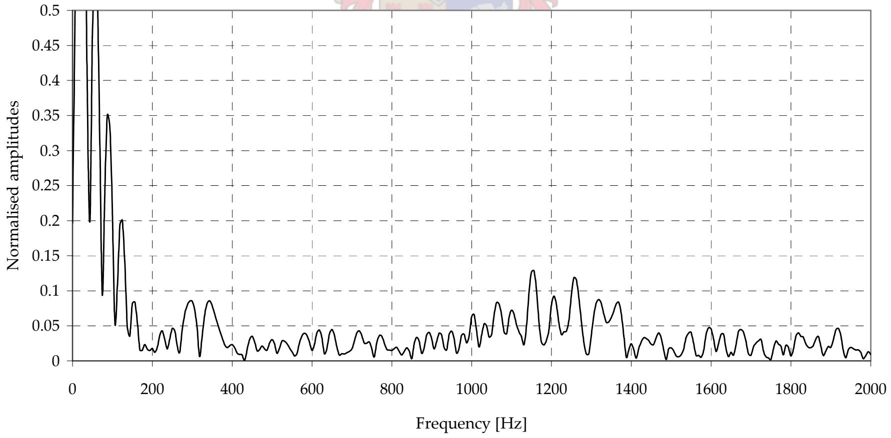

Figure 3.3.4: Enlarged DFT frequency domain of acceleration data at 1000 rpm engine speed.

However, certain frequencies add considerable amplitude to the frequency domain and these frequencies correlate well with calculated spring mode shapes. Table 6.4.1 and figure 6.4.11 show that the modelled first, second and third order of spring natural mode shapes were approximately between 440-530 Hz, 870-990 Hz and 1000-1400 Hz respectively. Unfortunately the modelled first order mode shapes did not correlate that well with the measured frequencies, but the second and third order mode shapes did.

It should be noted that the spring mode shapes were calculated with the spring decoupled from the complete valve train system. As discussed in section 6.5 with reference to Schamel (1989), decoupling the valve spring from the valve train system does not have a significant effect on the dynamics and this difference is negligible. Secondly it should be noted that the resonant frequencies mentioned above were computed on a free, uncompressed spring. (More about these calculations in section 6.4.) With these differences between modelled and measured spring set-ups, slight frequency ambiguities could be expected.

With the frequency analysis completed, it was possible to determine suitable cut-off frequencies in order to avoid high frequency noise. This information was used to design the Windowed-Sinc low pass filter for this application. It was also possible to verify the correlation between measured and modelled resonance frequencies. To do this, the filter was set to a cut-off frequency of 200 Hz, 600 Hz and 1400 Hz respectively. The aim was to identify the influence the individual spring mode shapes had on the acceleration data's vibration content. Figure 3.3.5 illustrates this.

Figure 3.3.5(a) illustrates frequencies below the first spring mode shape. It is clear that no resonant frequencies were present. Figure 3.3.5(b) includes the first spring mode shapes. It is clear from this figure that a first order resonance vibration is present. Figure 3.3.5(c) includes both the second and third order spring mode shapes as well. It is clear that a higher order mode shape is superimposed onto the first order vibration.

Again, the influence of white noise is present, but it became clear that when frequencies in the order of the modelled spring mode shapes were added to the measured acceleration signal, significant vibration amplitudes were added. The correlation between modelled and measured resonant frequencies is thus verified.

All three engine speed acceleration measurements were analysed with the MATLAB program and similar results were obtained. With these analysed acceleration measurements the dynamic model could be verified and this is discussed in chapter 7.

3.4 Measurement of valve spring forces

In order to validate the dynamic spring model's forced response, the capability to measure forces within the spring needed to be developed.

One method of measuring spring forces being used is applying strain gauges directly to the spring wire. This has two disadvantages (Schamel, 1993):

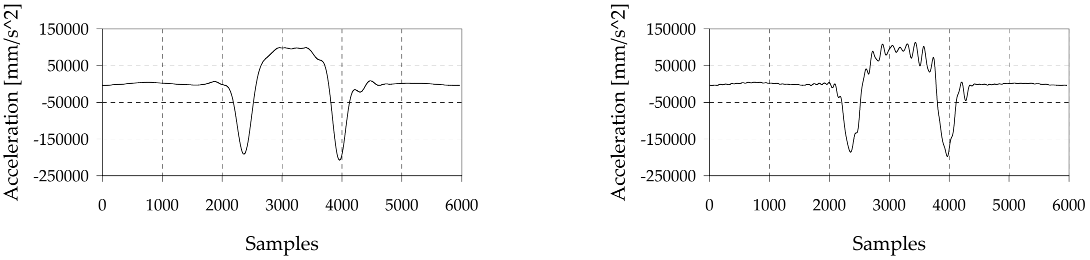

(a) Acceleration frequencies below 200 Hz (Below first order spring mode shapes).

(b) Acceleration frequencies below 600 Hz (Above first order spring mode shapes).

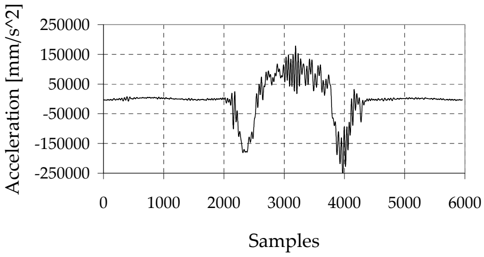

(c) Acceleration frequencies below 1400 Hz (Above third order spring mode shapes).

Figure 3.3.5: Acceleration measurements after filtering at various cut-off frequencies.

1. It is difficult to determine the correct location relative to the surge modes of the spring, and
2. strain gauging of the wire does not show whether severe clashing of the spring coils occurs. Once a coil rests on the next one, there is no more increase in strain and no additional information on the spring dynamics are available beyond this point.

Another more acceptable method is to measure the resultant spring seat force. A force transducer, to be located between the spring and cylinder head, was required. Commercially available force transducers were too thick to fit underneath the spring. The main spatial constraint being the amount of material that could be removed without cutting into the inlet ports or engine coolant jackets. Thus, a special transducer was developed from a concept used by General Motors Corporation (Schamel (1993)).

3.4.1 Development of the Force Washer Transducer (FWT)

The transducer roughly consists of a washer (hence the name FWT) with four ribs on the circumference, separated by slots every 90 degrees apart. If the device is loaded each quarter section of the washer acts as a bending beam. This bending is then measured with a full bridge strain gauge arrangement and calibrated through static spring compression, to be discussed in section 3.4.3.

The complex geometry of the transducer's bending ribs, as well as the stress concentrations that exist in the various small radii of the transducer, made initial hand calculations complex and justified using *Computer Aided Engineering* (CAE) techniques directly. ProEngineer and PATRAN/NASTRAN were used to model the FWT with the primary objective being to keep the transducer as thin as possible.

Results from the first realistic dynamic model's results (section 7.3) showed that the maximum spring seat force varied from approximately 560 N to 595 N from 1000 rpm to 6000 rpm engine speed respectively. Physically, the spring loaded the cylinder head asymmetrically due to the ground-off ends of the helical spring. The asymmetry of the spring's bottom surface resulted in an area segment of approximately 45 degrees not being loaded. This posed a problem in the sense that poppet valve springs rotate under normal engine operation. After calibrating the FWT at one spring position, slight rotations of the spring could result in entirely inaccurate measurements. To solve this problem, a second washer was designed and referred to as the *force spread washer*, illustrated in figure 3.4.1. As the name implies, this washer only spreads the uneven spring force evenly onto the FWT.

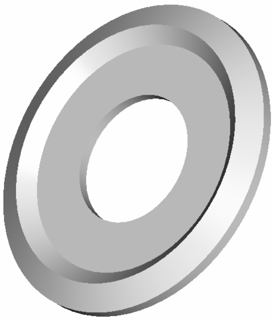

Figure 3.4.1: Force spread washer.

With a maximum calculated spring seat force of 595 N at 6000 rpm, each rib is loaded by a maximum distributed load of approximately 150 N. A safety factor of 1.6 was eventually chosen, resulting in a design criteria of 240 N per rib without material failure. The

FWT has symmetrical ribs and this enabled the modeling of only one half rib, i.e. one eighth of the complete FWT, and loading it with 120 N. This load was applied as a NASTRAN *Total Load*, distributed evenly over the spring's contact area, directly onto the tetrahedral elements' free faces. Tetrahedral elements are generally used for solid elements using auto mesh functions.

Stainless steel EN57 (E = 207 GPa and ρ = 7,80 × 10^{-6} kg/mm^3) was selected as the sensor material. EN57 has excellent linear material properties and is ideal for the application of measurement instruments Callister (1996). A yield strength of 207 MPa was assumed and used as the yardstick for optimising the design.

In order to exploit the geometrical symmetry of the FWT and only model one eighth of the transducer, the model's boundary conditions were defined in cylindrical coordinates:

1. The nodes on the cross section of the model were only constrained in the $T\theta$ plane, and
2. the nodes on the bottom contact area were constrained in the TZ plane.

After specifying a global element edge length of 0,7 mm the model was changed manually during design iterations. Changing the three dimensions in the model independently and systematically, and each time performing a re-run, eventually led to satisfactory results.

Some dimensions were fixed, but the transducer's thickness, outside radius and radii of rounds were design variables and these were changed during design iterations. Figure 3.4.2 and table 3.4.1 illustrate the five dimensions, $t1, t2, t3, r1$ and $d1$, that were changed, as well as the results of three iterations needed to achieve an optimal design.

The final iteration had a maximum Von Mises stress of 208 MPa. Figure 3.4.3 illustrates the stress and strain distribution of a 120 N load on one eighth of the FWT. This maximum stress was found to be in the corner of the slots separating the ribs. The maximum displacement for iteration three was 0,018 mm and was found to be in the middle of the rib at maximum diameter.

Strain gauges were modelled on the FWT FEM model. This was accomplished by creating two rod elements and locating them radially and tangentially at the location of strain gauge application. The area and material properties for the rod elements, both needed for the input variables to PARTAN's CROD element, was arbitrarily chosen. Their minute size meant that they had no effect on the FWT model.

The strain calculated with these two rod elements were $-2{,}529 \times 10^{-04}$ radial strain and $-5{,}871 \times 10^{-05}$ tangential strain. General strain gauges measure a maximum strain

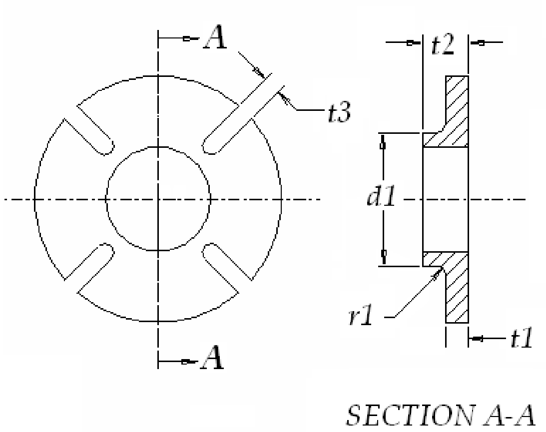

Figure 3.4.2: Force washer transducer.

Table 3.4.1: Force washer dimension iterations.

Iter	r1 $[mm]$	t1 $[mm]$	t2 $[mm]$	t3 $[mm]$	d1 $[mm]$	σ_{max} $[MPa]$	$\delta_{max,tip}$ $[mm]$
1	1	3	5	3	14	219	0.014
2	2	2	5	3	15	136	0.012
3	2	2	5	3	14	208	0.018

of 1μm per 1 mm, resulting in a strain of $1 \times 10^{-3} \cdot$ Thus, the maximum strain calculated for the FWT is a quarter of general strain gauge range and thus an acceptable resolution was expected.

The natural mode shapes of the FWT were investigated. This was done to ensure that none of the significant spring surge modes would excite the FWT into its resonance frequencies. If this materialised, the FWT would cause inaccurate strain gauge measurements. A normal mode analysis was performed with NASTRAN. As expected, the normal modes of the FWT were much higher than those of the spring. The first two normal modes of the spring were found at 445,56 Hz and 520,16 Hz respectively (figure 6.4.11(a) and (b)), whereas the first two normal modes of the FWT was calculated to be 23,05 kHz and 61,33 kHz (figures 3.4.4 and 3.4.5).

Thus the spring's fundamental natural frequency is roughly 50 times lower than the FWT's fundamental natural frequencies. From this investigation it was clear that the spring's harmonics would not drive the FWT into its resonance frequencies.

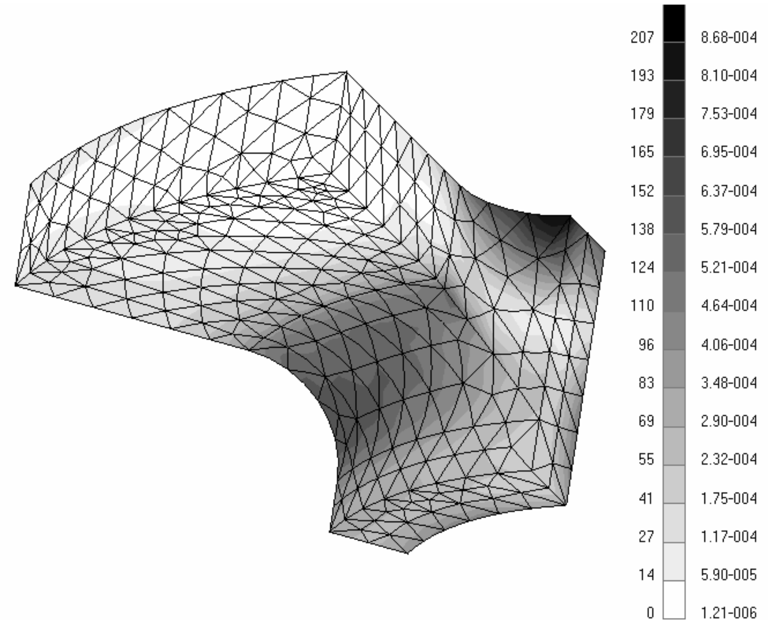

Figure 3.4.3: FWT von Mises stress and strain distribution for 120 N per one eighth rib.

3.4.2 FWT calibration

The FWT was instrumented as a full bridge strain gauge arrangement, known as the *Wheatstone bridge*. Appendix C contains a short review of the Wheatstone bridge. As figure 3.4.6 illustrates, two of the strain gauges would measure radial strain, and two would measure tangential strain. Tangential strain was calculated to have a insignificant value, but these gauges were still necessary to take advantage of the full strain gauge bridge arrangement and compensate for the temperature effects.

Although the FWT was designed for a specific load and safety factor (section 3.4.1), calibration was still necessary. Before calibration was commenced, the FWT was completely instrumented and installed into the cylinder head. Sensor damage and calibration discrepancies were minimised through this action. The sensor was installed into the cylinder head at intake valve number four. The dynamic models used the inlet cam profiles as input (it was also cooler than the exhaust side) and cylinder four allowed easy exit for the sensor wiring. Four core, shielded wire was used for the sensor wiring and was routed out of the cylinder head via a small hole drilled for this purpose. The shielded wire formed a *Farraday's* cage that minimised electromagnetic interference from the engine's high voltage ignition system, and minimised signal noise.

To compensate for the combined thickness of the FWT and the force spreading washer,

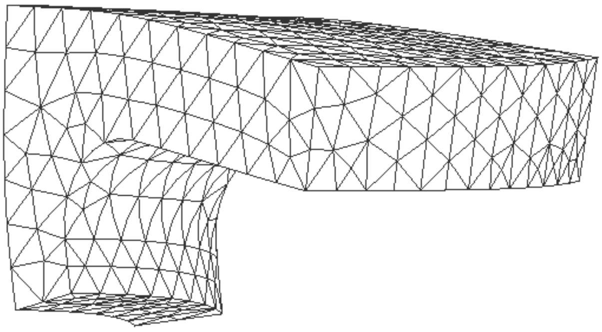

Figure 3.4.4: First vibration mode of FWT rib vibration at 23,05 kHz.

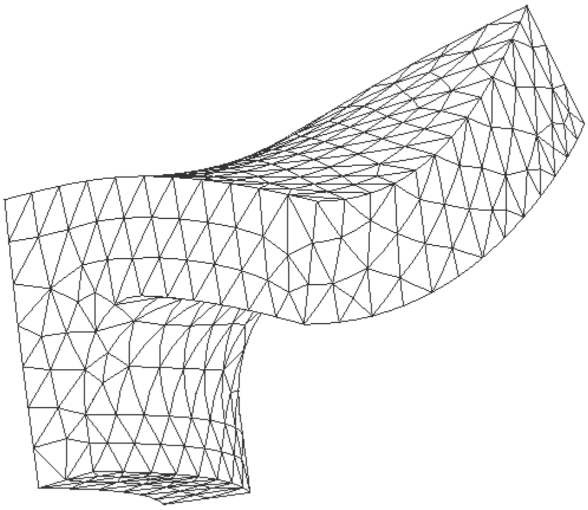

Figure 3.4.5: Second vibration mode of FWT rib vibration at 61,33 kHz.

the valve seat was machined deeper into the cylinder head to ensure correct spring installation length. To prevent the FWT from rotating under engine operating conditions and possibly damaging the extremely thin strain gauge wiring, a small pin was inserted at a position on the machined valve seat that fitted through one of the slots of the FWT. Figure 3.4.7 illustrates the cylinder head prior to sensor installation.

The signal from the FWT would be a voltage signal, passing through a HBM bridge

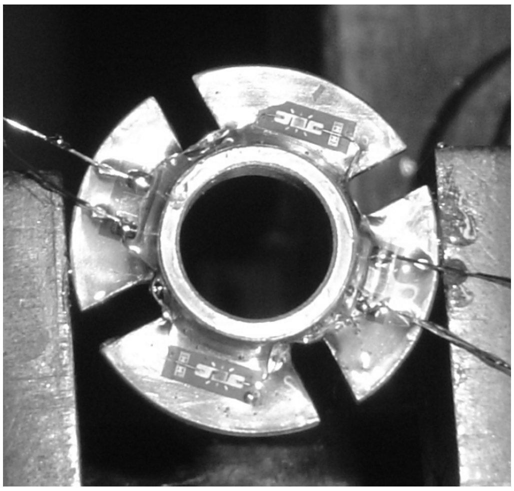

Figure 3.4.6: FWT underside before being installed into cylinder head.

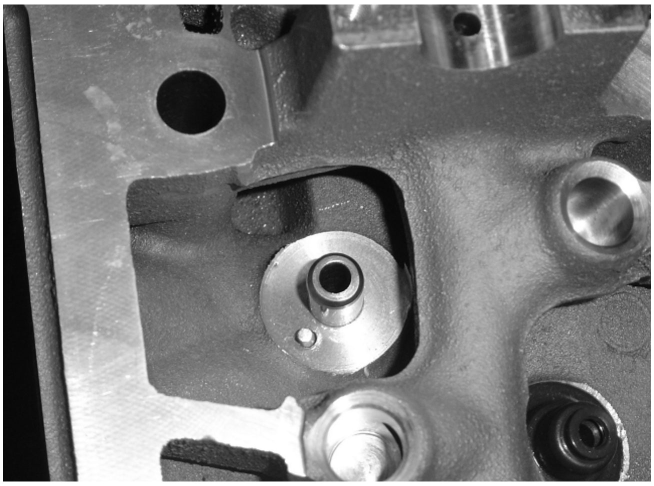

Figure 3.4.7: FWT positioning location in cylinder head.

amplifier. The final voltage signal had to be characterised into a force value. A small load cell (100 kg range) was first calibrated for use in the FWT calibration.

The load cell was calibrated by systematically loading it with carefully measured weights. The precise gravitational constant, g, at the location of calibration is 9,876 01 m/s^2 and this was used to calculate the exact force applied on the load cell. With a maximum sensor range of 12 mV/V an ideal linear load-voltage relationship was measured, illustrated in figure 3.4.8.

A linear curve was fitted through these points and the load cell was linearised with the following equation,

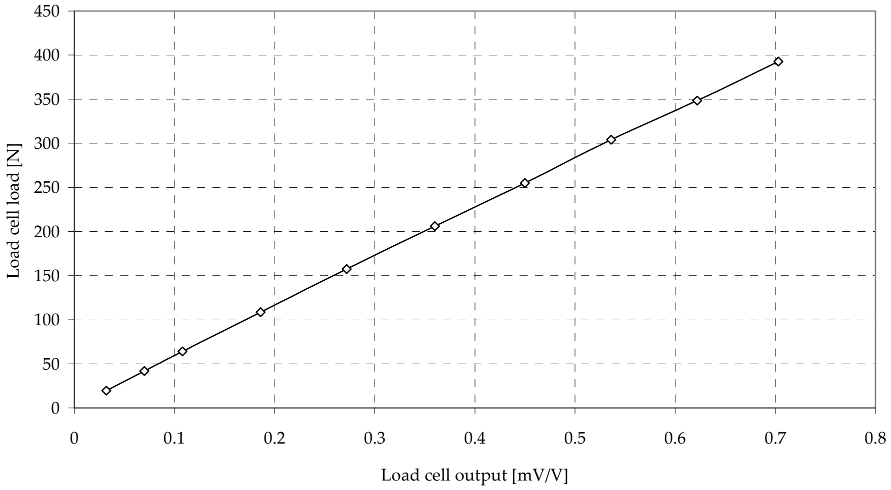

Figure 3.4.8: Load cell calibration result.

$$y = 556.16x + 4.0902 \tag{3.4.1}$$

The next step was to use the load cell to calibrate the FWT. Similar to the first static compression experiment of section 3.1, the FWT was loaded by assembling the valve spring, force spread washer and load cell into the cylinder head. A normal clamp was used to compress the spring until block length. Figure 3.4.9 illustrates the calibration setup.

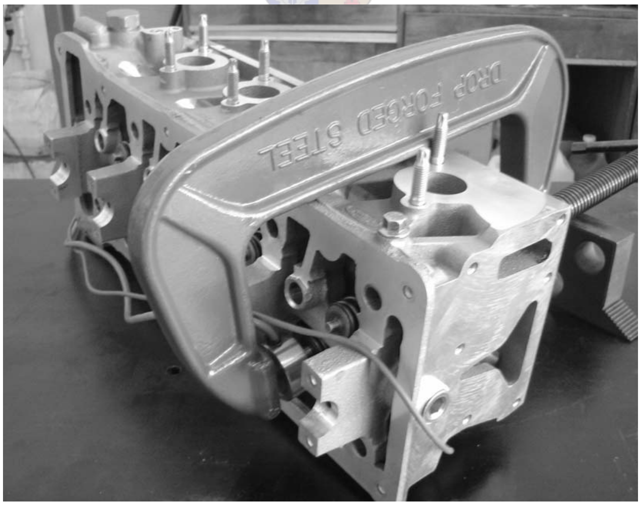

Figure 3.4.9: FWT calibration setup.

As was expected from the calculations, the FWT produced small strains. The bridge amplifier was set to maximum amplification, but the loaded FWT still produced a small voltage range. In future, a sensor could be designed with a smaller safety factor that would result in larger displacements and strains. Nonetheless, the measured voltage range was sufficient and produced a voltage range of approximately 500 mV from a load of 100 N to 900 N. Figure 3.4.10 illustrates two calibration measurements.

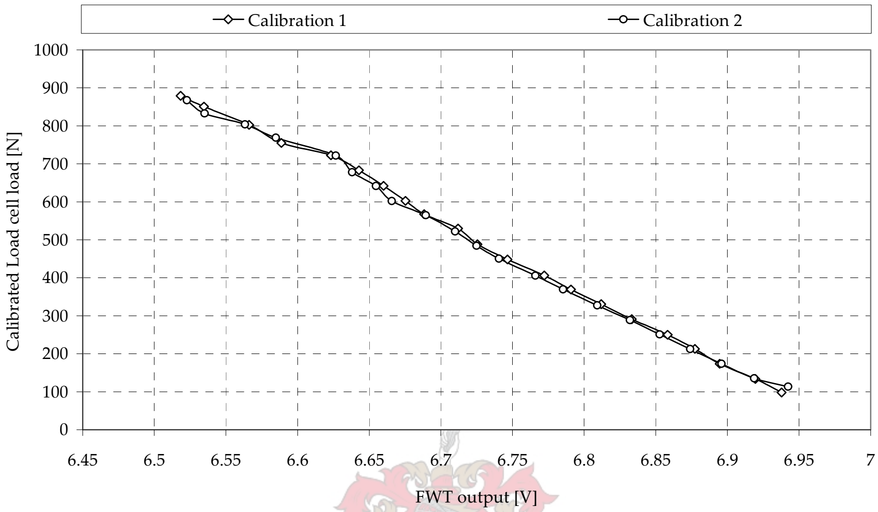

Figure 3.4.10: FWT calibration result.

Unfortunately, the load-voltage relation of the FWT was not as linear as that of the load cell. This was mainly due to a "hump" at approximately 700 N. This "hump" remained present at every other calibration measurement taken and was therefore repeatable and accepted as inherent to the FWT. If a linear curve was fitted through these deviation points, an approximate maximum error of 20 N could result.

Some alternative curve fitting methods were incorporated, some of which included the cubic spline and polynomial curve fitting methods. All gave undesirable results. It was thus decided to use linear interpolation to find values between calibrated values. The final break points (points used for the interpolation) were found by averaging four different calibration measurements. MATLAB was used to calculate these averages and find the break points. MATLAB was also used to interpolate (*inter*1 function) all the measured values quickly and efficiently.

By calculating average breakpoints and interpolating all measured voltage values from the FWT with MATLAB, spring force values could be calculated. This concluded the FWT calibration, which led to the actual valve spring force measurement, discussed in the following section.

3.4.3 Valve spring force measurement.

The Siglab spectrum analyser had a maximum sampling rate of 51,2 kHz. This was deemed insufficient for the spring force measurements at maximum engine speed. A MicroDaq was available which could sample analogue data up to 96 kHz. Two channels of information were measured for the valve spring force measurements, or spring seat force measurements. The FWT voltage, as well as the voltage from the standard Ford cam phasing sensor, were measured.

In total six measurements were made at engine crankshaft speeds ranging from 1000 rpm to 6000 rpm, every 1000 rpm. Each engine speed measurement was recorded at a different frequency in order to sample five cam events per recording, as illustrated in figure 3.4.11. Maximum hardware capability was used at maximum engine speed however, thus sampling at 96 kHz at 6000 rpm engine speed.

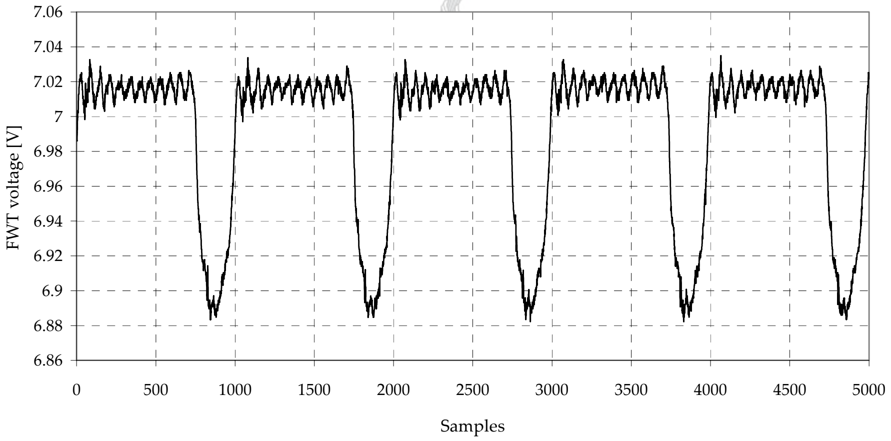

Figure 3.4.11: Complete FWT voltage recording at 4000 rpm engine speed containing five cam events.

Every recording was imported into a MATLAB programme written specifically to perform some basic data processing. Compared to acceleration measurements, all force measurements were relatively free from noise. The MATLAB programme split each recording into five separate cam events, calculated the average of the five cam events and finally filtered this averaged data to 3.5% of the sampling frequency, again using a Windowed-Sinc low pass digital filter (refer to figure 3.4.12). Filtering the 6000 rpm engine speed recorded data at 0.5% of the sampling frequency improved filter performance. This averaged and filtered data was used to modify and verify the dynamic model.

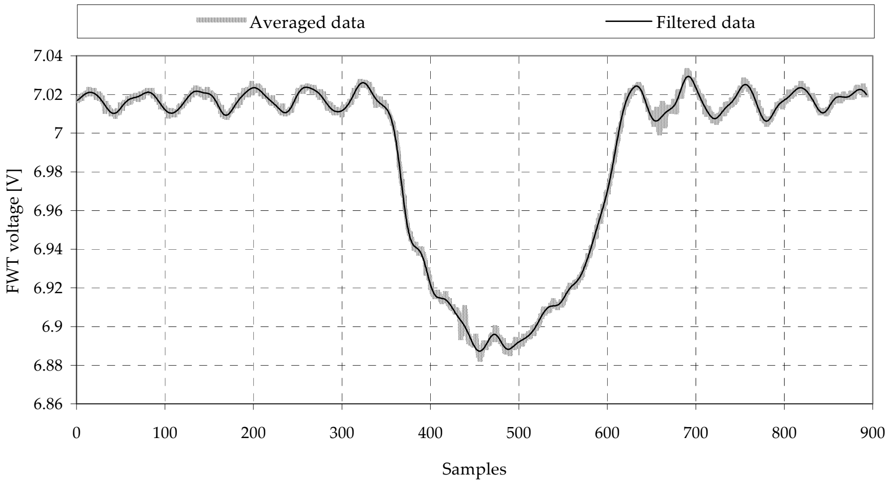

Figure 3.4.12: Averaged and filtered FWT voltage recording at 4000 rpm.

The successful completion of the valve spring seat force measurements concluded the experimental phase of this project. With the aid of the valve acceleration and spring force measurements the dynamic models could be verified and therefore achieve one of the primary objectives of the project. This is discussed in chapter 7.

Chapter 4

Mathematical Spring Models

The use of mathematical models was not the objective of this project. Commercial packages available for use in this project were far more advanced than any mathematical model that could be developed with this project's resources. By using these software packages an advanced and accurate model could be developed in a relatively short space of time. However, mathematical models were still investigated for background knowledge and it provided valuable insight into the mechanism of spring dynamics. Three models are discussed in this chapter, namely the dual-mass model, the surge-mode spring model and the multi-mass discrete model.

4.1 The dual-mass spring model

The dual-mass spring model is the simplest model for valve springs. It consists of one linear spring and it's mass is distributed into two masses located at the ends of the spring. One of these masses are usually fixed. This model is used when the cam mechanism only serves as a excitation mechanism. This was the first model used in valve train dynamic models and can be described by the basic, undamped, one degree of freedom spring-mass system.

$$m\ddot{y} + ky = 0 \tag{4.1.1}$$

where k is the spring stiffness, m is the active spring mass and y is the displacement coordinate along the length of the spring.

The model does not take into account any internal dynamics of the spring and is therefore not suited for the dynamic investigation of valve trains and will therefore not be discussed further.

4.2 Surge-mode approach model

The surge-mode model is an efficient and accurate model for linear valve springs and is used extensively in valve train models. Theory used in most software packages are based on normal mode analysis techniques and therefore this model is relevant to this project.

The model takes advantage of the fact that an elastic medium fastened at both ends can be described in terms of normal modes. To a good approximation one can say that the spring shows wave propagation and disturbances.

The first mode of motion with the lowest frequency is an in phase motion of all the spring particles with the maximum amplitude in the middle of the spring. Amplitudes at the end of the spring remain zero due to the fixed ends. In the second mode the two halves of the spring move in anti-phase with roughly twice the frequency. Figure 4.2.1 illustrates the first two modes of this motion.

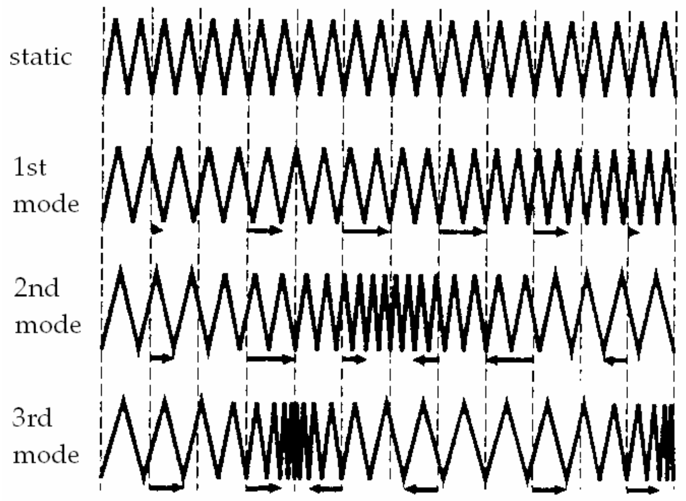

Figure 4.2.1: First three mode shapes of a linear, one dimensional spring.

The above approximation could be extended to assume that each individual infinitely small spring element is governed by the wave equation (Schamel (1989)), a second order partial differential equation.

$$\frac{\partial^2\psi(y,t)}{\partial t^2} = c^2\frac{\partial^2\psi(y,t)}{\partial y^2} \tag{4.2.1}$$

where ψ is the particle displacement and $c = \sqrt{L^2\,k/m}$ is the speed of wave propagation, in analogy to the speed of sound in air, and L is the spring length.

The two boundary conditions for this equation is spring displacement at the retainer side being equal to the valve displacement at the retainer, $h(t)$, and zero at the other end.

$$\psi(0,t) = h(t) \quad , \quad \psi(L,t) = 0 \tag{4.2.2}$$

The force exerted by the spring on the valve is proportional to the gradient of particle displacement, ψ. By adding the pre-load force component, exerted from the spring installation compression, $F_0 = kS$, where S is the pre-load displacement, the total force exerted by the spring on the valve is then given by

$$F = F_0 + Lk\frac{\partial \psi}{\partial y} \tag{4.2.3}$$

Statically, the force is uniform throughout the spring and by using equation 4.2.2 and equation 4.2.3 we find that the static displacement is

$$\psi(y) = \frac{(L-y)}{L}h(t) \tag{4.2.4}$$

For the time dependent solution the displacement consists of the static displacement, $s(t)$, plus the dynamic deviation, $\mu(y,t)$

$$\psi(y,t) = \frac{(L-y)}{L}h(t) - \mu(y,t) \tag{4.2.5}$$

From equation 4.2.5 differentiating partially we find

$$\frac{\partial \psi(y,t)}{\partial y} = -\frac{h(t)}{L} + \frac{\partial \mu(y,t)}{\partial y} \tag{4.2.6}$$

$$\frac{\partial^2 \psi(y,t)}{\partial y^2} = \frac{\partial^2 \mu(y,t)}{\partial y^2} \tag{4.2.7}$$

$$\frac{\partial \psi(y,t)}{\partial t} = \frac{(L-y)}{L}\frac{dh(t)}{dt} + \frac{\partial \mu(y,t)}{\partial t} \tag{4.2.8}$$

$$\frac{\partial^2 \psi(y,t)}{\partial t^2} = \frac{(L-y)}{L}\frac{d^2h(t)}{dt^2} + \frac{\partial^2 \mu(y,t)}{\partial t^2} \tag{4.2.9}$$

By substituting equations 4.2.7 and 4.2.9 into equation 4.2.1 the governing equation for the dynamic deviation from the static solution is found as

$$\frac{\partial^2 \mu(y,t)}{\partial t^2} = c^2 \frac{\partial^2 \mu^2(y,t)}{\partial y^2} - \frac{(L-y)}{L}\frac{d^2 h(t)}{dt^2} \tag{4.2.10}$$

with boundary conditions $\mu(0,t) = \mu(L,t) = 0$. If we now examine the free solution of the dynamic component of the spring motion, we are looking for oscillatory solutions of the separable form

$$\mu(y,t) = M(y)e^{j\omega y} \tag{4.2.11}$$

If we substitute equation 4.2.11 in 4.2.10 and neglect the forcing to get the free solution, we get

$$\frac{d^2 M(y)}{dy^2} + \frac{\omega^2}{c^2}M = 0 \qquad M(0) = M(L) = 0 \tag{4.2.12}$$

Using $\omega/c = n\pi/L$ this ordinary differential equation has the solution

$$M(y) = \sin\left(\frac{n\pi y}{L}\right) \qquad n = 1,\, 2,\, 3, \ldots \tag{4.2.13}$$

again with $c^2 = L^2 k/m$ we get the n'th mode frequency

$$\omega_n = n\pi\sqrt{\frac{k}{m}} \qquad n = 1,\, 2,\, 3, \ldots \tag{4.2.14}$$

With the above derivation the spring dynamic response problem has been reduced to a linear partial differential equation and the solution can be expressed as the superposition of modes. In order to solve for the normal modes, solutions of equation 4.2.10 are needed of the form

$$\mu(y,t) = \sum_n G_n(t)\sin\left(\frac{n\pi y}{L}\right) \tag{4.2.15}$$

In order to find this solution we must be able to project the spatial component of the excitation onto the mode shapes leading to

$$\frac{(L-x)}{L} = \sum_n a_n \sin\left(\frac{n\pi y}{L}\right) \qquad 0 < x < L \tag{4.2.16}$$

Since the spatial component of the excitation is a segment out of a saw-tooth characteristic (cam events produced by the rotating camshaft) and the mode shapes form a sine series, the solution is simply the Fourier coefficients for a falling saw-tooth characteristic, namely

$$a_n = 2/n\pi \tag{4.2.17}$$

Substituting equation 4.2.16 and 4.2.17 into 4.2.10

$$\frac{\partial^2 \mu(y,t)}{\partial t^2} = c^2 \frac{\partial^2 \mu^2(y,t)}{\partial y^2} - \frac{2}{n\pi} \sin\left(\frac{n\pi y}{L}\right) \frac{d^2 h(t)}{dt^2} \tag{4.2.18}$$

Further substituting equation 4.2.15 into equation 4.2.18 transforms the partial differential equation from equation 4.2.10 into a series of ordinary differential equations

$$\frac{d^2 G_n(t)}{dt^2} + \frac{kn^2\pi^2}{m} G_n(t) = -\frac{2}{n\pi} \frac{d^2 h(t)}{dt^2} \tag{4.2.19}$$

Using equation 4.2.14, equation 4.2.19 becomes the standard form for a simple undamped harmonic oscillator with explicit time dependant forcing,

$$\frac{d^2 G_n(t)}{dt^2} + \omega_n^2 G_n(t) = -\frac{2}{n\pi} \frac{d^2 h(t)}{dt^2} \tag{4.2.20}$$

In the practical application of the valve spring, internal spring damping should be accounted for. Fortunately the damping levels are low and a simple viscous damping model serves most purposes. The following term should simply be added to equation 4.2.20

$$2\zeta\omega_n \frac{dG_n(t)}{dt} \tag{4.2.21}$$

However, to keep this mathematical model review simple, the damping is omitted in this discussion. For further simplicity the solution is scaled in cam angle rather than time by substituting $dt = d\phi/\omega_{cs}$ into equation 4.2.21 and simplifying,

$$\frac{d^2 G_n(\phi)}{d\phi^2} + \frac{\omega_n^2}{\omega_{cs}^2} G_n(\phi) = -\frac{2}{n\pi} \frac{d^2 h}{d\phi^2} \tag{4.2.22}$$

where ω_{cs} is the cam rotation speed.

By combining equation 4.2.3, 4.2.4 and 4.2.15 the total force at any position y in the spring is given by

$$F(y,\phi) = -k\left(S + h(\phi) - \pi \sum_n n G_n(\phi) \cos\left(\frac{n\pi y}{L}\right)\right) \tag{4.2.23}$$

Equation 4.2.23 can now be solved easily by expressing the known excitation, $h(\phi)$, as a Fourier series as well (refer to appendix A for a review on Fourier series theory).

$$\frac{d^2 h(\phi)}{d\phi^2} = -n^2 \sum_{n=1}^{\infty} (a_n \cos\phi n + b_n \sin\phi n) \tag{4.2.24}$$

The solution of the simple undamped harmonic oscillator equation will also be a Fourier series for each spring mode and given by

$$G_n(\phi) = \sum_{n=1}^{\infty} (p_n \cos \phi n + q_n \sin \phi n) \tag{4.2.25}$$

By substituting equation 4.2.24 and 4.2.25 into equation 4.2.22 the complete numerical solution is found

$$\sum_{n=1}^{\infty} \left[-n^2 (p_n \cos \phi n + q_n \sin \phi n) + \frac{\omega_n^2}{\omega_{cs}^2} (p_n \cos \phi n - q_n \sin \phi n) \right] = \frac{2n}{\pi} \sum_{n=1}^{\infty} (a_n \cos \phi n + b_n \sin \phi n) \tag{4.2.26}$$

By comparison of the coefficients a set of algebraic equations are found to solve the coefficients p and q with.

$$p_n = a_n \left(\frac{2n\omega_{cs}^2}{\pi(\omega_n^2 - n^2\omega_{cs}^2)} \right) \tag{4.2.27}$$

$$q_n = b_n \left(\frac{2n\omega_{cs}^2}{\pi(\omega_n^2 - n^2\omega_{cs}^2)} \right) \tag{4.2.28}$$

With the above derived method it is possible to calculate the spring dynamics, $\psi(y, \phi)$, by knowing the excitation, $h(t)$ or $h(\phi)$, and the spring's natural frequency, ω_n. The spring's excitation is defined by the cam lobe's shape and the natural frequency is calculated from spring geometry and material properties (discussed in section 6.2).

As an illustration of this model the spring force at the bottom of the spring, $y = L$, was calculated by writing a MATLAB program. The measurement of the forces at this location in the valve train system was one of this project's objectives and performing this calculation could lend some insight into what to expect.

Figure 4.2.2 shows the spring force calculated with the MATLAB program at 3000 rpm. The figure clearly illustrates the contribution to the total force from the static and the dynamic component respectively. Note that this solution was found with zero initial conditions, i.e. $F(y, 0) = F(y, 2\pi) = 0$. In reality this is not the case.

There is a difference in oscillations between the valve spring and the rest of the valve train. The rest of the valve train is a dynamic system which changes dramatically when the valve opens and closes. In the closed position, the valve is always supported by the valve seat and all the components are essentially decoupled. Under the decoupled conditions all oscillations die out rapidly.

The valve spring is completely different. The excitations only takes place during the cam event, but the spring is always connected between the spring seat and the retainer

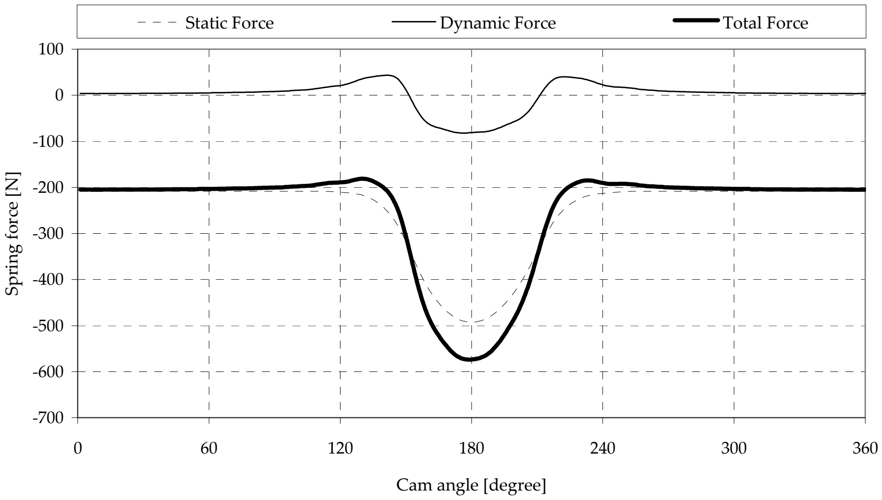

Figure 4.2.2: Static and dynamic force components of the total spring force.

and never decoupled. Damping in the spring is also very small and the oscillations excited during the cam event do not die out before the next cam event starts. The result is non-zero initial conditions. To reach steady state response for the valve spring the integration time needs to be spread over multiple camshaft revolutions. This sort of model sophistication goes beyond the scope of this discussion and will not be included in the above solution.

Surge-mode models are effective and accurate as long as the spring is operating in its linear ranges. The model does not consider any non-linearity caused by the interaction between spring windings. Unlimited mode amplitude is possible, thus no coil clash is included. This limits the model when the valve train needs to be evaluated or optimised to its dynamic limits. The multi-mass discrete model is a mathematical approach to solve this limitation and is briefly discussed in the following section.

4.3 Multi-mass discrete model

The multi-mass discrete model formed the basic concept for the dynamic model used in this project and will be discussed in detail throughout this document. Therefore the mathematical model will only be discussed in brief concepts and not in as much detail as the surge-mode mathematical model.

Valve spring geometries have become very complicated and in explaining this Schamel (1993) states that the increased speed requirements of modern engines forces spring manufactures to manufacture complicated spring geometries:

Since the basic spring frequency cannot be increased significantly, increased engine speeds have caused the lower cam harmonics to become critical and cause spring oscillations. To avoid excessive resonance, non-linear springs which change their natural frequency with lift are being used. In a strict sense the term natural frequency is no-longer correct for a non-linear spring, since the number of active coils of the spring, N_a, and therefore natural frequency, changes with deformation and spring surge amplitude of the spring. It is still convenient to use the term since it describes the frequency of the low amplitude free vibration at any given length of the spring.

The change in natural frequency with lift is therefore caused by coils becoming inactive as they come in contact with adjacent coils. The non-linearity of the spring is thus caused by geometry arrangements and not by an actual non-linearity of the spring's wire stiffness. Oscillations are further limited in some designs by deliberately driving the valve spring near its solid length during the valve lift, causing additional damping by coil clashing effects.

Again, by ignoring the damping terms for the purpose of simplicity, the simple discrete model in figure 4.3.1 (a) is governed by the following equation.

$$m_i\ddot{h}_i = k_i(h_{i-1} - h_i) + k_{i+1}(h_{i+1} - h_i) \tag{4.3.1}$$

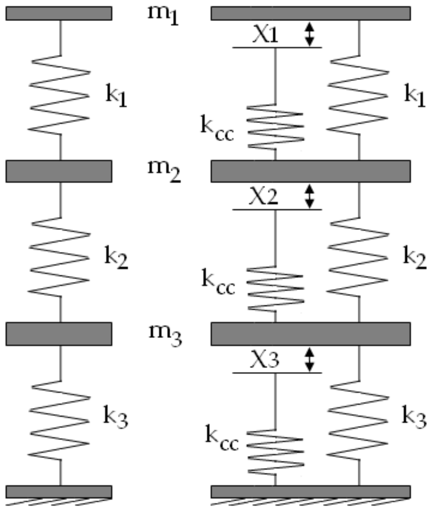

(a) (b)

Figure 4.3.1: Simple discrete valve spring model (a) without, and (b) with coil clash.

Again, as in the case of the surge mode model, we separate the static displacement, $s(t)$, from the dynamic deviation, $\mu(t)$, using the difference formulation $h(t) = s(t) + \mu(t)$.

$$m_i \ddot{\mu}_i - k_i(\mu_{i-1} - \mu_i) - k_{i+1}(\mu_{i+1} - \mu_i) = -m_i \ddot{s}_i + k_i(s_{i-1} - s_i) + k_{i+1}(s_{i+1} - s_i) \quad (4.3.2)$$

This is the resulting set of differential equations for figure 4.3.1 (a). This model also allows unlimited amplitude and the surge-mode model is equivalent to the discrete model with the number of masses approaching infinity. The multi-mass discrete model however, lends the opportunity to define a force between two elements which only acts if the two elements get too close.

By introducing these additional force laws, this limitation is overcome. The force laws will act if two neighbouring elements exceeds the available free space, X_i, between them. This force is refer to as the coil clash force, F_{cc}.

$$F_{cc_i} = \begin{cases} f(s_i, s_{i+1}, \mu_i, \mu_{i+1}, k_{cl}) & \text{if } s_i - s_{i+1} + \mu_i - \mu_{i+1} \geq X_i \\ 0 & \text{if } s_i - s_{i+1} + \mu_i - \mu_{i+1} < X_i \end{cases} \quad (4.3.3)$$

Continuing with this model by defining the law for this class force is unnecessary, because the concept behind the multi-mass discrete model illustrated satisfactorily. The remaining modeling in this project is ultimately based on this model.

Chapter 5

Hydraulic Lash Adjuster Model

The *Hydraulic lash adjuster* (HLA) is a standard construction unit used in modern valve trains. The functioning of the lifter and a detailed hydraulic model is presented in this chapter. A simplified version of this complete model was planned to be implemented in the dynamic model and the simplifications are discussed. In order to judge the shortcomings of the simplified model, the influence of the HLA on the valve train system is studied and discussed over different engine operating ranges. This gave insight into the accuracy of the simplified model. By comparing the measured valve spring forces, described in section 3.4.3, against the spring forces calculated in the dynamic model, validation of this simplified HLA model is achieved.

5.1 The functioning of the hydraulic lash adjuster

As shown in figure 5.1.1, the HLA consists of an housing, a plunger, a plunger return spring, a check valve, check valve spring and a cage. The high pressure chamber is the volume between the plunger and housing and is connected to the oil reservoir via the check valve mechanism. The oil reservoir remains connected to the cylinder head's oil rail at all times.

During the cam dwell period (base circle), and under normal operating conditions, the check valve is closed. The plunger return spring forces the plunger and oil reservoir against the finger follower and removes any gaps or lash that might exists between the valve train components. When compressive forces are applied to the HLA, such as in the event of cam lift, the plunger is forced into the housing, the plunger return spring compresses and the oil pressure inside the high pressure chamber increases due to the compression. The pressure increase creates a pressure difference and subsequent leak-

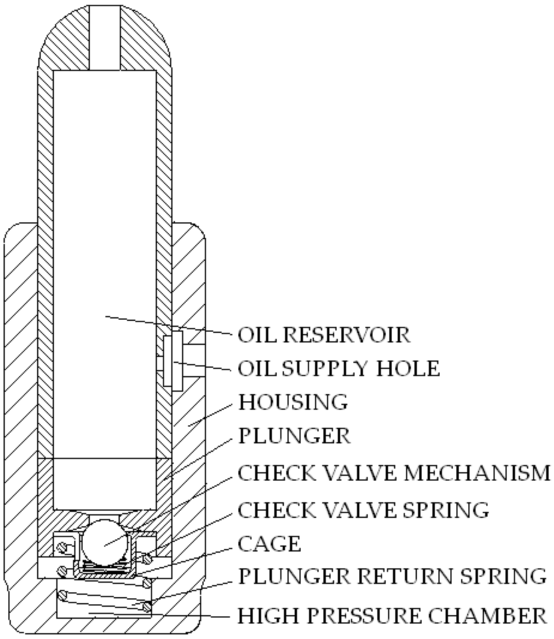

Figure 5.1.1: Hydraulic lash adjuster configuration.

age through the annular slot between the housing and plunger. (The leakage through the annular slot is the only form of damping the HLA offers.) In the compression process, the check valve remains closed by the high pressure inside the high pressure chamber.

When lift ends and the cam runs on its base circle again, the forces on the HLA become smaller than the elastic forces of the plunger return spring and thus the high pressure chamber expands to occupy any valve clearance. As oil has leaked, a pressure drop inside the high pressure chamber occurs. The higher pressure in the oil reservoir forces the check valve to open and allows oil to flow from the oil reservoir and re-fill the high pressure chamber. The check valve is closed by the check valve spring when the high pressure chamber pressure equalises with the oil reservoir pressure.

5.2 The HLA as an important valve train component

The HLA has well known advantages and they are being used more and more in modern valve trains. The operating surfaces of the HLA do not wear and this results in a constant load exchange during engine life, i.e. no gaps appear between moving parts. Engines fitted with HLA have less maintenance costs compared to engines fitted with tappets or shims which need complicated adjustments over time. Due to a decrease in vibration from collision excitation, an acoustic improvement results from using an HLA as well.

With these advantages some disadvantages need to be considered as well. Replacing a solid lifter with a hydraulic one means installing a valve train component with much lower stiffness. This difference increases the lifter's influence on the valve train dynamics.

Using the engine oil, which is often mixed with air, as the hydraulic fluid results in non-negligible compressibility. Being connected to the engine oil supply system can also cause malfunction of the HLA due to critical conditions in the oil circuit, such as a malfunctioning or worn oil pump.

The operation of the check valve, that could be described as an additional vibration system and important for the refill function of the high pressure chamber, is highly sensitive to the valve train dynamics.

Finally, after engine shut-off, open valves can shorten the hydraulic elements due to leakage. This causes slack in the valve train and contact loss between valve train components that causes severe noise and possible component damage for a limited period after engine start.

From the above it is clear that the HLA is highly complex and sensitive to various engine operating conditions. A deep insight into HLA dynamics is thus required. By studying an effective mathematical model of the HLA, such knowledge and insight is attained. The following section discusses such a mathematical model in detail.

5.3 Hydraulic lash adjuster model

In overview of the following section, the reaction force, reacting against the compressive force applied on the HLA by the valve train, needs to be calculated from a model of the HLA. This section describes this calculation in detail.

Schamel (1989) included a relatively simple HLA model in their valve train model modelled in ADAMS. It was a damper-spring model characterised from extensive experiments. The model included oil aeration and oil leakage, but did not include check valve operation. The model was used successfully with good results. Zou & McCormick (1996) developed a hydraulic model of the HLA and included check valve operation. They used a step-by-step calculation method to solve a numerical model of the valve train system. The HLA model used in this project was adopted from the theory developed by them and their model will be discussed in detail in this chapter. Porot & Trapy (1993) developed a similar model and applied it onto a direct acting cam valve train arrangement.

Oil pressure in the high pressure chamber is determined by its volume and the quantity of oil contained in it. The bulk modulus of elasticity of fluids is defined as

$$E = -\frac{dp}{dV/V} \tag{5.3.1}$$

where p is the pressure of the fluid and V is the volume of fluid mass. The bulk modulus of elasticity E depends upon the thermodynamic process causing a change of state. The bulk modulus of oil, E_{oil}, varies slightly with pressure

$$E_{oil} = E_0 + \beta p \tag{5.3.2}$$

where E_0 and β are constants specific to the oil being used.

As mention previously, air entrainment into the oil is common and constitutes a two phase system which has different properties from either of its components. The mixture bulk modulus, E, at a reference state is written as

$$E = \frac{E_{oil}E_{air}}{\phi_{oil}E_{air} + \phi_{air}E_{oil}} \tag{5.3.3}$$

where E_{air} = bulk modulus of air;
ϕ_{air} = volume fraction of air;
ϕ_{oil} = volume fraction of oil.

Zou & McCormick (1996) assumed that the process of homogenisation for the components is isothermal and the bulk modulus of air is

$$E_{air} = p \tag{5.3.4}$$

The mass density of the mixture is given by

$$\rho = \phi_{air}\rho_{air} + \phi_{oil}\rho_{oil} \tag{5.3.5}$$

where ρ_{air} and ρ_{oil} is the density of air and oil in pure state respectively. Zou & McCormick (1996) used an experimentally determined viscosity relationship of air-oil mixtures found to be

$$\mu_{mix} = \mu_{oil}(1 + 1.0\phi_{air}) \tag{5.3.6}$$

where μ_{mix} is the viscosity of the mixture and μ_{oil} is the viscosity of the oil.

By the definition of bulk modulus (refer to equation 5.3.1) the pressure variation is expressed as

$$dp = -E\frac{dV}{V} \tag{5.3.7}$$

This pressure variation is what Zou & McCormick (1996) used in their step-by-step calculation of high pressure chamber pressure. The numerical iteration could be expressed as

$$p_{n+1} = p_n - E\frac{\triangle V}{V_n} \tag{5.3.8}$$

where the subscripts n and $n+1$ represents the time steps n and $n+1$. Therefore, the volume variation, $\triangle V$, was calculated for each calculation step. Returning to the format used in equation 5.3.7, the volume variation of the fluid mass is calculated as

$$dV = dV_{vol} + dV_{pas} + dV_{cv} \tag{5.3.9}$$

where dV_{vol} = volume variation of the high pressure chamber which depends only on the change in the distance between the housing and plunger;

dV_{pas} = volume variation of oil passing through the annular slot caused by the gap between the plunger and housing;

dV_{cv} = volume variation of oil passing through the check valve.

The volume of oil passing through the annular slot from the gap between the plunger and housing is calculated by (refer to appendix D for the derivation of this equation)

$$\begin{aligned} dV_{pas} = \dot{Q}_{pas}\,dt =& \pi U_p h_g \left(r_p + \frac{2}{3}h_g\right)dt \\ & - \frac{\pi}{6\mu_{mix}}{h_g}^3\left(\frac{dp}{dx}\right)\left(r_p + \frac{h_g}{2}\right)dt \end{aligned} \tag{5.3.10}$$

where $\dot{Q}_{pas}$ = volume flow rate through the annular slot caused by the gap between the plunger and housing;

U_p = velocity of the plunger;

h_g = passage height of the gap;

r_p = outside radius of plunger;

$\frac{dp}{dx}$ = pressure gradient over length of gap.

The volume of oil passing through the check valve is calculated by

$$dV_{cv} = \dot{Q}_{cv}\,dt = \left[f_e\,S_e\left(\frac{2}{\rho}(p_{hps} - p_{oilres})\right)^{\frac{1}{2}}\right]dt \tag{5.3.11}$$

where $\dot{Q}_{cv}$ = volume flow rate through the check valve;
f_e = discharge coefficient of the check valve passage opening;
S_e = annular section opened by check valve displacement;
p_{hps} = high pressure chamber pressure;
p_{oilres} = oil reservoir pressure.

Calculating the discharge coefficient, f_e, becomes complicated and is one of the main parameters that determines the sophistication of any HLA model.

The reason for the complication is the fact that f_e is a function of the Reynolds number of the fluid flow through the check valve passage. The Reynolds number, in turn, is a function of the fluid speed through the passage, U_e, which is found by using *Bernoulli*'s equation. Using the *Bernoulli* equation for steady, frictionless, incompressible flow and the control volume shown in figure 5.3.1, the following expression is found

$$\frac{p_{hpc} - p_{oilres}}{\rho} + \frac{1}{2}(U_e - U_{oilres}) + g(h_e - h_{oilres}) = 0 \tag{5.3.12}$$

where U_e = fluid speed at annular section S_e;
U_{oilres} = fluid speed at entrance of annular section on the oil reservoir side;
g = gravitational constant;
h_e = boundary layer height at annular section S_e;
h_{oilres} = boundary layer height at entrance of annular section on the oil reservoir side.

Mass conservation is usually a vital part of the *Bernoulli* analysis. Thus, if S_{oilres} is the annular section on the oil reservoir side, the flow through the check valve passage is one-dimensional with constant density. The following relation

$$S_e U_e = S_{oilres} U_{oilres} \tag{5.3.13}$$

together with the assumption that the difference in heights, h_e and h_{oilres}, is negligible, compared to the difference in fluid velocities, U_e and U_{oilres}, the *Bernoulli* equation 5.3.12 simplifies to

$$U_e = \frac{2}{\rho}\left(\frac{p_{oilres} - p_{hpc}}{1 - S_e/S_{oilres}}\right) \tag{5.3.14}$$

From equation 5.3.14 it is shown that the fluid speed U_e is a function of the annular section, S_e. S_e is calculated using trigonometric calculations and is expressed as a function

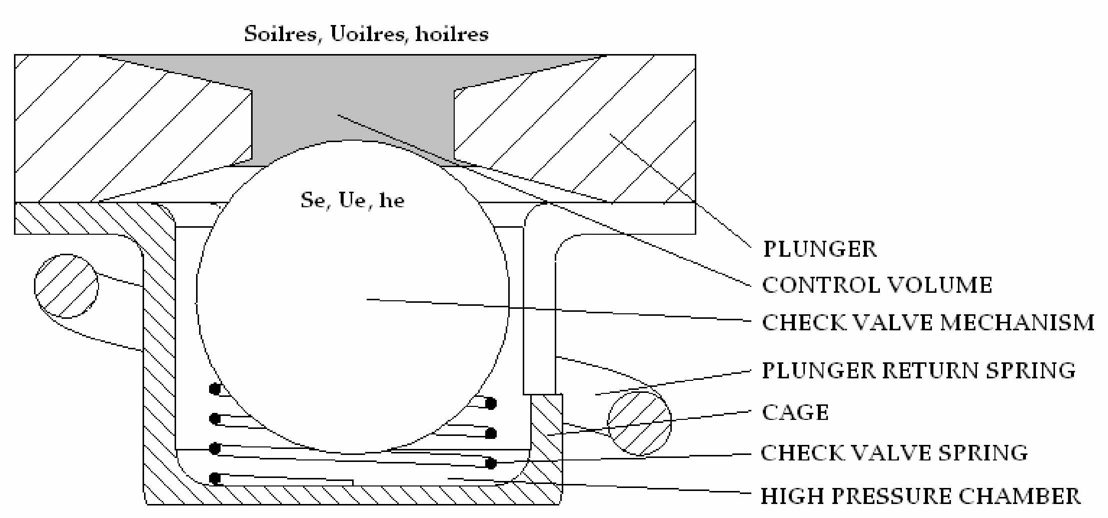

Figure 5.3.1: Check valve control volume.

of check valve displacement s_{cv}. Thus in summary of the above few paragraphs and equations, the discharge coefficient f_e is related to the check valve displacement s_{cv} by the following expression

$$f_e = f(Re = f(U_e = f(S_e = f(s_{cv})))) \tag{5.3.15}$$

The check valve mechanism is found to be a dynamic, independent, single degree of freedom, spring mass system.

$$\sum_i F_i = m_{cv}\ddot{s}_{cv} \tag{5.3.16}$$

where m_{cv} is the mass of the check valve and $\ddot{s}_{cv}$ the check valve acceleration. The applied forces on the check valve, F_i, are the oil pressure force, F_{cv}^{prs} and the viscous friction force, F_{cv}^{vis}. The pressure force acting on the check valve is calculated by

$$F_{cv}^{prs} = \pi r_h^2 (p_{hps} - p_{oilres}) \tag{5.3.17}$$

where r_h is the radius of the check valve passage. The viscous friction force acting on the check valve is calculated by

$$F_{cv}^{vis} = \frac{\pi}{2} f_d \, r_{cv}^2 \, \dot{s}_{cv} \rho \tag{5.3.18}$$

where r_{cv} is the radius of the check valve ball and $\dot{s}_{cv}$ is the velocity of the check valve relative to the housing. f_e is defined as

$$f_e = \begin{cases} 24/Re & \text{if } Re \leq 1 \\ 24(1 + 3Re/16)/Re & \text{if } Re > 1, \end{cases} \tag{5.3.19}$$

where Re is the Reynolds number which is defined as

$$Re = \frac{2r_{cv}\dot{s}_{cv}\rho}{\mu} \tag{5.3.20}$$

Thus, calculating the discharge coefficient, f_e, the dynamics of the check valve ball needs to be known in advance. To emphasise the complication and difficulty of calculating the dynamics of the check valve, the following facts need to be kept in consideration:

1. Due to the relatively small space the check valve operates in, contact with the plunger on the one side and with the spring in it's solid length conditions on the other side, adds a non-linear component to the dynamic equation in the form of impact and,
2. air bubbles flowing past the check valve ball adds uncertainty to the applied forces on the ball.

Essentially, the above two conditions are extremely complicated and have a relatively small influence on the valve train. However, the check valve spring-mass system has a free vibration mode shape and resonance frequency associated with it. If the applied forces excite the check valve into its natural frequency, "normal" check valve operation behaviour is deviated from and interesting valve train dynamics occur. Some of these are discussed in detail in section 5.5.

The latest ADAMS/Engine package is one software package that includes most check valve operating conditions. In the end, the desired accuracy of the valve train model needs to be established and this will determine the HLA model's level of sophistication for one.

Some simplifying assumptions regarding the check valve's operations were used successfully in this project and these will be discussed in section 5.4.

Concluding the discussion on the calculation of the discharge coefficient, f_e, with or without simplifications, it is thus possible to calculate the volume variation of the fluid mass in equation 5.3.9.

Once the volume variation is known, the pressure variation, dp, from equation 5.3.7 is known. Thus, the pressure inside the high pressure chamber is calculated after each time step. Finally with this, the reaction force on the plunger, reacting on the compressive forces that are applied to the HLA by the valve train, can be calculated. The reaction force consists of the viscous friction force on the side area of the plunger, F_p^{vis}, and the oil pressure force in the high pressure chamber, F_p^{prs}.

Oil flow thought the annular slot caused by the gap between the plunger and housing, causes the viscous force given by

$$F_p^{vis} = A_p^{side} \tau_p \tag{5.3.21}$$

where A_p^{vis} is the side area of the plunger and τ_p is the shear stress which is given by

$$\tau_p = \mu \frac{U_p}{h_g} - \frac{h_g}{2} \left(\frac{dp}{dx} \right) \tag{5.3.22}$$

The pressure force acting on the plunger is calculated from

$$F_p^{prs} = A_p^{base} p_{hpc} \tag{5.3.23}$$

where A_p^{base} is the area of the plunger base.

The discussion on the detailed model of the HLA is therefore concluded. In order to implement the HLA model into the dynamic model it needs to be simplified. The reasons for this will be discussed in the following section.

5.4 Implementation of a simplified HLA model

Implementing the HLA model discussed above, adopted from Zou & McCormick (1996), into the dynamic model of this project calls for simplification of the model. The main reason for this is that the equations of pressure variation are defined implicitly in the sense that the pressure is needed to calculate the pressure difference which in turn determines the pressure. Therefore a step-by-step iterative solution method is normally used.

The dynamic model of the valve train is modelled in ADAMS. ADAMS uses an iterative step-by-step solution method to solve the equations of motion for dynamic simulations. Unfortunately, this solution process or algorithm, was unaccessible for this project. ADAMS does however have a FORTRAN version of the ADAMS/Solver which could be used to build and model the HLA as discussed in section 5.3. By compiling a FORTRAN based computer program the step-by-step volume and pressure variations could be calculated. This process, however, goes beyond the scope of this project. By understanding the effects that simplifying the HLA will have on the valve train system, or lack of effect for that matter, a simplified model could be used based on the project objectives and the model accuracy required.

The model eventually used for the dynamic model in this project was relatively simple. Due to the difficulty of using a step-by-step numerical solution method, both the time [step] dependant calculation of dV_{pas} and dV_{cv} (equation 5.3.9) could not be calculated in ADAMS.

The result was that the pressure variation of the high pressure chamber depended only on the volume variation caused by the change in distance between the housing and the plunger. Variation of lifter stiffness due to a variation of the air volume fraction of the oil inside the high pressure chamber was accounted for. This calculation also reduced to an implicit equation, but was a function of plunger displacement only and independent of time. The equation was found by combining equations 5.3.3, 5.3.4, 5.3.8 and 5.3.23 (ignoring the bulk modulus of elasticity's variance with pressure and temperature) to be

$$\left(F_p^{prs}\right)^{n+1} = A_p^{prs}\left[(p_{hpc})^n - \frac{E_{oil}(p_{hpc})^n}{\phi_{oil}(p_{hpc})^n + \phi_{air}E_{oil}}\frac{(dh_{hpc})^n}{(h_{hpc})^n}\right] \tag{5.4.1}$$

where dh_{hpc} is the height variation of the plunger relative to the housing and h_{hpc} is the total distance between the plunger and housing. Subscripts n and $n+1$ represents the iteration steps.

A simple iteration program was written in MATLAB. (Equation 5.4.1 contains the fundamental equation used in the MATLAB program.) The lifter stiffness, as a function of plunger displacement and a pre-defined air volume fraction, ϕ_{air}, was calculated. This characterisation of the HLA was included in ADAMS as a single component force, represented by a different spline for each air volume fraction. (The use of single point forces are discussed in section 6.5.)

Figure 5.4.1 illustrates the effect of oil aeration on the lifter stiffness characteristics of the HLA model calculated from equation 5.4.1.

It is clear that aeration has a profound effect on lifter stiffness due to the immense compressibility differences between air and oil. Note that at zero plunger displacement, the lifter force is not zero, but has a value that balances the spring pre-load force, 179 N in this case. The force decreases steadily until it exerts no force on the valve train at which point any further lifter expansion is impossible and contact between lifter and follower is lost.

In the end, the model did not include any check valve operation, nor did it account for any leakage of oil through the annular slot. The following section describes the

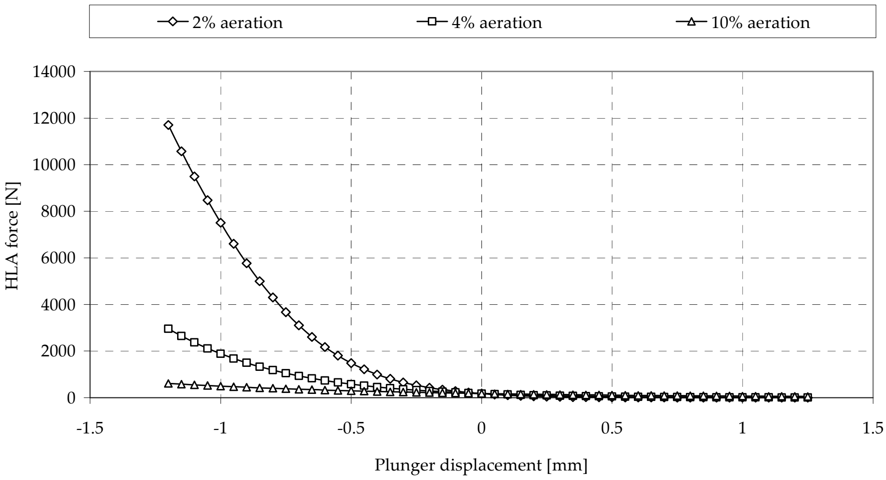

Figure 5.4.1: Force characterisation of simplified HLA model with regards to oil aeration fractions.

behaviour of these two mechanisms in detail which provides insight into the accuracy of the simplified model.

5.5 Influence of the HLA on valve train dynamics

Kreuter & Maas (1987) investigated the behaviour of the lifter under low, medium and maximum engine speeds respectively. They measured, amongst others, lifter displacement (lifter displacement or shortening is often referred to as lifter "collapse"), check valve displacement and actual valve displacement. The following section is an evaluation and study of their findings regarding the effect of hydraulic lifters on valve train dynamics.

5.5.1 Check valve behaviour

It was concluded that during low and medium engines speeds the lifter, more specifically the check valve, behaved normally. However, when considering high engine speeds, the behaviour of the check valve deviates from its normal operation. In essence, the check valve opens while it should remain closed and causes additional lifter collapse. This in turn causes contact loss between valve train components if the check valve opens during valve lift events, and causes a phenomena called "pre-collapse" if it opens during cam base circle events.

Firstly, during cam lift events, vibration of the check valve due to inertia forces, contact forces between check valve and check valve seat and pressure oscillations inside the high pressure chamber, could cause the check valve to open. As soon as the check valve opens, back-flow occurs and the lifter collapses, causing contact loss between valve train components. This malfunction mechanism could be visualised as sporadic buckling of one of the valve train components. Contact loss then occurs due to the remaining valve train components carrying momentum and not following the buckling displacement. Contact loss between components results in accelerated wear, shortening of engine life and engine noise.

Secondly, near the cam base circle event, where the check valve should have recently closed after leakage compensation, the check valve could become unstable due to erratic pressure oscillations. These pressure oscillations together with inertia forces prevents the check valve from returning to its seat. As soon as the next event begins, the pressure in the lifter rises and causes the check valve to finally close, but with a small delay. As a result of this delay there will be back-flow of oil through the valve, which causes a shortening in the lifter.

Pre-collapse causes some of the cam lift to be absorbed by the collapse of the lifter instead of driving the valve open. This causes the valve to open with a delay and thus decrease the valve opening time and ultimately engine performance. Eventual valve opening velocity also increases considerably and this could again lead to valve bouncing, contact loss between components and increased component wear.

Pre-collapse happens seldom and is difficult to predict and reproduce under test conditions. Still, pre-collapse is present in most valve train systems fitted with hydraulic lifters and can have large influences on the valve train dynamics. Kreuter & Maas (1987) found a reduction in valve opening duration of up to 10 camshaft degrees.

5.5.2 Oil leakage through annular slot

The leakage of oil through the annular slot caused by the gap between the plunger and housing could be described by referring to equation 5.3.21. It is clear that the leakage through the slot causes a viscous friction force on the side area of the plunger (equation 5.3.22). This force consists of a component that depends on plunger velocity. This means that the leakage causes a damping force that adds to valve train system damping.

5.6 Simplified model accuracy

In summary of the simplified model's shortcomings, the following is not taken into account:

1. Contact loss between valve train components caused by unstable check valve operation,
2. Lifter pre-collapse caused by unstable check valve operation resulting in a decrease in valve opening duration, and
3. Damping caused by viscous friction forces on the plunger side area caused by the oil flowing through the annular slot.

All of the above HLA operation mechanisms have relatively small effects on the overall valve train dynamics. The effect of check valve operation malfunction, which has the most prominent effect on the valve train system, only occurs in a small engine operating range. In addition to this, it is not repeatable and highly erratic and would be difficult to reproduce under test conditions.

The simplified model, existing without the above mechanisms, is considered to capture the primary functions of the HLA; taking the highly sensitive oil aeration effect into account, as well as having a realistic hydraulic force-displacement character, illustrated in figure 5.4.1. The simplified model is regarded as being sufficiently accurate for the objectives of this project.

Chapter 6

Flexible Body Based Model

6.1 Overview

As discussed in chapter 1, the internal dynamics and oscillations of springs cannot be ignored in a numerical model. Although the surge-mode approach model captures these effects, it also allows unlimited amplitude for the deviation displacement of the spring particles. Non-linear effects such as coil clash is thus not taken into account. This led to the development of a two-stage flexible body based model described in this chapter. The first stage is referred to as the detailed model, and the second stage is referred to as the equivalent model.

The detailed model consists of a detailed FEM model which accounts for the geometric non-linearity, as well as the interaction between windings of the spring. The model thus governs the non-linearity in stiffness and frequency. The flexible bodies are generated from a detailed ProEngineer solid model that was imported into PATRAN. Within PATRAN a mesh was created manually to ensure a controlled mesh size and mesh element distribution and placement. The model consists of three-dimensional wedge elements and one-dimensional gap elements. Mesh size control was important in order to locate gap elements at specific nodes throughout the model, as discussed in detail in section 6.4. A non-linear static analysis, as well as a modal analysis were performed on the detailed spring. The results were validated with a quasi-static spring compression experiment and the theoretical calculation of the spring's fundamental natural frequency.

The results of the detailed model were processed into force-deformation curves and used to generate the equivalent model's elements.

The equivalent model consist of one single subdivided element for each flexible body of the detailed model. Each single spring element's stiffness reflects the linear stiffness of the subdivided flexible bodies of the detailed model and was derived from the linear part of the detailed model's force-deformation curves. The non-linearity that results from the coil interactions was again modelled with the gap elements used in the detailed model. The single spring elements used were linear beam elements which were free to translate only in the longitudinal direction, thus resulting in a one-dimensional flexible body. The equivalent model was analysed and compared to the detailed model in respect of static non-linear compression, as well as modal frequencies.

The equivalent model was duplicated into ADAMS and the remaining valve train components were added as rigid bodies. The HLA being an exception, as discussed in section 5.3.

6.2 Spring stiffness and fundamental natural frequency

Before the spring modeling of this project commenced, a study into the calculation of two basic spring characteristics were performed namely; stiffness and natural frequency. The following section discusses this study in detail.

The external work done on an elastic member in deformation is transformed into strain, or potential energy. If the member is deformed a distance y, this energy is equal to the product of the average force and the deflection (Shigley *&* Mischke (1989)), or

$$U = \frac{R}{2}y = \frac{F^2}{2k} \tag{6.2.1}$$

This equation is general in the sense that it is applicable to both tension or compression and torsion, provided that the correct dimensions are chosen for k. (By replacing k with appropriate expressions, strain energy formulas for various simple loadings may be obtained.) Recall that the spring constant for an axially simple loaded bar is

$$k = \frac{AE}{l} \tag{6.2.2}$$

This equation does not apply to a long slender bar loaded in compression if there is a possibility of buckling. Also, when the word *simple* is used to describe the loading, the meaning is that no other loads are present and no geometric complexities are present. Thus, a bar loaded in simple tension is a uniform bar loaded by a tensile force, which is acting through the centre of the bar.

Similarly, the torsional spring rate of a solid round bar loaded by simple torsion is

$$k = \frac{GJ}{l} \tag{6.2.3}$$

By substituting equations 6.2.2 and 6.2.3 into equation 6.2.1 we have the strain energy for tension or compression and torsion respectively.

$$U = \frac{F^2 l}{2AE} \tag{6.2.4}$$

$$U = \frac{T^2 l}{2GJ} \tag{6.2.5}$$

To obtain an expression for the strain energy due to direct shear, consider the element with one side fixed in figure 6.2.1. The force F places the element in shear and the work done is,

$$U = \frac{F\delta}{2} \tag{6.2.6}$$

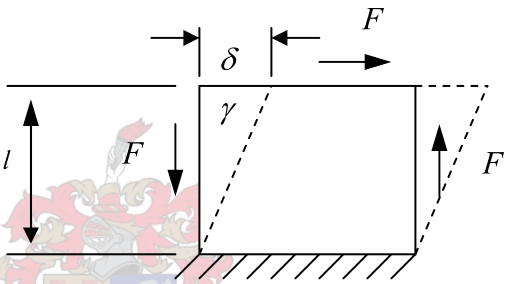

Figure 6.2.1: One side fixed infinitesimal element.

Since the shear strain is

$$\gamma = \frac{\delta}{l} = \frac{\tau}{G} = \frac{F}{AG} \tag{6.2.7}$$

we have the shear strain energy as

$$U = \frac{F^2 l}{2AG} \tag{6.2.8}$$

The force-deflection relations of springs are easily obtained using Castigliano's theorem. The theorem states: *"When forces act on elastic systems subject to small displacements, the displacements corresponding to any force, collinear with the force, is equal to the partial derivative of the total strain energy with respect to that force"* (Shigley & Mischke (1989).) Mathematically, the theorem of Castigliano is,

$$\delta_i = \frac{\partial U}{\partial F_i} \tag{6.2.9}$$

where δ_i is the displacement of the point of application of the force F_i in the direction of F_i. The total strain energy for a helical spring is composed of a torsional component and a shear component, as shown in figure 6.2.2. Strain energy caused by tension or compression forces is irrelevant and omitted. Using figure 6.2.2 we have

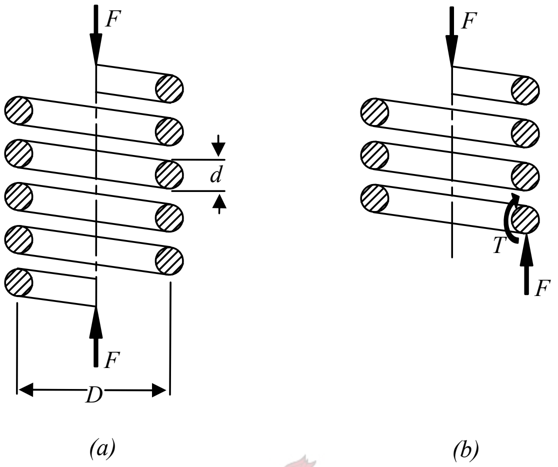

Figure 6.2.2: (a) Axially loaded helical spring; (b) free-body diagram showing that the wire is subject to a direct- and torsional shear.

$$U = \frac{T^2 l}{2GJ} + \frac{F^2 l}{2AG} \tag{6.2.10}$$

where

$$T = \frac{FD}{2} \tag{6.2.11}$$

$$l = \pi D N_a \tag{6.2.12}$$

$$J = \frac{\pi d^4}{32} \tag{6.2.13}$$

$$A = \frac{\pi d^2}{4} \tag{6.2.14}$$

Substituting equations 6.2.11 to 6.2.14 into equation 6.2.10, we have

$$U = \frac{4F^2 D^3 N_a}{d^4 G} + \frac{2F^2 D N_a}{d^2 G} \tag{6.2.15}$$

Then using Castigliano's theorem,

$$y = \frac{\partial U}{\partial F} = \frac{8FD^3N_a}{d^4G} + \frac{4F^2DN_a}{d^2G} \tag{6.2.16}$$

By defining the spring index as

$$C = \frac{D}{d} \tag{6.2.17}$$

equation 6.2.16 can be rearranged to yield

$$y = \frac{8FD^3N_a}{d^4G}(1 + \frac{1}{2C^2}) \tag{6.2.18}$$

With the term

$$(1 + \frac{1}{2C^2}) \tag{6.2.19}$$

being close to one, we have spring displacement as

$$y \approx \frac{8FD^3N_a}{d^4G} \tag{6.2.20}$$

With spring rate defined as

$$k = \frac{F}{y} \tag{6.2.21}$$

we have

$$k = \frac{d^4G}{8D^3N_a} \tag{6.2.22}$$

The displacement of the spring elements is governed by the wave equation,

$$\frac{\partial^2\psi(y,t)}{\partial t^2} = c^2\frac{\partial^2\psi(y,t)}{\partial y^2} \tag{6.2.23}$$

Here we are only interested in eigenvalues of this equation. The n'th mode eigenvalues, or natural frequencies, in radians per second, are

$$\omega_n = n\pi\sqrt{\frac{k}{m}} \qquad n = 1, 2, 3\ldots \tag{6.2.24}$$

The fundamental natural frequency is defined at $n = 1$, and this frequency, in radians per second, with $\omega = 2\pi f$, is

$$f = \frac{1}{2}\sqrt{\frac{k}{m}} \tag{6.2.25}$$

The moving mass of the spring can be defined in terms of the active coils only and thus we have from equations 6.2.12 and 6.2.14

$$m = \rho V = \rho A l = \rho \frac{\pi d^2}{4} \pi D N_a = \rho \frac{\pi^2 d^2 D N_a}{4} \tag{6.2.26}$$

Substituting equation 6.2.22 and equation 6.2.26 into equation 6.2.25 and simplifying we get the fundamental natural frequency, in Hertz, of a free-free helical compression spring.

$$f_n = \frac{2}{\pi N_a} \frac{d}{D^2} \sqrt{\frac{G}{32\rho}} \tag{6.2.27}$$

The above equation is used by Giorelli (2002) to verify the fundamental frequency of a FE valve spring model. Before attempting to validate this project's valve spring's natural frequency, a dimensional analysis should be performed on the equation 6.2.27.

Equation 6.2.27 is only valid for *Systeme International* (SI) dimensions. According to White (1999), there exist four primary dimensions from which all other secondary dimensions can be derived. These are: mass, length, time and temperature. Two of the most crucial secondary dimensions to this project are force and pressure. Expressing equation 6.2.27 dimensionally we have,

$$\{T^{-1}\} = \{L\}\{L^{-2}\}(\{ML^{-1}T^{-2}\}\{M^{-1}L^{3}\})^{\frac{1}{2}} \tag{6.2.28}$$

Expressing equation 6.2.28 in primary and secondary SI dimensions (kg, m, s, K, N, Pa) we have

$$\{s^{-1}\} = \{m\}\{m^{-2}\}(\{Nm^{-2}\}\{kg^{-1}m^{3}\})^{\frac{1}{2}} \tag{6.2.29}$$

Simplifying equation 6.2.29 we have,

$$\{s^{-1}\} = (\{Nm^{-1}\}\{kg^{-1}\})^{\frac{1}{2}} \tag{6.2.30}$$

The units for this project are different to that of the SI units. It has the dimensions of kg, mm, s, K, N and MPa. Equation 6.2.30 thus becomes

$$\{s^{-1}\} = (\{N(1000)mm^{-1}\}\{kg^{-1}\})^{\frac{1}{2}} \tag{6.2.31}$$

By comparing the two dimension systems (equations 6.2.30 and 6.2.31) a conversion factor is found that is necessary to keep the equation dimensionally homogenous:

$$\{s^{-1}\}_{kg,m,s,K,N,Pa} = \sqrt{1000}(\{s^{-1}\}_{kg,mm,s,K,N,MPa} = 31.62\{s^{-1}\}_{kg,mm,s,K,N,MPa} \quad (6.2.32)$$

6.3 Solid modeling

The final spring model was a combination of three modeling steps, each needed to represent the physical spring accurately (note the difference in terminology used for the physical spring and solid spring): The first, the so-called solid model, was modelled in ProEngineer. The second, the so-called FEM model, was modelled in PATRAN, and the third, the so-called dynamic model, was modelled in ADAMS. The FEM and dynamic model's required their preceding models as building blocks.

ProEngineer is an advanced CAD software package, incorporating Boolean operations to construct geometry in three dimensional space. Except for the cylinder head solid model, detail manufacturer's drawings of the remaining valve train components could only be obtained in JPEG format. This meant that all the solid models needed to be re-constructed in ProEngineer from a clean sheet.

The valve train assembly consists of 12 parts, listed in table 6.3.1. The scope of this project was to focus on the non-linearities of valve springs and the effect of its dynamics on the remaining valve train. The term valve train was defined to entail only one cylinder's inlet valve train components. This included one valve, one spring, one cam lobe, etc. Expanding the model into the entire valve train system would merely be a modeling duplication exercise. Until camshaft dynamics (camshaft resonance, camshaft torsional deflection, etc.) and its effect on the valve train needs to be investigated, the scope of this project would therefore only encompass the modeling of the inlet valve train components of cylinder one.

With the spring being an exception, the valve train components were modelled relatively simply. During modeling, mass, density and moment of inertia were kept in mind when decisions were made with regard to the level of detail required. (Appendix E contains all solid models of the valve train components.) Therefore most details from the manufacturer's drawings were included, with the following exceptions:

1. The camshaft model was modified for the sake of simplicity. Only cylinder one's valve train components were investigated and therefore the complete camshaft was redundant. Only one cam lobe was modelled onto a shortened, simplified

Table 6.3.1: Breakdown of valve train components.

Assembly	Components	Sub-components
Valve train	Cylinder head	
	Inlet valve seat	
	Inlet valve	
	Valve guide	
	Spring retainer	
	Hydraulic lash adjuster	HLA oil base
		HLA oil reservoir
	Camshaft	Cam
		Shaft
	Finger follower assy	Finger follower
		Roller
	Spring	

shaft. The camshaft was merely a rigid motion generator and its inertia and mass properties did not influence the dynamic model. This simplification therefore did not affect the valve train model.

2. Another component that was modified from the original manufacturer's design, was the valve guide. A thin plate was added around the guide, representing the seating surface of the valve spring. The thickness of the plate represents the thickness of the valve stem seal, which is positioned underneath the physical spring, as well. This allowed the valve spring to be positioned accurately to the correct precompressed length. The valve guide did not influence the dynamic model because it was a stationary part locked to ground or constrained to not move.

3. As was discussed in chapter 5, the geometry of the HLA is complex. In short the HLA consists of hydraulic valves, springs, oil chambers, moving parts, etc. A simplified version was modelled with the dynamic modeling requirements kept in mind. Eventually the HLA solid model consisted of two components; the HLA oil base component and the HLA oil reservoir component. The moving mass of the HLA oil reservoir component was critical and influenced the dynamic response of the valve train system. The geometry of the moving part was measured from a disassembled part and modelled to a high accuracy.

4. The valve spring retainer and the collets were merged and modelled as one solid. It was unnecessary to model these components individually, because their contribution to the valve train dynamics was merely as moving masses. Both components

are symmetric around their centre axis as well. As long as the combined mass of the components reflects accurately in the single solid model, this assumption remains acceptable.

Modeling dimensions of less than 1 mm in the SI units of metres, quickly became troublesome with ProEngineer automatically rounding off decimal places. The valve train components were therefore all modelled in millimetre and kilogram units. Unfortunately, this unit system was to remain the chosen system for this project and added a slight complication to unit systems and dimensional analysis in general.

Initially, a density of $7{,}850 \times 10^{-06}\,\mathrm{kg/mm}^3$ were chosen for all the components. ProEngineer calculated the mass of the components based on this initial density and the modelled volume of the components. All moving components were weighed using a NAGATA mass balance and compared to the initially modelled masses. The solid models' densities were adjusted according to the ratio of the weighed masses to that of the initially calculated masses. This resulted in all moving components having accurate mass properties such as densities and moments of inertia tensors.

Non-moving components' densities remained at the initially assumed value, their mass being irrelevant. Appendix E contains an exploded and assembled view of the valve train model, as well as tabulated mass properties calculated with ProEngineer.

The complexity of the spring's geometry was due to a varying pitch, a varying diameter and also ground ends. The Ford spring's varying pitch (decreasing the pitch to the spring's ends) is simply incorporated to allow the two end coils to end with a near zero pitch. This is done to maximise the spring's seating area once the ends get ground off perpendicularly to the spring's centre axis. The varying diameter however, is incorporated to allow the coils with bigger diameters to compress first. From equation 6.2.22 the following relation is deduced

$$k \propto \frac{1}{D^3} \tag{6.3.1}$$

Thus coil diameter, D, is indirectly proportional to stiffness, k. Approximately 1 coil has a small diameter and the 5 coils below it have equal bigger diameters. In the event of high engine speeds and/or excessive spring resonance, the bigger diameter coils will be allowed to clash, resulting in spring oscillation damping, while at least one coil will be stiffer and add room for linear compression. The top stiffer coil also "shields" the moving valve train components immediately above it from normal spring oscillations that are restrained to the less stiff bottom part of the spring.

An added advantage, although probably not the primary motivation for having a smaller diameter top coil, is that this allows the spring retainer, which fits into the top spring coil, to have a smaller diameter. With the retainer having a smaller diameter, the moving mass of the spring could be reduced, which in turns increases the fundamental natural frequency of the valve train system.

Thus, as can be deduced from the above and previous discussions, the complex geometry of the valve spring has a direct influence on the overall dynamic response of the valve train. This further motivates the attention to detail necessary to model the spring accurately.

The spring was modelled using a helical sweep of the cross section of the spring wire. Five different sections were modelled and merged together afterwards to form the complete spring. The first (bottom) and fifth (top) section had a constant pitch of 3,7mm, equal to the spring wire's diameter. The diameter of the helical sweep of the first section was a constant 22,7 mm. The sweep diameter of the top section varied from 18,7 mm to 18,1 mm. These sections also had a cut, which represented the ground-off ends.

The second and fourth sections had a linear varying pitch. The starting and ending pitch would be equal to the respective pitch angles of the spring sections adjacent to it, thus varying between 8,1 mm and 3,7 mm. Thus the second and fourth spring section joined the centre section to the two outer sections. Again the helical sweep diameter of the second section was a constant 22,7 mm, while that of the fourth section varied from 17,4 mm to 18,7 mm.

The centre section, section three, thus had a constant pitch of 8,1 mm and the helical sweep's diameter varied from 22,7 mm to 17,4 mm. Section three was the largest of all the spring sections, containing most of the constant pitch and constant spring diameter coils. The individual spring sections as well as the assembled spring is illustrated in figure 6.3.1.

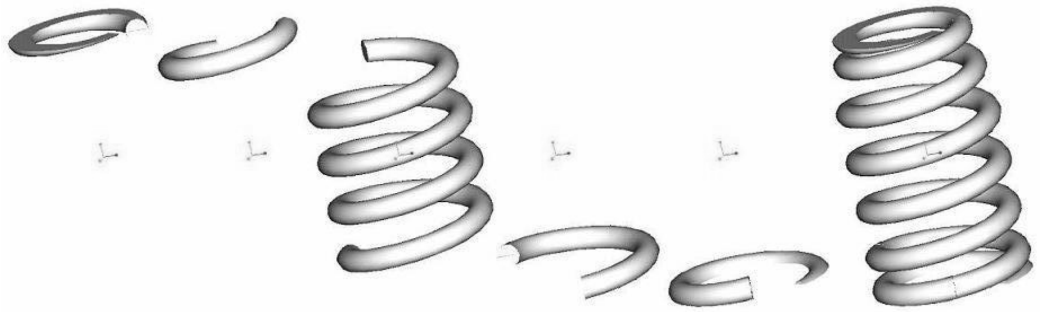

Figure 6.3.1: Spring construction from five sections.

The dimensions of these sections were partly found from a two dimensional manufacturer's drawing, and partly from measuring the physical spring and adjusting the size of the sections until a satisfactory representative spring was modelled.

Except for the above mentioned geometric modeling of the spring and other valve train components, extra detail were modelled into some of the components in preparation for their use in the FEM- and dynamic model. (This will be referred to as the second phase of solid modeling.)

In terms of the FEM model, only the valve spring solid model was further developed. As will be discussed in detail in section 6.4, a carefully controlled element mesh was planned for the valve spring FEM model. This mesh required extra detailing of the geometry of the solid model to assist in the meshing process. Although more geometric modeling was performed in the FEM software package environment, PATRAN, ProEngineer was used to construct the more complicated geometry.

The most prominent of these were datum curves representing the cross sections of the spring wire. These curves were required at intervals of 15 degrees. (15 degrees was the mesh size chosen for the FEM elements of the spring wire.) This was accomplished by constructing datum planes at 15 degree angles apart and then constructing a datum curve at each intersection between the datum plane and the spring wire. In addition to this, the two spring sections that contained ground-off ends, also had to include these datum curves on their un-cut spring sections.

Two models were finally exported to PATRAN as *Initial Graphics Exchange Specification* (IGES) files. (IGES was originally developed in 1979, by the NBS, to facilitate the transfer of geometry and annotations from one CAD/CAM system to another. IGES is the predominant format used for the transfer of geometry information.) One model contained the complete spring with datum curves, the other only consisted of two un-cut end sections. In PATRAN these two models were overlaid and produced a solid model consisting of seven spring sections and 219 datum curves (refer to figure 6.3.2).

In terms of preparing the solid model for the dynamic model, various steps and components needed to be prepared. These included datum points and datum curves at strategic positions. The datum points would be used to place and orientate mechanisms in the dynamic model, such as at the centre of the inlet valve for a translational joint mechanism. Datum curves were used to define curve-to-curve constraints (later developed into curve-to-curve contact) between contact surfaces. Two contact surfaces were modelled with curve constraints, the first one being the cam-on-roller contact and the second one being the follower-on-valve tip contact.

The final solid modeling step was the assembly of the various valve train compo-

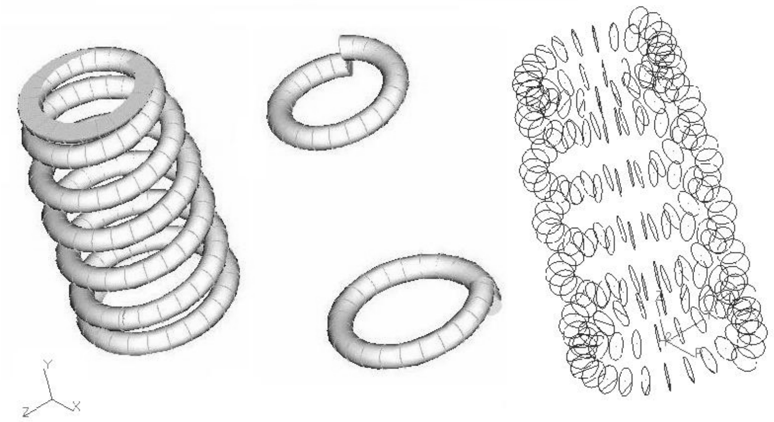

Figure 6.3.2: ProEngineer and PATRAN solid models showing constructed datum curves.

nents in their correct positions. Careful study of the physical valve train system and a clear understanding of the valve train system operation, as well as a well defined set of project objectives, were required before commencing modeling of mechanisms and constraints for the dynamic model. (The valve train operation will be discussed in detail in the dynamic model section, section 6.5.)

As far as the assembly of the valve train solid models was concerned, only spatial positioning was important. The geometry of the components delegated their placement. Only the finger follower and HLA oil reservoir component had a complex placement.

The finger follower needed four constraints to enable correct placement. These included;

1. plane alignment of the cam lobe and the finger follower roller,
2. placing the roller tangentially on the cam lobe,
3. placing the finger follower tangentially on the valve tip, and finally
4. constraining the centre point of the finger follower's spherical cup, onto the HLA oil base component's axis of symmetry.

The final part to be assembled was the HLA oil reservoir component. As discussed in detail in section 5.1, the primary function of the HLA is to remove lash in the valve train system. Under ideal conditions there exist no gaps between the finger follower and its neighbouring components. Therefore the finger follower was assembled tangentially to all its neighbouring components before the moving part of the HLA was assembled. The HLA oil reservoir component's spherical end was constrained to be in contact with the finger follower's spherical cup and its axis of symmetry constrained on the HLA oil base axis of symmetry.

ADAMS/View was used as the dynamic modeling software package and geometry was transferred to ADAMS/View as Parasolid files. This was accomplished by using ProEngineer's Wildfire version 2.0, which is based on the Parasolid kernel. For those CAD systems based on the Parasolid kernel, there are many benefits in transferring geometry in Parasolid files over that of using IGES files. ADAMS/View creates solid bodies from the Parasolid information that allows further Boolean operations, as well as the selection of geometric features such as the centre of a circle.

Once the solid spring model was imported into PATRAN and the solid model assembly was imported into ADAMS/View, the second phase of the solid modeling was completed. Section 6.4 discusses the solid modeling performed in PATRAN.

6.4 FEM model

As mentioned in section 6.1, the spring was modelled in two stages. The detailed model consists of flexible bodies that enable internal spring surge of the spring to be simulated. The interaction between two neighbouring coils gives the non-linearity of the total spring. The following sections describe the modeling of the detailed spring in detail.

6.4.1 Modeling flexible spring bodies

The flexible bodies, representing one quarter of a spring winding, comprise of six flexible sections, representing the spring wire every 15 degrees of the spring wire. Each flexible section is composed of 12 wedge elements, stacked to form a "circular" section. In essence, these bodies, sections and elements, illustrated in figure 6.4.1, are the building blocks of the detailed spring model.

The choice of elements was deliberate. Total spatial control of the elements and nodes were desired in order to place gap elements' connection points at specified locations. In short, a single node was needed at the centre of each spring coil cross section. For such a specification, the more commonly used tetrahedral elements, normally used with an auto-mesh function, did not suit the application.

A tri-parametric element was needed and the wedge element was chosen. In theory, the wedge element is identical to the brick element but with a collapsed side. Most solid elements theory are direct extensions of plane elements. The extension consist of adding another coordinate and another displacement component. For simplicity the *Constant*

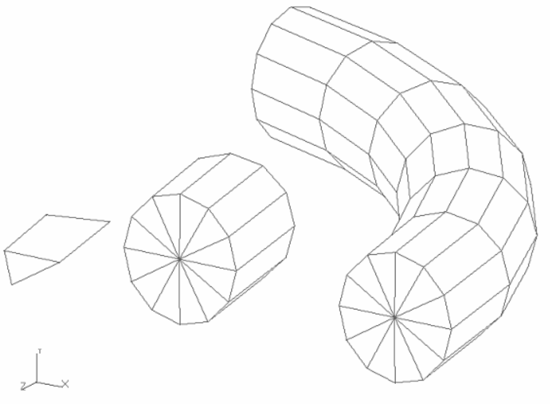

Figure 6.4.1: Detailed spring model building blocks.

Strain Triangle (CST) and *Linear strain triangle* (LST) plane elements, instead of the wedge or hexahedron elements, are discussed in appendix F.

A choice of wedge element had to be selected from NASTRANS's *Wedge*6 and *Wedge*15 elements, represented here by the CST and LST plane elements respectively (Cook (1995)). As discussed in section 6.2 and shown in figure 6.2.2, the element loads of an axially loaded spring has a torsional component and a shear component. From the discussion in appendix F, the LST element is more suited for bending application and therefore the *Wedge*15 element, representing the LST element in theory, was chosen to model the spring.

After the element choice was made, the finite element modeling could commence. Two solid models were exported to PATRAN from ProEngineer from which the FEM model was created. In PATRAN these two models were overlaid and produced a solid model consisting of seven spring sections and 219 datum curves (refer to figure 6.3.2). The difference between the two models are only contained in the ends of the spring. One being ground-off, and the other not. This was done for a specific reason, as will become clear shortly, but firstly, the construction of the normal spring flexible body section will be discussed.

Besides the ground-off end sections, the modeling of the spring was relatively simple. Each wedge element was created between two neighbouring datum curves created in ProEngineer from the spring wire's cross section every 15 degrees apart. Each element was carefully positioned and the element orientations were all identical, pointing radially outwards. Figure 6.4.2 illustrates the spring elements without the ground-off sections.

The ground-off sections were more complicated. First of all, the centre node of

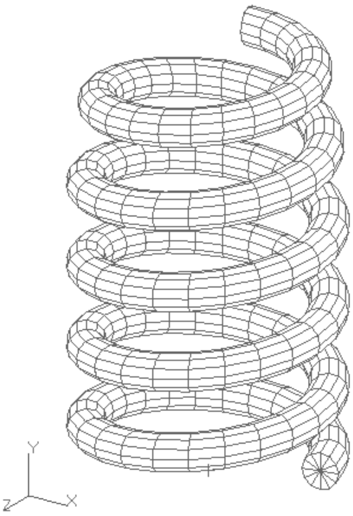

Figure 6.4.2: Detailed spring elements without ground-off end sections.

the wedge elements were no longer coincident with the spring wire's centreline. The spring's centreline was used to connect gap elements to the flexible bodies, and could not be ignored. Secondly, more and more element faces needed to be part of the flat ground-off face as an increasing width of the spring wire gets ground off at the end of the spring coil. This meant that special care had to be taken to position the nodes on the circumference of the spring's cross section. Figure 6.4.3 illustrates two different ground-off sections and how these nodes were moved.

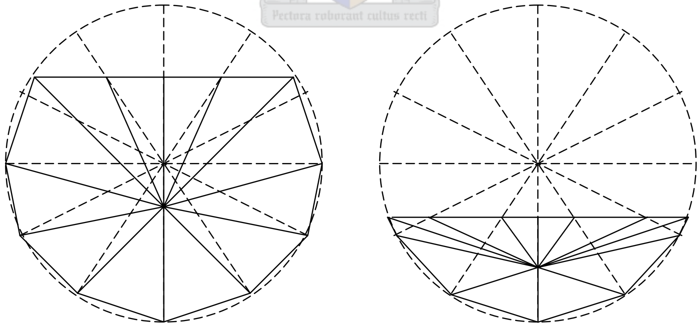

(a) *(b)*

Figure 6.4.3: Spring ground-off cross sections with the ground-off face (a) above, and (b) below the spring wire centreline.

The reason for importing the solid geometry of the unground-off ends was thus to assist in this complicated meshing procedure. The end result was that both spring ground-off sections had a neatly structured element architecture. This enabled the accurate positioning of gap elements and *Multi point constraint* (MPC) elements, as will be discussed shortly. Figure 6.4.4 illustrates the complete top ground-off section.

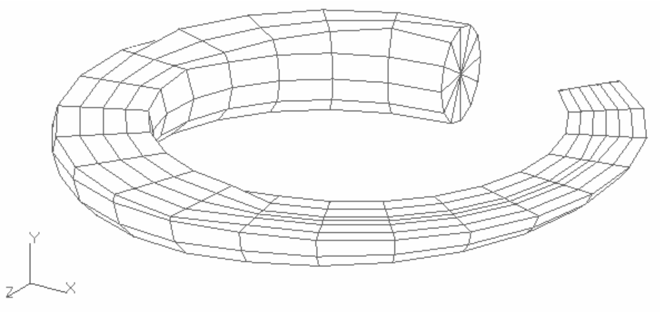

Figure 6.4.4: Top ground-off spring section.

6.4.2 Modeling contact

Coil interaction between two neighbouring spring coils gives the non-linearity of the total spring. A strategy was needed to model this into the spring and NASTRAN's gap elements were used together with a non-linear static analysis type.

In a linear static analysis we implicitly assume that the deflections and strains are very small and the stresses are smaller than the material yield stresses. This linearity implies that any increase or decrease in the load will produce proportional increase or decrease in displacements, strains and stresses. In many structures, at or near failure (yield) loads, the deflections and the stresses do not change proportionally with the loads.

Either the stresses are so high that they no longer obey Hooke's law (linear stress to strain relationship) or else there are such large deflections that the compatibility equations (strain to displacement relationship) cease to be linear. These two conditions are respectively called material and geometric non-linearity. Another type of non-linearity arises due to the presence of gaps in a structural model. Since the stiffness of a structure changes substantially after an open gap closes or a closed gap opens, an iterative (non-linear) analysis is necessary if gap elements exists in the FEM model.

To represent and model coil contact in the spring model, NASTRAN's CGAP elements were used. Referring to figure 6.4.5, the following is defined:

$\vec{v}$ = vector defined as the action direction of the gap element;
$k1$ = stiffness of open gap element;
$k2$ = stiffness of closed gap element;
$1, 2$ = node numbers defined as connecting points of the gap element.

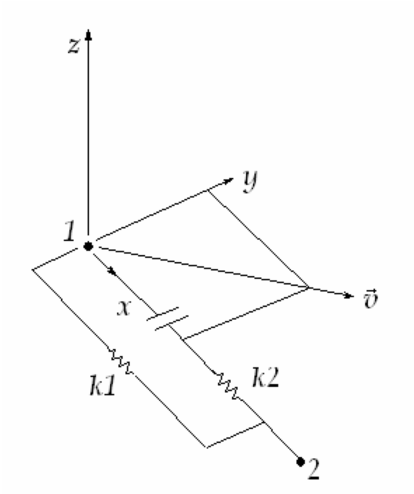

Figure 6.4.5: Graphical representation of the *CGAP* element.

In principle, modeling the gap elements was simple. At the ends of each flexible spring section, gap elements were positioned and connected to the nodes on the spring wire's centreline, including the ground-off section's centreline. The initial gap opening had to be specified accurately. The choice of solid wedge elements resulted in a spatially symmetric mesh. The initial gap openings were simply the initial distance between the connecting nodes, minus the two halves of the spring wire diameters. Figure 6.4.6 illustrates the gap elements and their position.

The gap elements open stiffness, $k1$, was specified to be small enough as to be negligible, allowing the linear wedge elements to define the stiffness of the spring prior to contact. The closing stiffness, $k2$, was characterised by the spring's wedge element properties being dependant on the final value for the Young's modulus of elasticity, E, chosen for the spring's material. A small cube with unit dimensions (refer to figure 6.4.7) and consisting out of spring material, together with equation 6.2.2, was used to calculate the gap stiffness upon gap closing.

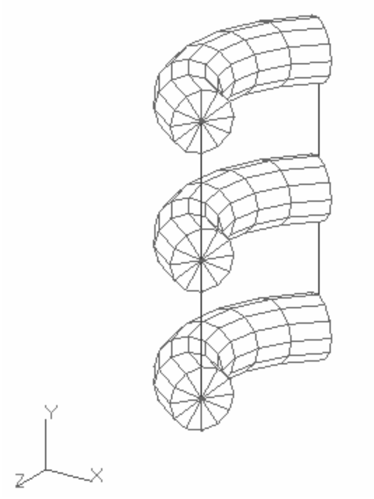

Figure 6.4.6: Flexible spring sections with gap elements.

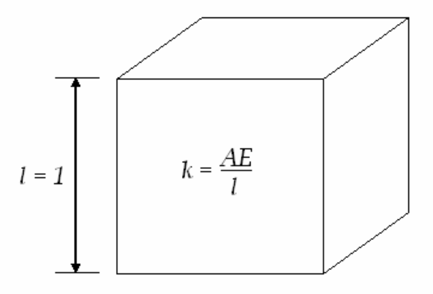

Figure 6.4.7: Small cube to calculate spring material contact stiffness.

6.4.3 Detailed spring model boundary conditions and constraints

Constraints had a direct influence on the spring's static and dynamic behaviour. Therefore, some special constraints were incorporated. NASTRAN's *Rigid Body Element, type 2* (RBE2) was used.

Using RBE2 elements, defines a rigid body link between an arbitrary number of nodes. One independent node is selected and an arbitrary number of dependant nodes are selected. Degrees of freedom is also selected and assigned to the nodes and this enables the modeling of complicated constraints.

In the case of the physical spring, the two ends are the only parts of the spring that are constrained. Both ends are assumed to remain flat against the operating surfaces. All nodes on the bottom ground-off surface remain in contact with the spring seating surface, and all the nodes at the top ground-off surface remain in contact with the spring retainer. In addition to this, all the nodes in contact with these two surfaces are allowed to expand in the radial direction. These specifications determined that the spring was constructed in cylindrical coordinates.

The RBE2 elements were applied to the top and bottom spring sections as two separate application concepts. Firstly, the nodes on the spring's ground-off surfaces were connected to the nodes on the spring wire's centreline, as illustrated in figure 6.4.8. Secondly, all the nodes on the spring wire's centreline were connected to the single node on the spring's principle axis of symmetry. One for the top section and one for the bottom section.

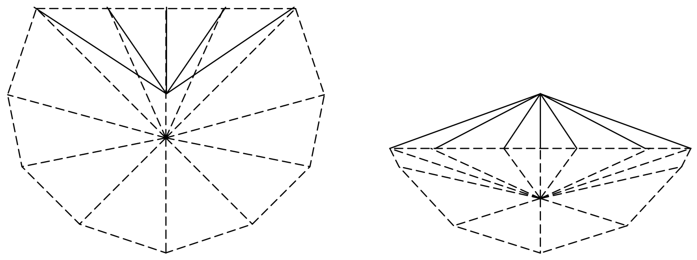

(a) *(b)*

Figure 6.4.8: Spring ground-off cross sections with MPC (solid lines). The ground-off face (a) above, and (b) below the spring wire centreline.

The idea of the first application was to ensure that the nodes on the ground-off surface remain in the same plane. In addition to this, the applied force was distributed to all the nodes on this surface. All six degrees of freedom were dependant on the single node's degrees of freedom.

The second application was firstly done to distribute the load from the single node on the spring's principle axis of symmetry to the single node of the first MPC application (which in turn distributed it onto the surface of the ground-off end).

Secondly, and more importantly, the degrees of freedom was specified to allow the nodes on the spring wire's centreline (and therefore the nodes on the ground-off surfaces attached to it) to expand radially, while constrained to move with the surface of the spring retainer.

This was accomplished by leaving the T_r-direction independent, and the T_θ, T_z, R_r, R_θ and the R_z dependant on the node on the principle axis of symmetry. Furthermore it is recommended by MSC that a rectangular coordinate system should be used for any grid point that lies on the polar axis. Thus the two nodes chosen to be the independent nodes for the second application of the MPC's, were modelled in rectangular coordinates.

These two nodes were only free to move in the T_y-direction. The final result of the MPC elements are illustrated in figure 6.4.9 showing the top ground-off section only. The only difference between the top and bottom ground-off surfaces is that the bottom ground-off surface's centre node was constrained in all six degrees of freedom.

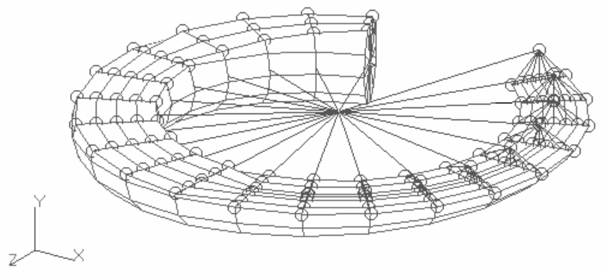

Figure 6.4.9: Top ground-off spring section with MPC elements.

The modeling of the MPC elements concluded the modeling of the detailed spring elements. The following section discusses the characterisation of the detailed spring model by adjusting the material properties.

6.4.4 Spring characterisation

By modeling the spring geometrically as accurately as possible, including realistic contact element properties through gap elements and constraining the spring correctly, the model was assumed to be an accurate representation of the physical spring. The only outstanding feature was to characterise the spring's material properties. This was accomplished by adjusting the material's Young's modulus, E, the Poisson's ratio and the spring material's density.

The spring's density was calculated in a similar manner to the other valve train components, by using the volume calculated with the solid model in ProEngineer and adjusting the density value until the spring's solid model had an aggregate mass equal to that measured. The end result was a density of $7{,}375 \times 10^{-6}\,\mathrm{kg/mm}^3$. The Poisson's ratio was assumed to be 0.3.

The spring's Young's modulus value was found through performing a static nonlinear compression analysis of the spring with a total load of 800 N. The displacement of the top node was requested and written to a file for every two percent of the total applied load. (This process will be discussed in detail in subsection 6.4.5.) This result was compared to the quasi-static compression experiment discussed in section 3.1.

The results from this experiment was used to determine the Young's modulus of elasticity iteratively with NASTRAN. A final value of $E = 220 \times 10^3$ MPa was found. The gap element closing stiffness was also updated with the new E value at every iteration analysis by using equation 6.2.2 and figure 6.4.7. The comparison between the FEM analysis and the experimental spring compression is illustrated in figure 6.4.10.

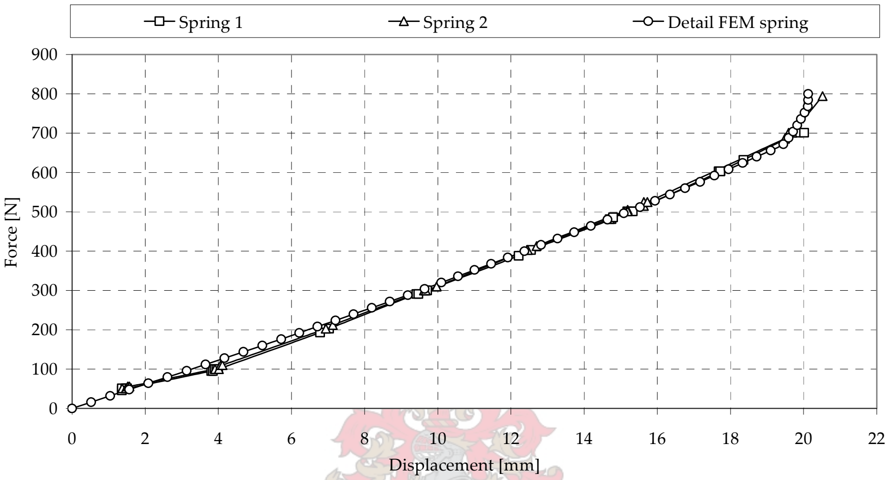

Figure 6.4.10: Spring static compression measurement results compared to detailed FEM model non-linear static compression analysis.

The detailed spring model thus compared very well with the actual spring with respect to a quasi-static compression. The next step was to compare it dynamically by performing a modal analysis on the detailed spring model.

All constraints and loads were removed and NASTRAN's modal analysis calculation was performed on the spring. By removing all constraints, the first 6 modes are the rigid body movements having frequencies of near zero Hertz. The remaining modes were useful and by keeping the result of dimensional analysis (equation 6.2.32) in mind for correlating the frequencies dimensionally, the next 10 mode shapes are shown in table 6.4.1 and some of these are illustrated in figure 6.4.11.

Giorelli (2002) used equation 6.2.27, derived in section 6.2, to verify the fundamental frequency of a finite element valve spring model. This verification was also performed on this project's spring and the calculation is shown in equation 6.4.1. The physical values used in this equation were gathered from the manufacturer's drawing and the

Table 6.4.1: Calculated mode shape frequencies of the detailed spring model.

Mode shape number	NASTRAN frequency [Hz]	Corrected frequency [Hz]	Mode description
7	14.05	444.27	1st compression Y
8	16.45	520.19	1st lateral bending Z
9	16.53	522.72	1st lateral bending X
10	16.65	526.52	1st rotation around Y
11	27.59	872.47	2nd compression Y
12	30.95	978.72	2nd lateral bending Z
13	31.17	985.68	2nd lateral bending X
14	31.71	1002.76	2nd rotation around Y
15	39.41	1246.25	3rd compression Y
16	44.21	1398.04	3rd lateral bending Z

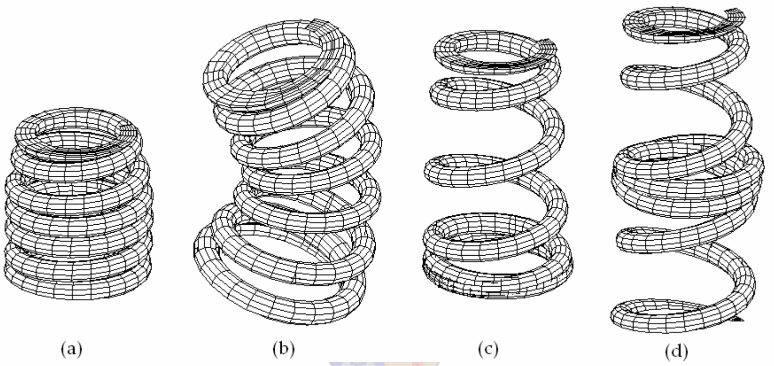

Figure 6.4.11: Detailed spring mode shapes at (a) 444,27 Hz, (b) 520,19 Hz, (c) 872,47 Hz and, (d) 1246,25 Hz.

FEM model results:

$$\begin{aligned} f_n &= \frac{2}{\pi N_a} \frac{d}{D^2} \sqrt{\frac{G}{32\rho}} \\ &= \frac{2}{(3.14)(5.75)} \frac{(3{,}7\,\text{mm})}{(23{,}5\,\text{mm})^2} \sqrt{\frac{(84{,}615 \times 10^{3)}\,\text{MPa}}{32(7{,}375\,\text{kg/mm}^3)}} \\ &= 444{,}99\,\text{Hz} \end{aligned} \tag{6.4.1}$$

By comparing the result of 444,99 Hz from the calculation shown in equation 6.4.1, theoretically derived in section 6.2, with the first mode shape frequency of 444,27 Hz derived from FEM in table 6.4.1, it was concluded that the detailed spring model was adequately accurate with respect to stiffness and material properties.

This concluded the modeling of the detailed spring. The next modeling phase consisted of modeling the equivalent spring from the force-deflection curves of the detailed model.

6.4.5 Generating force-deflection curves

As mentioned before, the equivalent model consist of one single element for each flexible body of the detailed model. Each single element's stiffness reflects the linear stiffness of the flexible bodies of the detailed model and was derived from the linear part of the force-deformation curves. The non-linearity that results from the coil interactions, represented by the non-linear sections of the force-deflection curves, would later be added into the dynamic model by superimposing a non-linear force on each linear element. This concept is illustrated in figure 6.4.12 where a detailed spring section is replaced by a single linear flexible spring element containing a superimposed non-linear force. For the equivalent model, the non-linearities were also incorporated by the same gap elements used in the detailed model.

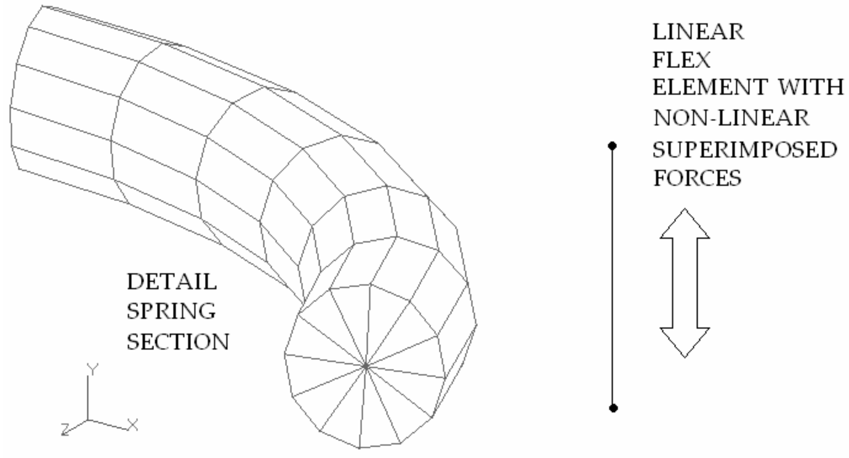

Figure 6.4.12: Dynamic spring element progression from detailed spring.

All information needed to construct the equivalent- and dynamic spring model is processed from the force-deflection curves generated by the static non-linear compression analysis of the detailed spring in NASTRAN. From the basis of using one flexible spring element per detailed spring section, spanning 90 degrees of the spring's coils, 22 sections were calculated to represent the detailed spring, roughly representing five spring coils.

Isaac Du & Chen (2000) specified that 20 Craig-Bampton (Craig & Bampton (1968)) axial mode sets, up to 7000 Hz, were necessary to have a good representation of static and dynamic deformation in *Internal Combustion* (IC) engine valve springs. Referring to the theory of modal analysis of multi-degree of freedom systems (discussed in section 4.3), we have the following undamped equation of motion for n masses and n springs, resulting in n equations of the form

$$m_i \ddot{h}_i = k_i(h_{i-1} - h_i) + k_{i+1}(h_{i+1} - h_i) \quad \text{for} \quad i = 1\,,\, 2,\, \ldots,\, n \tag{6.4.2}$$

The n eigenvalues are determined from the characteristic equation given by

$$\det(\lambda I - \bar{K}) = 0 \tag{6.4.3}$$

which gives rise to an nth-order polynomial in λ. Solving the determinant of this nth-order polynomial results in n eigenvalues, or natural frequencies. Having 22 linear elements available meant that it could be represented by 22 masses and springs that could calculate 22 axial modes sets. Thus exceeding the Craig-Bampton minimum mode sets requirement.

The detailed spring analysis is run with an output request that requests the output of node displacements in steps of two percent of the total applied load. This resulted in large data files that needed to be analysed. The size of the files made it impractical to pick through the data manually and a DELPHI computer program was written to analyse the data. In short, this DELPHI program searched and extracted result sets of user defined nodes and elements.

Naturally, the 22 spring elements had 23 nodes where the equivalent detailed spring sections were attached to one another. The gap elements were also attached to these 23 nodes. Only the force-deflection characteristics of these nodes were important. The node numbers of these nodes were renumbered in NASTRAN to distinguish them clearly from the thousands of other nodes. These node numbers were one of the two inputs to the data processing DELPHI program. The other input was the original location of the nodes in the global coordinate frame, or differently put, vertical heights of each of these nodes. This second input was used to perform the following tasks and calculations:

1. Import the data file, which was the $.f06$ extension file of NASTRAN's output,

2. import the node numbers of the nodes being searched for,

3. import the original global z-coordinate, or vertical heights, of these nodes,
4. search and record the z-coordinates of each of the designated nodes at each load step,
5. calculate the relative displacement between two nodes that will ultimately form the two connection nodes of their single equivalent spring element. Thus, calculate the force-deflection curves:

$$\begin{aligned} s_{\,i,j+1} &= \triangle z_{\,i+1,j+1} - \triangle z_{\,i,j+1} \\ &= (z_{\,i+1,j+1} - z_{\,i+1,j}) - (z_{\,i,j+1} - z_{\,i,j}) \end{aligned} \tag{6.4.4}$$

where $s_{i,\,j+1}$ = displacement of spring section i at time $j+1$;

$z_{\,i+1,j+1}$ = z-coordinate of node $i+1$ at time $j+1$;

$z_{\,i+1,j}$ = z-coordinate of node $i+1$ at time j;

$z_{\,i,j+1}$ = z-coordinate of node i at time $j+1$;

$z_{\,i,j}$ = z-coordinate of node i at time j.

and finally,

6. write a text file that contains all the force-deflection data.

The result was that the text file contained force-deflection data of 22 spring sections. The data was read into a spreadsheet to linearise the spring sections and separate the linear part from the non-linear parts of the force-deflection curves. As an explanation of this process, spring section 16 will be discussed. Figure 6.4.13 contains the original force-deflection curve for spring section number 16.

As can be seen from this figure, the spring section behaved perfectly linearly until an applied force of 480 N was reached. Following an increase in applied force, the behaviour was again relatively linear (only with a different gradient, or stiffness) until an applied force of 704 N was reached. A linearisation force of 704 N was used to linearise the force-deflection curve. What this meant was that a straight line was drawn through zero and the applied force of 704 N, representing the linear stiffness of spring section number 16, and all forces above or below this linearisation force was simply added onto the non-linear force-deflection curve, shown in figure 6.4.14. The linear stiffness of section 16, k_{16}, thus being the gradient of the linearisation curve. In the case of section 16,

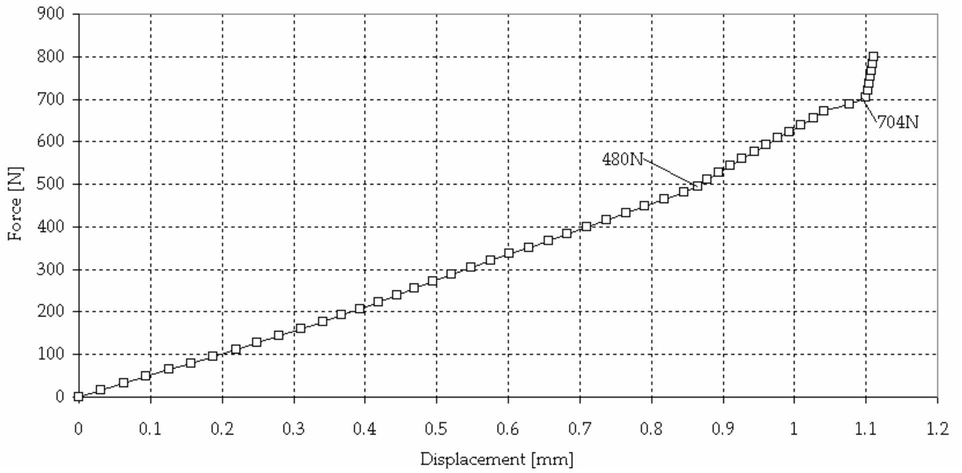

Figure 6.4.13: Original force-deflection curve for spring section number 16.

704 N corresponds to a section displacement of 1,1 mm, thus

$$\begin{aligned} F_i &= k_i s_i \\ k_{16} &= \frac{F_{16}}{s_{16}} \\ &= \frac{704\,\mathrm{N}}{1{,}1\,\mathrm{mm}} \\ &= 640\,\mathrm{N/mm} \end{aligned} \tag{6.4.5}$$

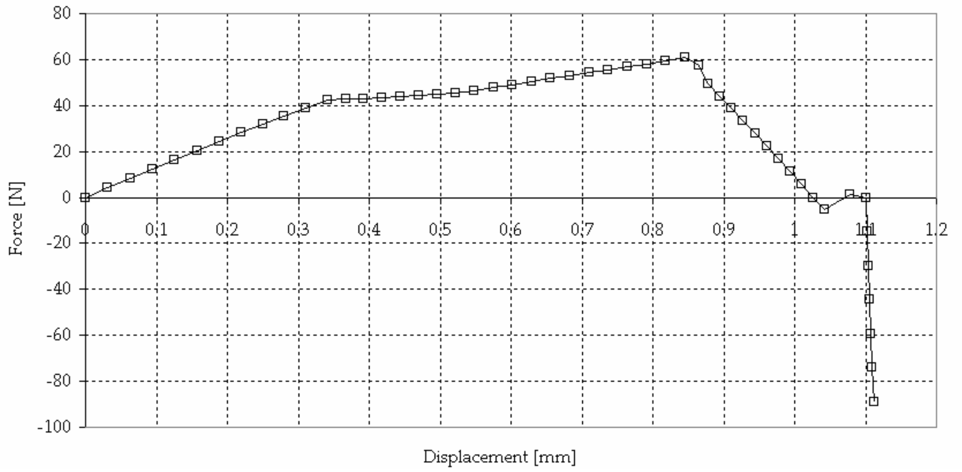

Figure 6.4.14: Non-linear part of original force-deflection curve for spring section number 16.

At this point, 22 spring elements were defined, which had 22 linear stiffness values, as well as 22 non-linear force-deflection curves. The next step was to calculate the individual mass of each spring element.

The ProEngineer solid model was used to perform this calculation by cutting the solid spring into the 22 individual spring sections. (Table G.1 in appendix G contains the discretised information of the detailed spring.) The equivalent spring was constructed from this tabulated information. The equivalent spring was firstly simulated in NASTRAN and compared with the results obtained from the detailed spring simulation before being duplicated into ADAMS.

6.4.6 Constructing the equivalent spring

From table G.1 all information was available to construct the equivalent spring. After spring model verification was completed in the PATRAN environment, the spring would be duplicated in ADAMS. The primary difference between the PATRAN equivalent spring model and that of the ADAMS model was in the application of the non-linear contact between neighbouring coils. The PATRAN model still implemented the gap elements similar to that of the detailed spring model. The ADAMS model used *Single component force* (SCF), defined by splines such as the force-deflection curve of figure 6.4.14, superimposed onto the linear spring elements.

The equivalent spring consisted of 22 single flexible elements. Each element's mass was distributed into two masses, concentrated at the two ends of the spring elements. The ratio of all the mass elements distribution was 1:1. Only the two spring elements at the ends of the equivalent spring had a mass distribution of 1:2. This was a rough estimation of the spring sections's active part (one third of the total mass) compared to the spring section's inactive part (two thirds of the total mass).

One two-dimensional beam element was used for each flexible spring element. The beam element was defined through a Young's modulus value (equal to that of the detailed spring model), individual element length, individual element cross sectional area and individual material density.

The element length was defined as the global y-length of the corresponding detailed spring section. With the chosen Young's modulus, linear spring stiffness known from table G.1 and the element y-length, the cross sectional area of each element was calculated with equation 6.2.2. Finally, the density for each spring element was calculated simply by $\rho = m/V$.

The gap elements were modelled similarly to the gap elements used in the detailed model. Care had to be taken when defining the connecting nodes of the gaps, seeing that one gap element spanned more than one single spring element. Reference to the detailed model was essential for this step. Again, the initial gap openings were simply the initial distance between the connecting nodes, minus the two halves of the spring's wire diameters. (Table G.2 of appendix G contains the equivalent spring model's beam element properties.)

The equivalent spring was modelled in cartesian coordinates and only had one degree of freedom. Only longitudinal displacements were allowed and this resulted in a one-dimensional flexible body. Thus, all nodes were constrained in the T_x, T_z, R_x, R_y and R_z coordinates and free in the T_y-direction. The bottom node was pinned to prevent rigid body movement.

The first analysis performed on the equivalent spring was the non-linear static analysis in which the spring was simply compressed with a total load of 800 N. The result was compared with the non-linear, static analysis performed on the detailed spring and is illustrated in figure 6.4.15. This plot also illustrates the error as an percentage. It is shown that the results compare consistently with an average error of 4% and a maximum error of 7%.

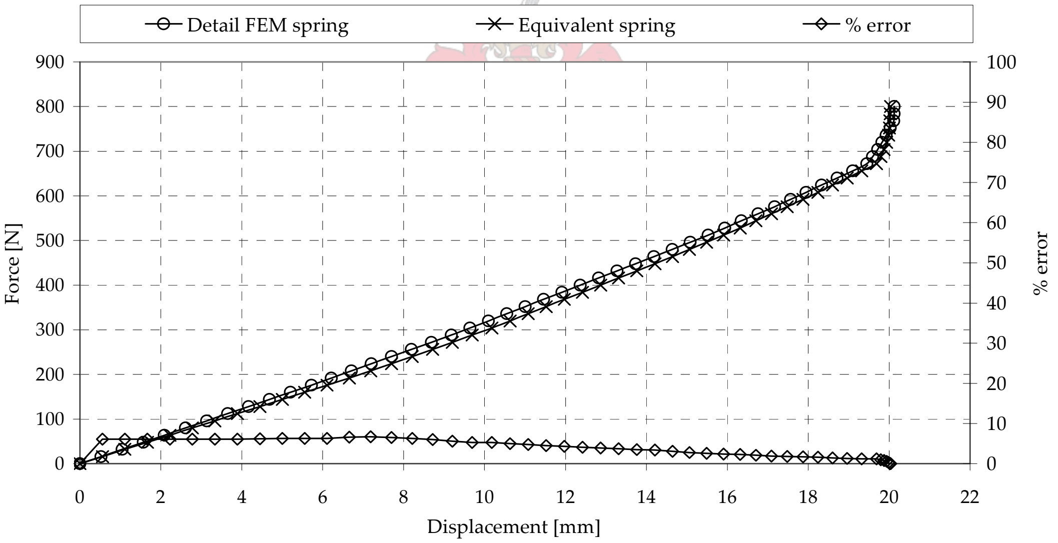

Figure 6.4.15: Error between the detailed spring and the equivalent spring static deflection.

The second verification was done through a modal frequencies analysis. Figure 6.4.16 illustrates the first three mode shapes compared to the un-deformed equivalent spring. Keeping in mind that only the longitudinal mode shapes of the detailed spring could be used. Table 6.4.2 illustrates the comparison of mode shape frequencies.

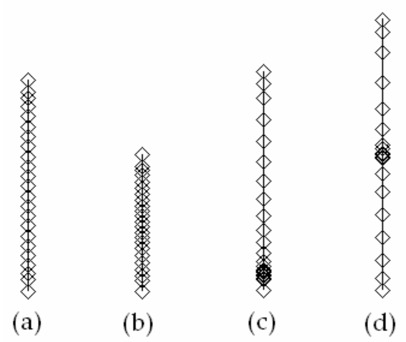

Figure 6.4.16: (a) Un-deformed equivalent spring model. Mode shapes at (b) 429,97 Hz, (c) 845,90 Hz, and (d) 1272,63 Hz.

Table 6.4.2: Comparison of mode shape frequencies between the detail spring and the equivalent spring model.

Detailed spring		Equivalent spring		
Mode shape number	Mode shape frequency [Hz]	Mode shape number	Mode shape frequency [Hz]	error [%]
7	444.27	7	429.97	3.2
11	872.47	8	845.90	3.0
15	1246.25	9	1272.63	-2.1

The above results show that with a much simpler equivalent model, satisfactory results are found. The calculation of the equivalent model is also considerably faster and model efficiency is vastly improved. These findings support the construction of the dynamic model based on the equivalent model.

By completing the verification of the equivalent spring model successfully, the FE modeling is concluded. The following sections discuss the construction of the dynamic spring model, as well as the adding of the remaining valve train components that leads to the synthesis of the complete dynamic valve train model.

6.5 Dynamic model

The complete dynamic model was constructed in ADAMS, with models developed and information acquired from the solid- and FEM models. The dynamic model contained all the components of one inlet valve train system. On completion of the dynamic model, a complete valve train model was available for analysis of valve train dynamics, as illustrated in chapter 8.

Schamel (1989) described, in detail, the possibility of decoupling the spring dynamically from the remaining valve train components without a compromise of accuracy. In short, due to the large difference in stiffness between the valve spring and the combination of the remaining valve train components (the HLA being the exception), the computation of the dynamic component of the spring force can be decoupled from the computation of the valve train dynamics.

For this reason, all the remaining valve train components could be modelled as rigid bodies, again with the exception of the HLA model. The focus was thus placed merely on the valve spring- and HLA dynamics.

As was mentioned in section 6.3, a clear understanding of the valve train system's operation was required before commencing modeling of mechanisms and constraints for the dynamic model. The following section describes the physical valve train operation in detail.

6.5.1 Valve train operation

Various valve train configurations are being used in poppet valve IC engines. The most common are the centre pivot finger-, the direct acting-, the pushrod- and the end pivot finger-arrangement (refer to figure 6.5.1).

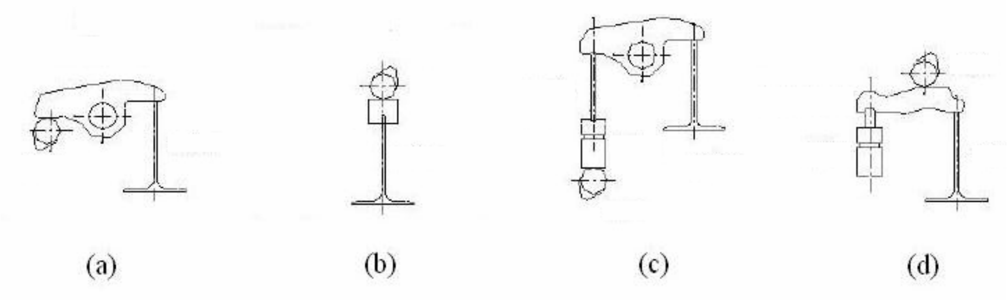

Figure 6.5.1: The (a) centre pivot finger -, (b) direct acting-, (c) pushrod- and (d) end pivot finger valve train arrangement.

This project involved the study of the end pivot finger valve train arrangement, also known as the 3D-finger follower valve train arrangement because of the three dimensional freedom of movement of the follower. Figure 6.5.2 illustrates the final assembly of the valve train components in ProEngineer.

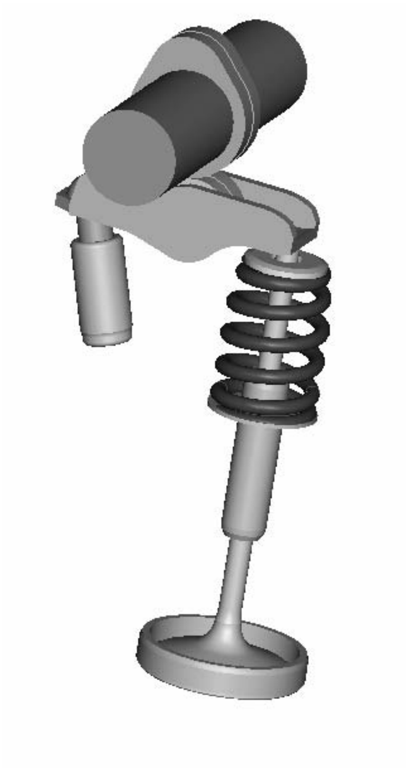

Figure 6.5.2: Valve train solid model assembly.

In this case the installed spring is only for graphical representation, since the actual solid model of the spring was modelled in its free length. The spring would be compressed to its installed length in the dynamic model. The non-moving valve train components (valve seat, valve guide and the HLA oil base) are positioned into the cylinder head at specifically machined locations.

The inlet valve is allowed to translate along and rotate around its axis of symmetry, thus having a $< TY, RY >$ freedom. The valve translation is constrained through contact with the valve seat and the spring exerting a force through the valve retainer and collets. The finger follower is in contact with the valve tip. Loss in contact is possible, i.e. in events of severe valve spring oscillations causing the valve tip and/or finger follower to deviate from their kinematic profiles. The valve is free to rotate and in practice is a necessity to prevent fuel and deposit build-up between the valve and valve seat. The valve experiences friction between:

1. the valve movement in the guide (translational),

2. the valve and valve seat contact (rotation),
3. the valve stem and the collets (rotation), and
4. movement between the finger follower and valve tip (translation).

The camshaft is only allowed to rotate around its axis of symmetry, thus having a $< RZ >$ freedom. The cam itself is in contact with the finger follower roller. Contact loss between the camshaft and roller is possible, similarly as in the case of the finger follower-valve tip contact. Besides the friction experienced between the cam and roller surfaces, the cam experiences friction at the hydrodynamic journal bearings in the cylinder head.

The collets are manufactured with grooves that fit into mating grooves on the valve stem. These grooves are case hardened seeing that it is the only transfer of valve spring forces to the finger follower and experiences high stresses. The collets have rotational freedom around its axis of symmetry, $< RY >$. The valve spring retainer and collets have matching wedge shaped profiles and are constantly wedged against each other through the valve spring force.

Although the HLA have been modelled as two separate solid models, it is physically one pre-assembled component that is simply slid into a machined position on the cylinder head. It must however be remembered that, dynamically they are two different parts. The HLA oil reservoir component is allowed to translate along and rotate around its axis of symmetry, thus having a $< TY, RY >$ freedom.

The HLA is discussed in more detail in section 5.1, but in short, it will translate and rotate infinitesimally during normal operation. The forces exerted on the HLA are from the rotating camshaft pressing the finger follower down. The HLA will compress slightly until the HLA reaction forces exceed the valve spring reaction forces, from which point onward the valve spring will experience the most deflection. The finger follower is positioned onto the spherical surface of the HLA oil reservoir. The mating surface of the finger follower is also spherical in shape and has the same radius. This joining between the HLA oil reservoir component and the finger follower forms a spherical contact joint. Similar contact loss between the finger follower and HLA is possible, as in the case of the finger follower-valve tip contact and the cam lobe-finger follower roller contact. Besides friction inside the HLA between the plunger and tappet (refer to section 5.1), friction is also experienced inside the spherical contact joint.

An innovative lubrication system exists in the physical valve train system. The HLA oil reservoir is connected to the normal oil system of the engine and therefore contains pressurised oil. The spherical end of the HLA has a 2 mm diameter hole machined into it. Pressurised oil flowing through this hole lubricates the spherical joint between the two components. In addition to this, the finger follower has a minute 0,3 mm diameter hole machined through the spherical shell. This allows oil to be sprayed directly onto the roller of the finger follower, thus lubricating the roller to minimise friction between roller and cam lobe.

Finally the finger follower is positioned, as discussed above, on the HLA and rests on the valve tip. Theoretically, the finger follower is not constrained. It is free to move in all 6 *degrees of freedom* (d.o.f.), even if only infinitesimally. Under normal valve train operation, contact from the HLA, cam lobe and valve tip defines the movement. The most prominent movement of the finger follower is rotation around its Z axis rotating at the HLA contact end (refer to figure 6.5.3 below). The spherical joint between the finger follower and HLA gives the finger follower the freedom to rotate around its Y- and X axis as well. The finger follower however has stops (not modelled on the solid model) at the valve's side to prevent rotation around the Y axis. The line of contact between the cam lobe and finger follower roller, as well as the line of contact between the finger follower and valve tip, prevents rotation around the its Y- and X axis.

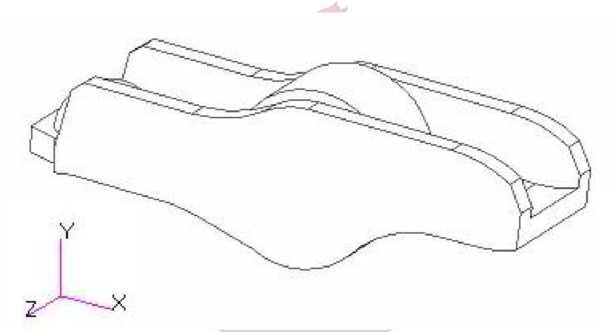

Figure 6.5.3: Finger follower solid model illustrating its local coordinate frame.

The most common failure mechanism of the 3D-finger follower valve train arrangement is the dislodging of the finger follower itself, i.e. when severe valve spring oscillations causes loss of some, or all of, the component contacts in such a manner that the finger follower "jumps" off its rests.

This concludes the discussion on the physical valve train system and its detail operation. The following section discusses the simplifications made on the mechanisms of the valve train system in order to minimise redundant degrees of freedom and build the dynamic model efficiently.

6.5.2 Valve train mechanism simplifications and implementation

In ADAMS, redundant degrees of freedom do not have any effect on the mechanical system, whether they are present or not. An example of one redundant constraint would be the rotation of the inlet valve around its own axis of symmetry. Physically, the intake valve moves inside the valve guide with a cylindrical joint. Translation up and down inside the valve guide is allowed, as well as rotation around the axis of symmetry. By replacing the cylindrical joint with a normal translational joint (no rotation around the axis of symmetry allowed), one system degree of freedom is removed, which removes one equation of motion from the mechanical system and increases computational efficiency. In the dynamic model of this project, the removal of redundant degrees of freedom such as the above exists at almost every component.

Another general simplification was the absence of friction in the dynamic model. As discussed in section 3.2, when the test rig measurement concept was abandoned, friction measurement became impossible. This simplification did not effect the results of the model drastically, if any. Good model-measurement correlation was found without the inclusion of friction as will be seen in chapter 7.

All the solid models of this study were imported into ADAMS as Parasolid files. (The spring and HLA being dynamic models and not falling under this criteria.) Each model was defined as a solid component with the correct model mass, centre point of gravity and moment of inertia value, as tabulated in table E.1. From here on, mechanisms and constraints were fitted to the components. By referring to the above valve train operation discussion, the following section will summarise the dynamic model and its simplifications:

All non-moving valve train components were constrained to ground with lock joints. No degrees of freedom and no relative movement between these parts and ground were allowed. These included the valve seat, valve guide and the HLA oil base, all of which were positioned into the cylinder head at clearly defined (machined) locations.

The inlet valve was constrained to the valve guide with a translational joint that only allowed translation along its axis of symmetry inside the valve guide. Contact between the inlet valve and inlet valve seat were also modelled with the help of ADAMS's point-to-plane contact.

The camshaft was constrained to ground with a revolution joint, or simply put, a hinge. Thus only allowing rotation around its axis of symmetry. A rotational motion was superimposed onto this joint and this was the motion generator of the dynamic model. The cam itself was constrained to the camshaft with a lock joint. Thus no relative movement between the cam and camshaft was allowed.

As has been mentioned earlier, the collets were ignored in the solid model and its mass was simply added to that of the spring retainer. The spring retainer was constrained to the valve tip with a lock joint.

The HLA have been modelled as two separate solid models. The HLA oil base part was constrained to ground with a lock joint. The HLA oil reservoir part was constrained to the HLA oil base part with a translational joint, only allowing it to translate up and down along its axis of symmetry. The HLA dynamic model was incorporated into ADAMS as a Single Component Force (SCF). This SCF acts between two user defined bodies. The direction vector is chosen to be the line of sight between the two bodies.

The value of the SCF is specified by a function, which in the case of the HLA model is an AKIMA spline fitted through displacement-force data points (refer to figure 5.4.1) found from the characterisation equation 5.4.1. In essence, the input to this function is the relative displacement between the HLA oil base and oil reservoir which results in an output force (the force expanding the HLA), taken from the spline values. Linear interpolation and extrapolation is used for values between data break points.

The finger follower is constrained to the spherical end of the HLA oil reservoir part by means of a revolute joint. In reality, contact loss is possible at this joint, but much less likely that contact loss between cam and roller, and follower and valve tip. Therefore contact loss in this joint will only be clear when analysing the joint force. When the joint force becomes zero, contact is lost.

The revolute joint prevents the finger follower from rotating around the HLA centre of symmetry, but allows it to rotate around its Z axis (refer to figure 6.5.3). As discussed in Chapter 3, an accelerometer and a small block of mild steel were added to the follower. The total additional mass added to the follower was 5,6 g and this was simply modelled onto the follower as a point mass and constrained to the follower with a lock joint at the correct location.

The finger follower roller is constrained to the finger follower by means of a revolution joint, allowing it only to rotate around its axis of symmetry.

In addition to the modeling of a non-linear spring, one of the objectives of this project was to account for contact loss between components. ADAMS's two-dimensional curve-to-curve contact was used between the cam and finger follower roller, as well as between the valve tip and finger follower.

As the name implies, two curves need to be specified for one curve-to-curve contact constraint. These curves were constructed from the geometry itself and defined as a matrix of points. Two closed curves for the cam and finger follower roller, and two open curves for the valve tip and finger follower were specified respectively.

In addition to specifying the curves, the type of normal force between two contacting bodies could be specified. Impact force-based contact was chosen instead of a restitution force-based contact. Figure 6.5.4 and equation 6.5.1 describe the $Impact$ function in detail.

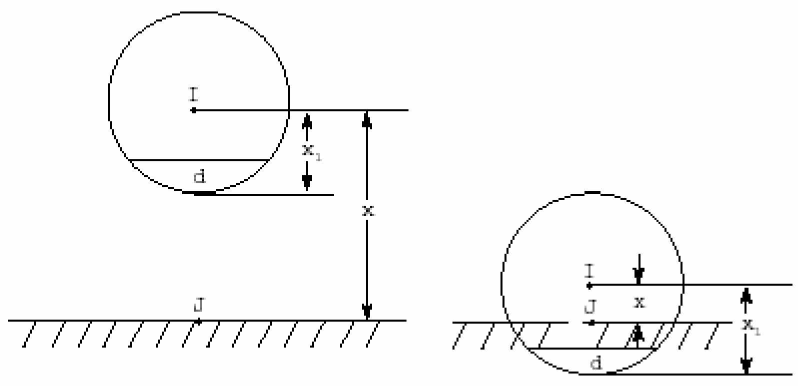

Figure 6.5.4: Impact force description.

$$Impact(x, \dot{x}, x_1, k, e, c_{max}, d) \tag{6.5.1}$$

where x = distance between the I and J marker;

$\dot{x}$ = time derivative of x;

x_1 = positive real variable that specifies the free length of x;

k = non-negative real variable specifying the stiffness between boundary surface interaction;

e = positive real variable that specifies the exponent of the force deformation characteristic;

c_{max} = non-negative real variable that specifies the maximum damping coefficient, and;

d = positive real variable that specifies the boundary penetration at which ADAMS/Solver applies full damping.

The stiffness, k, was defined as the material stiffness, calculated similarly to the closing stiffness of the gap elements used in the FEM model (refer to figure 6.4.7). No damping was specified for bodies in contact.

With the inclusion of contact, the dynamic model was complete except for the introduction of the dynamic spring model. The following section discussed this.

6.5.3 Dynamic spring model, pre-compression and pre-load

As was discussed in section 6.4.6, the equivalent spring model was to be copied into ADAMS by specifying one body for each of the 22 spring elements. (The valve guide was the ground body to which the first spring component was connected to.) These 22 spring elements were connected to each other through 22 linear springs, using the standard spring component found in ADAMS. In addition to the 22 linear spring elements, 22 SCF were also incorporated between all the spring bodies. Similarly to the SCF of the HLA model, each of these 22 SCF were defined by a function that was represented by a spline. The splines were defined by the non-linear force-deflection curves discussed in section 6.4.5.

Again, no damping was used in specifying the linear spring components. The reason for this, as is the reason for specifying no damping between bodies in contact, is that upon first comparison between the dynamic model and measured data, it became clear that no damping was prominent in the valve train system. Only by removing all system damping, a good correlation between test data and the dynamic model was found.

In reality, the only significant damping that exist between valve train components is the Coulomb damping caused by a layer of oil between the contact surfaces. (This damping leads to a definition of friction as well.) This Coulomb damping was assumed to be negligible small. In addition to this, metal to metal contact generally have insignificant damping. (Akiba *&* Kakiuchi (1988), Baniasad *&* Emes (1998) and Isaac Du *&* Chen (2000)) Thus, the necessity to remove all damping in the dynamic model, to ensure good comparison with measured data, was to be expected.

The FEM model of the spring was developed and analysed in its free length. The dynamic spring model had to be inserted into the valve train model pre-compressed to its working length. The installed length is known and the FEM model was merely compressed to that length in a static compression analysis. The reaction force (or pre-load force in this case), as well as the individual spring element displacements, were calculated. Each spring element of the ADAMS dynamic model was modelled at the pre-compressed length with the pre-load set to the pre-load calculated from NASTRAN. Spring stiffness values and force-deflection curves remained unchanged.

After the spring model was incorporated, the dynamic model assembly process was completed. The next step was the verification of the dynamic model and this is described in the next section.

6.5.4 Dynamic model summary

Table 6.5.1 summarises the mechanisms of the final dynamic model. Note that repetitions of mechanisms are omitted.

Table 6.5.1: Summary of dynamic valve train model mechanisms.

Component	Connected to	Mechanism
Inlet valve seat	Ground	Lock joint
Valve guide	Ground	Lock joint
	Inlet valve	Translational joint
HLA oil base	Ground	Lock joint
	HLA oil reservoir	Translational joint
HLA oil reservoir	Finger follower	Revolute joint
Cam	Finger follower roller	Curve to curve contact
Camshaft	Cam	Lock joint
	Ground	Revolute joint with rotational motion
Finger follower roller	Finger follower	Revolute joint
Inlet valve	Finger follower	Curve to curve contact
	Spring retainer	Lock joint
Spring body 1	Valve guide	Linear spring component
	Valve guide	Single component force
	Ground	Translational joint
	Spring body 2	Linear spring component
	Spring body 2	Single component force
Spring body 2 to 20	Spring body 3 to 21	Linear spring component
	Spring body 3 to 21	Single component force
	Ground	Translational joint
Spring body 22	Spring retainer	Linear spring component
	Spring retainer	Single component force
	Ground	Translational joint
Accelerometer and securing block	Finger follower	Lock joint

Using the ADAMS's model verification function, the dynamic model was verified successfully with the following output and summary:

1. 25 degrees of freedom,
2. 32 moving parts (not including ground),
3. 3 revolute joints,
4. 23 translational joints,

5. 6 lock joints,
6. 1 motion, and
7. no redundant constraint equations.

By successful verification of the dynamic model in ADAMS, the model was completed. Model input parameters such as engine speed, damping coefficients, oil aeration values, etc., could now be changed until good measured data verification was achieved. Dynamic model verification is discussed in the following chapter.

Chapter 7

Dynamic Model Verification

As discussed in chapter 3, the finger follower acceleration above the inlet valve tip, as well as the spring seating force, were measured experimentally on a running engine. ADAMS allows various measurements to be placed at various locations on the dynamic model. Thus, an acceleration measurement was located at the point of measurement on the physical engine. The spring seating force were also measured on the ADAMS model.

Measurement results from sections 3.3 and 3.4.3 could now be compared with the dynamic model results. This was one of the primary project objectives and was done to modify the dynamic model parameters until adequate model accuracy was reached. After an acceptable level of model verification was reached, the dynamic model was deemed representative of the physical valve train system and various analysis on the valve train could be conducted.

Various other measurements were added throughout the model such as valve displacement, -velocity, -acceleration, contact force between bodies in contact, HLA reaction force, HLA displacement, etc. However, these are not verification measurements, but rather analysis measures and will be discussed in chapter 8.

7.1 Dynamic model complexity

In developing the complete dynamic model as discussed in section 6.5.2, four steps were incorporated. Firstly, only one linear spring was used. Secondly, 22 linear spring elements replaced the single linear spring. Thirdly, the 22 non-linear force-deflection relations were superimposed onto the 22 linear spring elements, and finally, the HLA dynamic model was included (prior to this stage no relative motion between the HLA oil reservoir and oil base was allowed).

To motivate the above systematic increase in model complexity, the first verification step was to compare each development step with one another. An engine speed of 4000 rpm was chosen for this illustration. At 4000 rpm, interesting dynamic behaviour occurs, but not to the extent as in the case of 6000 rpm engine speed, where the objective of the illustration might be lost.

The simplest form of the model included a single linear spring. The total stiffness, K_{total} of this spring was calculated to be 28,8 N/mm from the following equation

$$\frac{1}{K_{total}} = \frac{1}{k_1} + ... + \frac{1}{k_i} + ... \frac{1}{k_n} \tag{7.1.1}$$

The dynamic profile of this model was very close to the kinematic result of the valve train simulation and not a good approximation of valve train dynamics if compared to the other dynamic models, illustrated in figure 7.1.1. Only the second cam event is plotted to ensure that good system equilibrium is reached. It is evident that the single linear spring does not account for internal spring oscillations and force superpositions.

However, the multi-spring linear model becomes unstable and is a bad representation of the actual dynamics. The reason for this is that the linear model does not restrict un-limited spring body displacement amplitudes. For the non-linear model, the force-deflection curves was added and these represents physical coil contact and therefore restricts un-limited spring body displacement.

The final model, compared in figure 7.1.2 with an actual measurement of the spring force at 4000 rpm, was based on the non-linear multi-spring model, but with the HLA dynamic model being added. In this case, the oil aeration value is set to 1% air and a slight oscillation throughout the spring seat force curve is present. This oscillation seems to have been damped slightly and correlates well with the measurement. This damping however is caused by the HLA only.

Now that the necessity for the model sophistication has been illustrated, the next step would be to compare measured acceleration and spring seat force data with the dynamic model data. In summary, the final dynamic model contained:

1. a multi-component non-linear spring model,
2. an HLA model with the capability to vary the oil aeration value,
3. the capability to include damping, both as internal damping of the spring elements and as damping between contacting bodies, and
4. no friction.

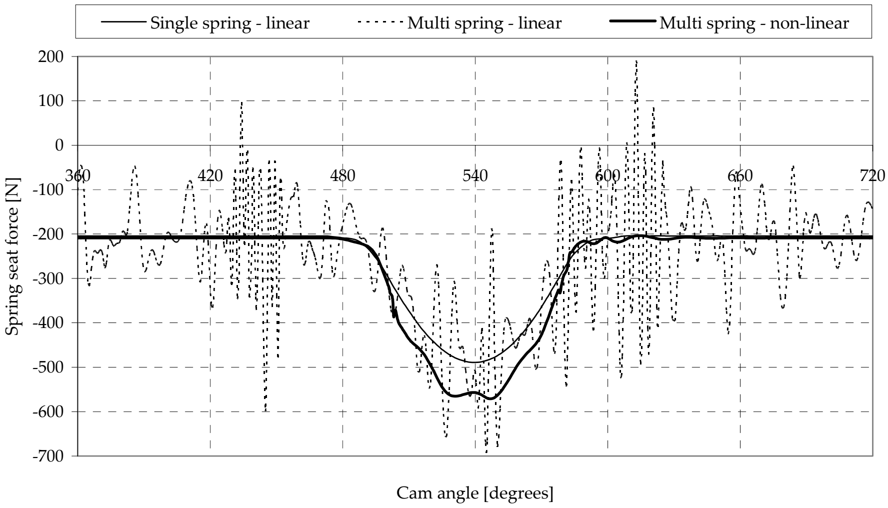

Figure 7.1.1: Modelled spring seat force comparison between the single linear spring model, the unstable multi spring linear model, and the multi spring non-linear model. 4000 rpm engine speed.

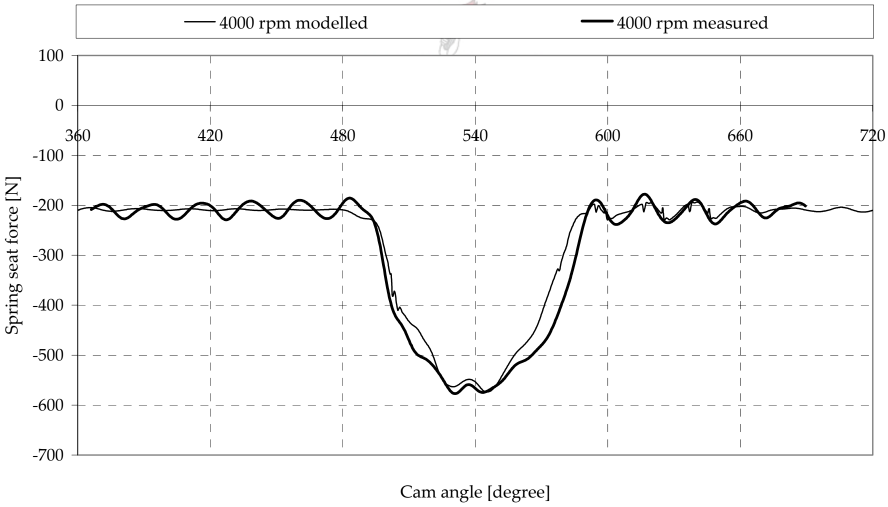

Figure 7.1.2: Spring seat force comparison between the multi spring non-linear model, including the HLA dynamic model with 1% oil aeration, and measured values. 4000 rpm engine speed.

7.2 Acceleration measurements comparison

At first only the FWT measured data was used to verify the dynamic models. The acceleration measurement data was only used as a general comparison. The reason for this was that the acceleration measurements were much more noisy than the FWT measurements and for this reason used with more reluctance than the relatively "clean" FWT measurement. However, the acceleration measurement were used eventually and the comparisons will be discussed first.

As discussed in section 3.3, data analysis methods such as the DFT and digital filtering were used to analyse the acceleration measurements. Figures 7.2.1 through to 7.2.3 illustrate the comparison between the acceleration measurements and the dynamic model.

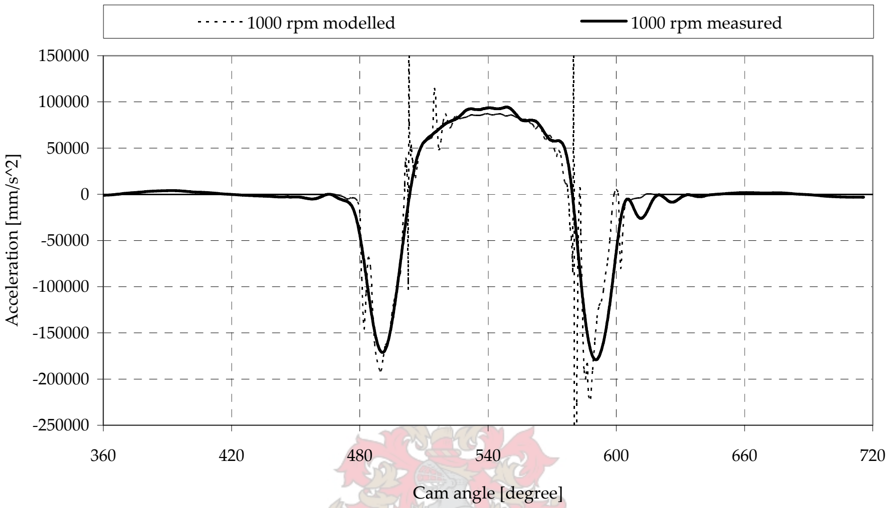

Figure 7.2.1: Modelled and measured follower tip acceleration at 1000 rpm engine speed. 1% oil aeration.

7.3 Force washer transducer measurements comparison

From the FWT measurements, it was clear that very little dynamic damping was present in the valve train. It was thus necessary to remove all damping from the dynamic model in order to ensure good correlation. Eventually, the only parameter used to change the models significantly was the oil aeration values of the HLA model. This proved to be convenient and efficient.

The oil aeration values were varied from 0.5% to 10% for each engine speed modelled. Figures 7.3.1 and 7.3.2 illustrate the difference between two identical models of which the oil aeration value was 2% and 0.5% respectively.

Both models correlate well at the end of spring compression, but the difference lies in the oscillation amplitude between cam events. With a smaller percentage of air in the

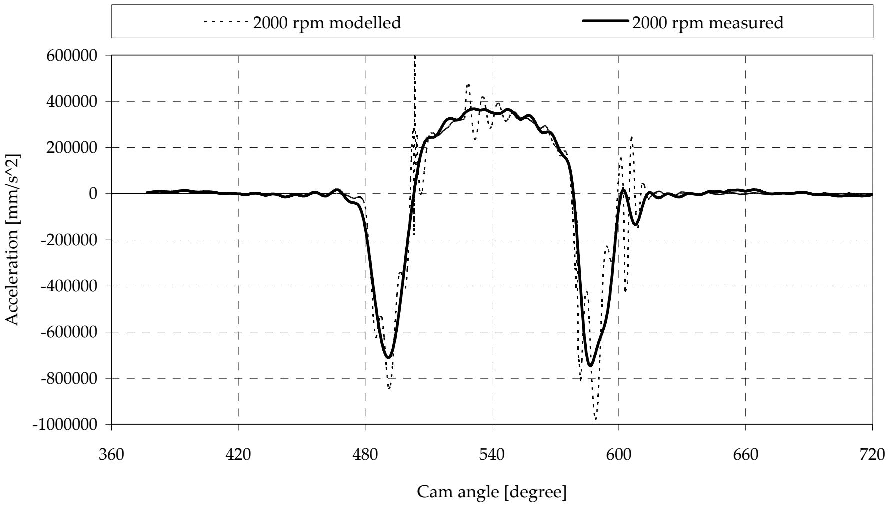

Figure 7.2.2: Modelled and measured follower tip acceleration at 2000 rpm engine speed. 1% oil aeration.

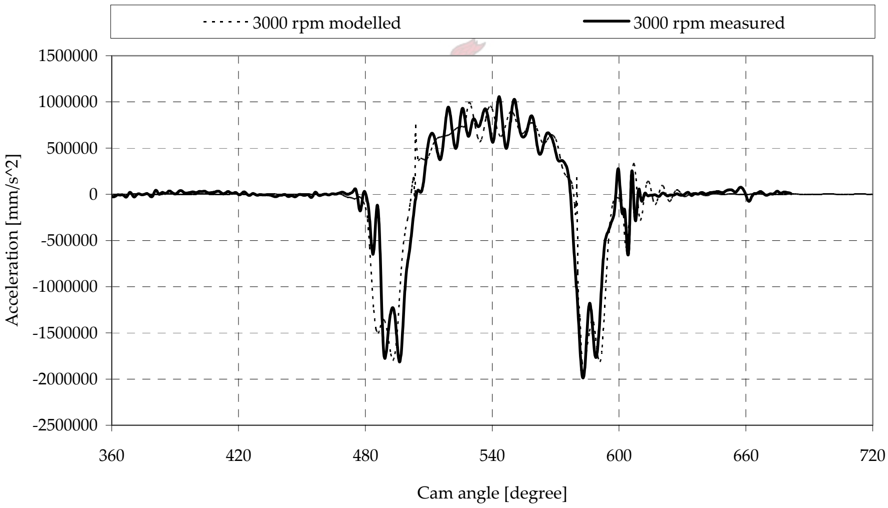

Figure 7.2.3: Modelled and measured follower tip acceleration at 3000 rpm engine speed. 1% oil aeration.

oil, the HLA becomes stiffer and less compressible. Oscillation frequency is proportional to stiffness and therefore increases with a decrease of oil aeration (equation 7.3.1).

$$\omega_{osc} \propto \frac{1}{air} \tag{7.3.1}$$

Oscillation amplitude is inversely proportional to stiffness and therefore decreases with

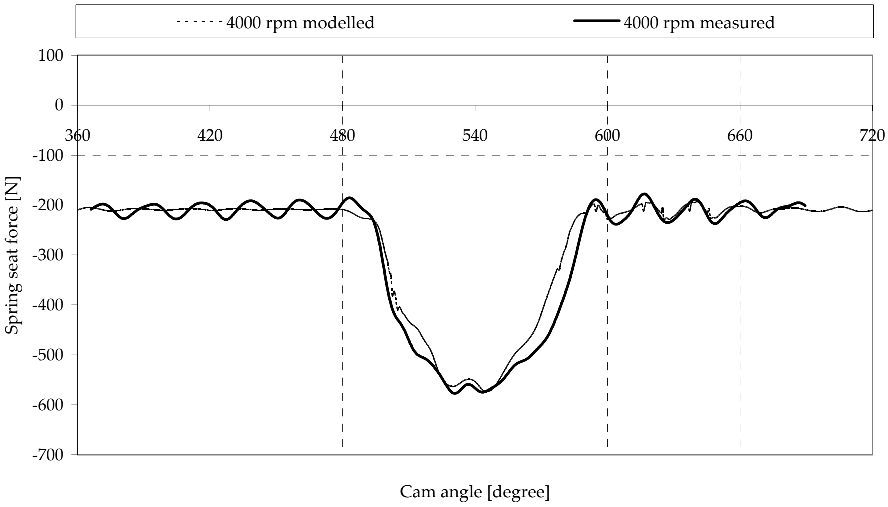

Figure 7.3.1: Modelled and measured spring seat force at 4000 rpm engine speed. 2% oil aeration.

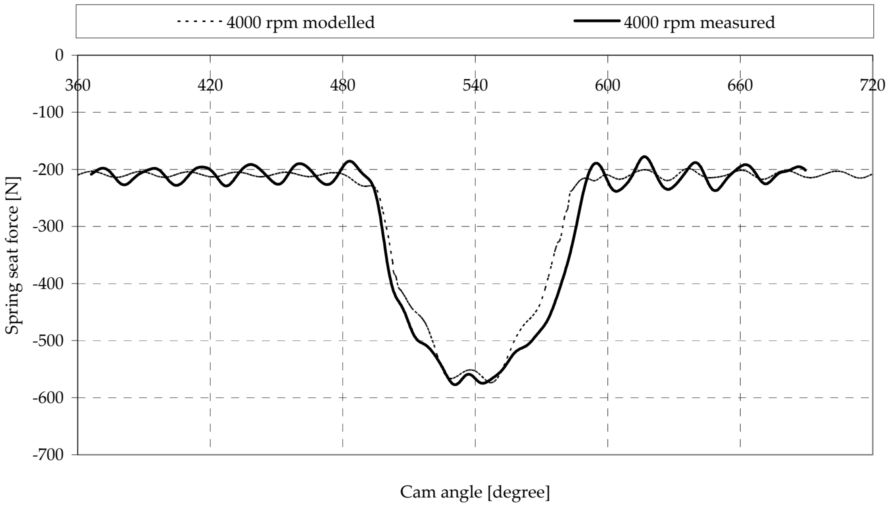

Figure 7.3.2: Modelled and measured spring seat force at 4000 rpm engine speed. 0.5% oil aeration.

a decrease in oil aeration. With 2% air, the force oscillations between the cam events correlated better.

At each engine speed a different oil aeration value was found. The reason for this is that the oil aeration value is a function of oil viscosity and oil temperature. The durability of the FWT was an uncertainty and the engine was not allowed to be heated up properly before measurement was started. Therefore for one, the oil temperature was increasing during measurement and this influenced the oil aeration. The measurement taken at 1000 rpm was the first measurement to be recorded. The engine oil was still cold and relatively de-aerated and therefore a low value of oil aeration could be expected.

Eventually all measured engine speeds were modelled and model parameters adjusted until good correlation was found. At some engine speeds, the correlation fitted better than others. Figures 7.3.3 through to 7.3.6 illustrate the comparison between measurements of the FWT with that of the modelled results at engines speeds of 1000 rpm, 3000 rpm, 5000 rpm and 6000 rpm.

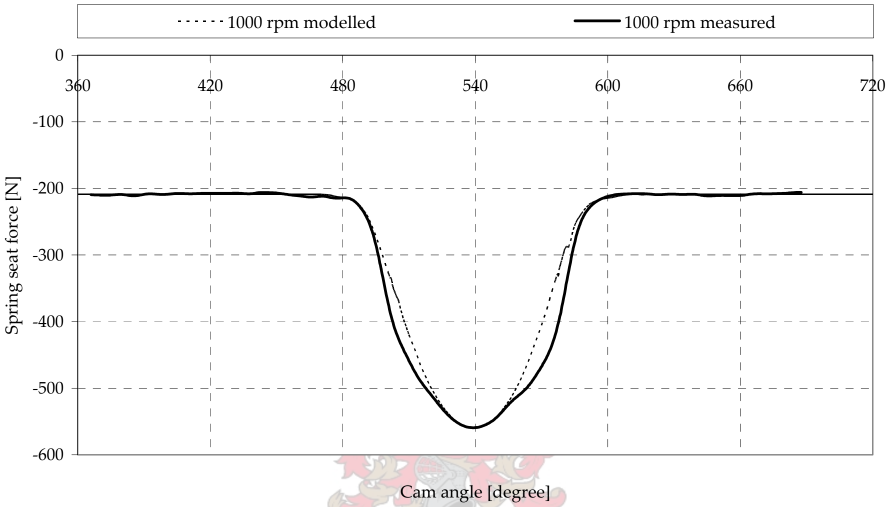

Figure 7.3.3: Modelled and measured spring seat force at 1000 rpm engine speed. Model contains 1% aerated oil.

At 1000 rpm, figure 7.3.3, very little kinematic deviation was observed. The forces during the spring compression and expansion phase did not correlate too well. This could be caused by small differences in spring stiffness between the model and the actual spring. However, the force amplitudes correlate well. As mentioned before, the aeration value at this speed was the lowest and this is believed to be caused by the fact that it was measured with cold oil as soon as the engine was started. In other words, it is hypothesised that the oil was well de-aerated.

2000 rpm was not measured due to the FWT failing before it could be measured.

At 3000 rpm, figure 7.3.4, kinematic deviation is present. Although the forces during the spring compression and expansion phase correlate to an even lesser extent than that of at 1000 rpm, the oscillation amplitudes correlate well. In some instances the oscillation frequencies also tie up. Oil aeration value has increased to 2 percent due to the oil being heated, less viscous and more aerated.

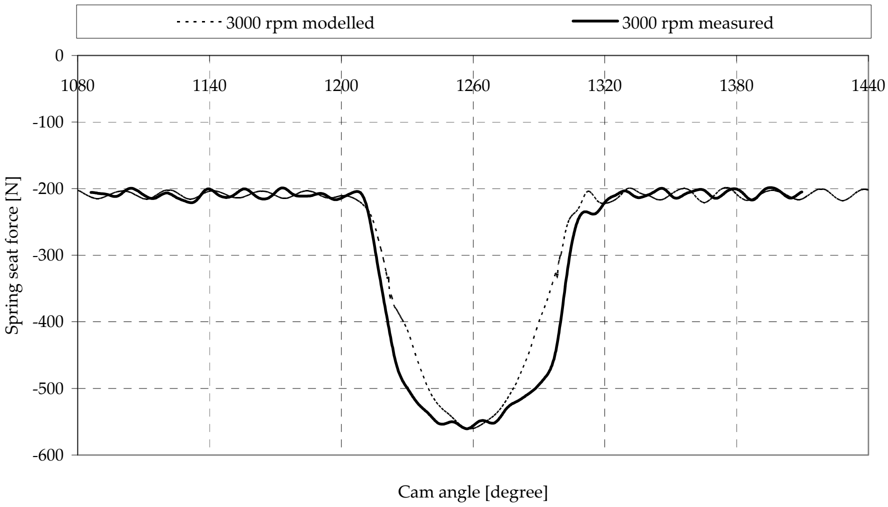

Figure 7.3.4: Modelled and measured spring seat force at 3000 rpm engine speed. Model contains 2% aerated oil.

At 4000 rpm, figure 7.3.1, the two curves correlate well. The oscillation during the maximum cam lift is captured as well, in frequency and in amplitudes. This dynamic deviation is typically the illustration of spring surge and well defined at this engine speed. Even the oscillations after the cam event correlate well, again in frequency and in amplitude. It also seems as if the slight damping of the oscillations after the cam event is captured in the model.

Unfortunately, the oscillations before the cam event are not well predicted by the model. This might be caused by the fact that the initial conditions had not yet reached a state of equilibrium by the time of the second cam event. By investigating this, it was clear that this was not the case. Roughly in the middle between two cam events it was found that all oscillations ceased suddenly. This could be caused by ADAMS calculation algorithm and choice of step sizes as this phenomena was highly sensitive to step size chosen. This was however the best compromise that could be found and the result was left as reported.

At 5000 rpm, figure 7.3.5, valve dynamics deviated substantially from the kinematic profiles and spring forces oscillated with large amplitudes. Unfortunately, at this engine speed, the oscillation frequencies did not correlate well. Again, slight differences in natural frequencies could result in these differences between the measured and modeled results. Oil aeration values of five percent were required for good dynamic prediction indicating that at this speed, the oil was well aerated.

At 6000 rpm, figure 7.3.6, correlation between measured and modelled values corre-

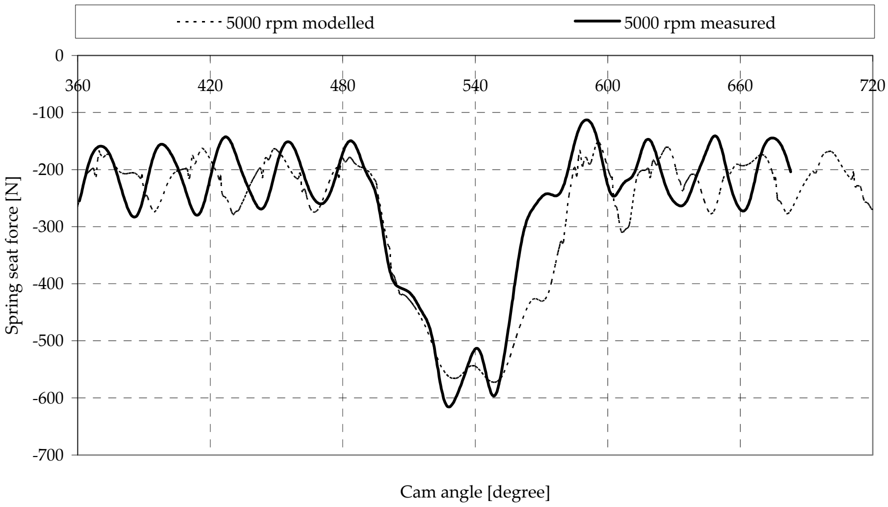

Figure 7.3.5: Modelled and measured spring seat force at 5000 rpm engine speed. Model contains 5% aerated oil.

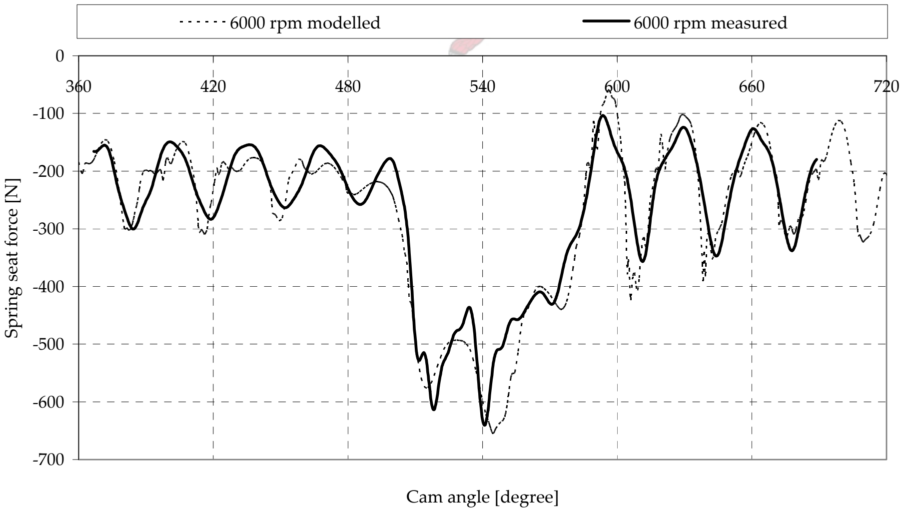

Figure 7.3.6: Modelled and measured spring seat force at 6000 rpm engine speed. Model contains 5% aerated oil.

late exceptionally well. By realising the speed of measurements and the of forces being measured over microns of displacements, this result at 6000 rpm is better than expected. Oscillation frequency, -amplitude and -damping correlate nearly perfectly.

With dynamics being more critical at higher engine speeds, the improved correlation at higher speeds make the dynamic model extremely valuable for analysing valve train dynamics.

Chapter 8

Case Study: Cam Profile Modification Analysis

The dynamic model had been verified successfully through actual measurement of spring seat forces and valve- or cam follower tip accelerations. As a demonstration of the model's capabilities and to illustrate how it can fulfil the need for which this project was initiated, a case study is discussed in this chapter.

8.1 Case study objectives

During a product development project at the engineering company sponsoring this project, certain engine modifications were done on a production engine. The objective was to increase the engine performance dramatically. The primary modification was the improvement of the engine breathing by increasing the inlet valve opening duration and opening lift.

Due to a lack of suitable models and time the cam profile modification was done graphically. The proposed development strategy was to manufacture a prototype and then proceed with an engine test to measure the engine performance increase.

Modifying engine breathing characteristics usually results in a gain and loss process. For example, if you gain torque in low engine speeds, you lose torque at high engine speeds and vice versa. Five iterations were necessary before the desired performance increase was achieved. The final prototype, aptly referred to as Proto5, achieved the desired performance characteristic with regards to engine power and torque curves and also engine driveability.

The effect that the cam profile modification had on the valve train dynamics could also not be analysed thoroughly and this is where the need for this project arose. In hindsight now, the verified dynamic model would be applied in the analysis of the valve train dynamics of the Proto5 cam profile. The standard camshaft profile is used as a benchmark throughout the analysis.

8.2 Cam profile modification

One spatial constraint of the new cam profile design was that it had to fit inside the standard camshaft profile. No billets of this camshaft were available in the short amount of time allocated for this development. As figure 8.2.1 illustrates, the basic principle was to grind the standard cam lobe down to a smaller base circle and keep the standard maximum lift point identical to the standard profile, thus effectively increasing the lift of the cam profile.

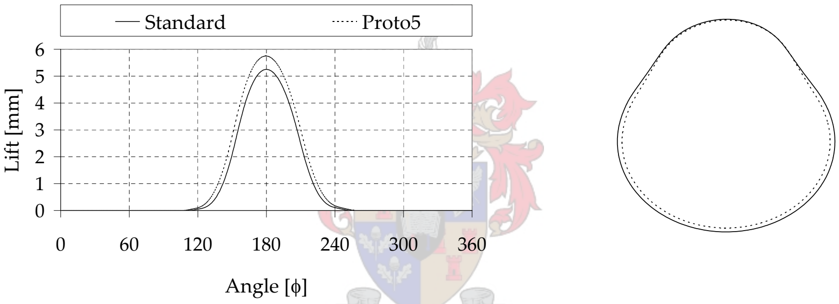

(a) Cam lift (b) Cam profile

Figure 8.2.1: Cam lift and cam profile comparison.

The end result was that the base circle radius was decreased form 15 mm to 14,35 mm and the maximum lift was increased by 0,5 mm, which related into a 9,5 % increase. By numerically integrating the area under the cam lift curve using the $\frac{1}{3}$ Simpson's rule and knowing the valve dimensions, an indication of the area flow rate of the intake port could be calculated. The difference in the area under the two lift curves were 17,7 %. Theoretically speaking, if the Proto5 cam profile would operate under an identical volumetric efficiency as the standard cam profile, the engine would breath 17,7 % more air-fuel mixture which could directly result in an engine performance increase of the same amount.

A Taylor series expansion was used to numerically differentiate the cam lift curves in order to calculate the kinematic cam velocity and cam acceleration curves. From figure 8.2.2 it is clear that both the kinematic velocity and acceleration peaks increased slightly. The next step was to incorporate the Proto5 camshaft profile into the dynamic model.

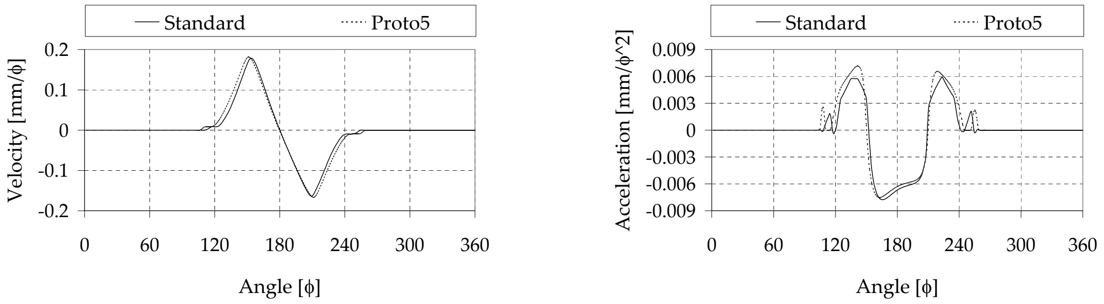

(a) Cam profile velocity

(b) Cam profile acceleration

Figure 8.2.2: Kinematic cam profile velocity and acceleration comparison.

Another useful criteria that could assist in the comparison of the two cam profiles would be the calculation of the harmonic contents of the profiles. Norton (1998) used the detailed spectral information of the camshaft as the input function of a *Frequency Response Function* (FRF) in his study of the vibrational characteristics of valve trains. The spectral information of the camshaft profiles could give us an idea of how the two different camshaft will excite the valve train system.

To calculate the spectral information of the camshaft profiles, the lift curves were represented by a Fourier series (Appendix section A.1.1 discusses the Fourier series theory in detail). The Fourier series coefficients were expressed in polar coordinates and plotted in figure 8.2.3. (In both cases the DC component, coefficient a_0 of equation A.1, was omitted.) This calculation was done with a MATLAB program written for this project.

All the lower order harmonics of the Proto5 profile had considerably larger amplitudes than those of the standard cam profile. However, from the 5th order harmonic and above, the amplitudes were slightly smaller than that of the standard cam profile which means that less probability exists for spring and valve train frequency resonance. Thus the vibrational content of the Proto5 camshaft valve train system is expected to be less than the standard system.

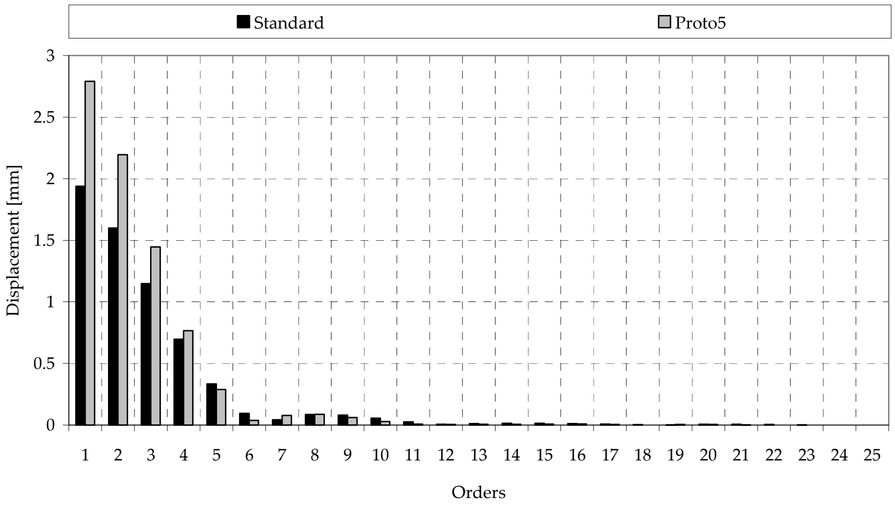

Figure 8.2.3: Cam profile harmonic content comparison.

8.3 Dynamic model modification

As was stated earlier, the radius of the base circle of the Proto5 camshaft was decreased by 0,65 mm. By referring to the finger follower valve train arrangement, this meant that the finger follower would shift up in order to ensure contact between the roller and the cam lobe, effectively rotating around the valve tip and opening a gap between itself and the HLA.

To calculate the length the HLA had to elongate in order to take up this valve train slack, the dynamic model was first simply allowed to reach static equilibrium. With the smaller camshaft inserted into the model, the modelled oil pressure in the HLA was allowed to expand the HLA until the valve train model slack was removed and all force were statically balanced again. The amount the HLA elongated was precisely 0,3 mm.

However, neither the model nor the actual engine, were ran in this configuration. Allowing the HLA to expand to that length would cause it to operate outside it's allowable operating length. A small spacer disc 0,3 mm thick was inserted between the HLA and the cylinder head, thus lifting the whole HLA. This meant that the HLA still operated under identical conditions to that of the standard engine arrangement.

8.4 Dynamic model comparison measures

Now that the two dynamic models had been set-up, many different aspects could be investigated. However, some are more interesting than others and these will be discussed here. Most of the parameters discussed in this section were analysed from 1000 rpm to 6000 rpm at intervals of 1000 rpm.

The obvious parameters to look at are the valve lift, valve velocity and valve acceleration curves. Additionally, the possibility to analyse valve train forces also exists. By increasing engine performance, it is reasonable to assume that the engine will be under more strain. In the specific application of Proto5, higher accelerations could lead to increased acceleration forces, which in turn could lead to contact loss. In the case of valve train dynamics, contact loss between valve train components could result in severe engine wear and reliability problems.

Even though contact loss may not be present, the safety margin (the difference between minimum spring force and maximum acceleration force) could be compromised. For this, the contact force at the HLA, the contact force between the cam and follower roller, and the contact force between the valve tip and follower tip were measured.

Another area of concern would be the fact the the spring is compressed 9,5 % more. This leads to an increase in spring material stresses, in the form of shear stresses, that would shorten the spring's operating life. Unfortunately this could not be investigated by the dynamic model directly. However, higher accelerations and increased spring compression could lead to a higher percentage of spring coil contact. This would lead to more internal damping and could actually improve valve train vibrations and operating life of other components.

As a starting point, the valve lift curves were analysed. Dynamic problems were found to occur at 6000 rpm and the dynamic model was used to analyse and find explanations for these problems. Figure 8.4.1 illustrates the difference between the standard and Proto5 valve displacement curves. It was found that the Proto5 camshaft profile had excessive valve movement after the valve should have been seated, while the standard cam profile behaved correctly.

This is referred to as "valve bounce" and is usually caused by excessive valve seating velocity, or valve closing velocity, where the impact velocity of the valve exceeds a threshold value. By studying the valve velocity curves, figure 8.4.2, it was found that the valve seat impact velocity of Proto5 was approximately -300 mm/s and the standard cam profile was -57 mm/s.

Although this value was almost six times more, it was also noticed that the velocities were negative, meaning the valve was moving away from the valve seat at that time. Furthermore, it was noticed that the valve increased its speed slightly before it slowed down again and changed direction before it came in contact with the valve seat. This indicated that some oscillation in valve train dynamics caused the subsequent valve

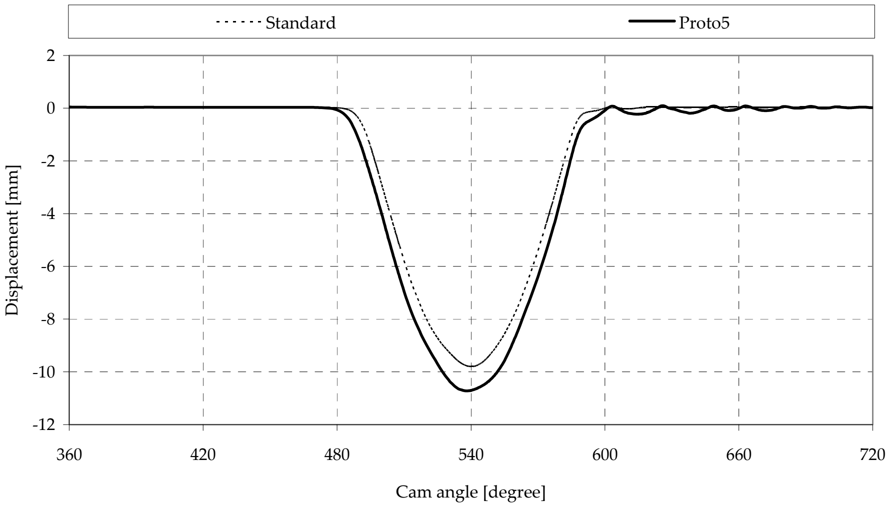

Figure 8.4.1: Valve displacement comparison at 6000 rpm engine speed. Valve bounce is present with the Proto5 camshaft profile.

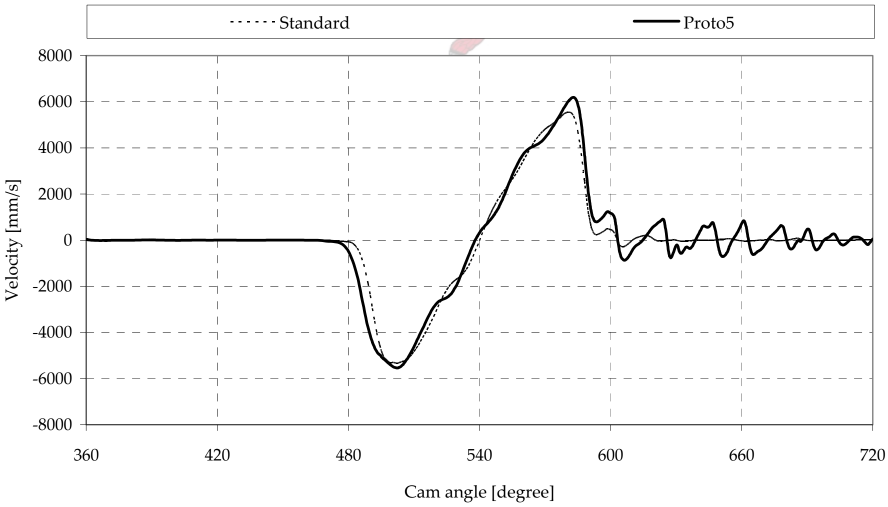

Figure 8.4.2: Valve velocity comparison at 6000 rpm engine speed. Valve bounce is present with the Proto5 camshaft profile.

bounce and not high valve impact velocity.

Upon further analysis it was found that the first parameter that drastically deviated from the standard cam profile's dynamic behaviour was the contact force between the cam and follower roller (figure 8.4.3).

At approximately 588 degrees cam angle the contact force spiked to a value of almost three times more than that of the standard cam profile. What followed was contact loss

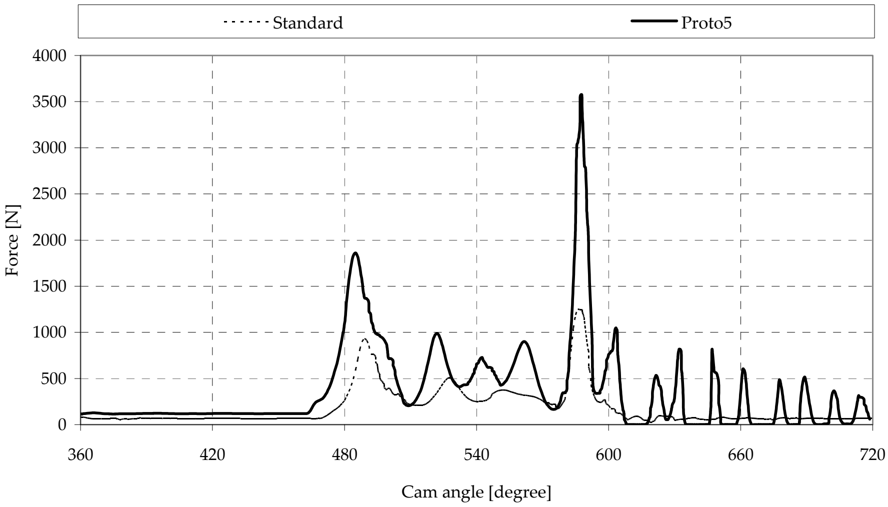

Figure 8.4.3: Contact force between cam and follower roller at 6000 rpm engine speed.

between the cam and roller (contact force becomes zero) at the exact timing of valve seating. The contact loss caused valve train back lash and jerking which caused the oscillations and eventually valve bouncing. In this case, the valve train dynamics of Proto5 are predicted to fail at 6000 rpm with the Proto5 cam profile.

The question was what caused this sudden spike in contact force. The first step was to look at the forces at other locations in the valve train. Firstly, the contact force between valve tip and follower tip did not deviate much from the standard cam profile at 588 degrees cam angle. The same appeared to be the case for the contact force measured at the HLA (Figure 8.4.4).

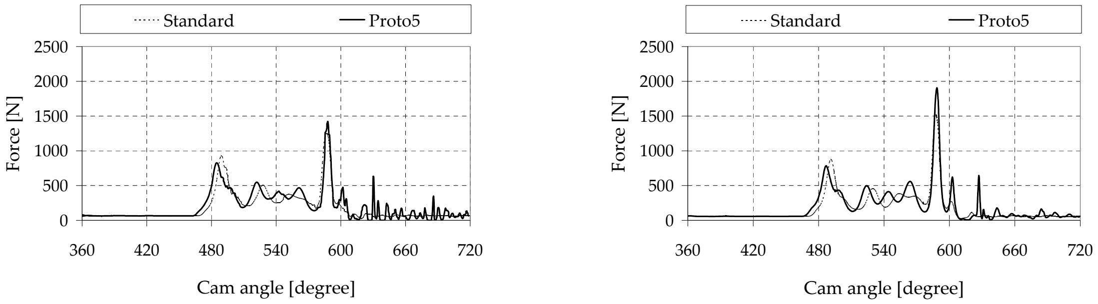

(a) Valve tip contact force

(b) HLA force

Figure 8.4.4: Valve tip to follower tip and HLA contact forces at 6000 rpm engine speed.

However, when referring to the valve acceleration at 588 degrees cam angle the valve acceleration were 22 % higher than the standard cam profile, as illustrated in figure 8.4.5. This increased the acceleration forces and by superimposing them onto the slightly increased contact forces at the valve tip and HLA, caused a large increase in reaction contact force between the cam and follower roller.

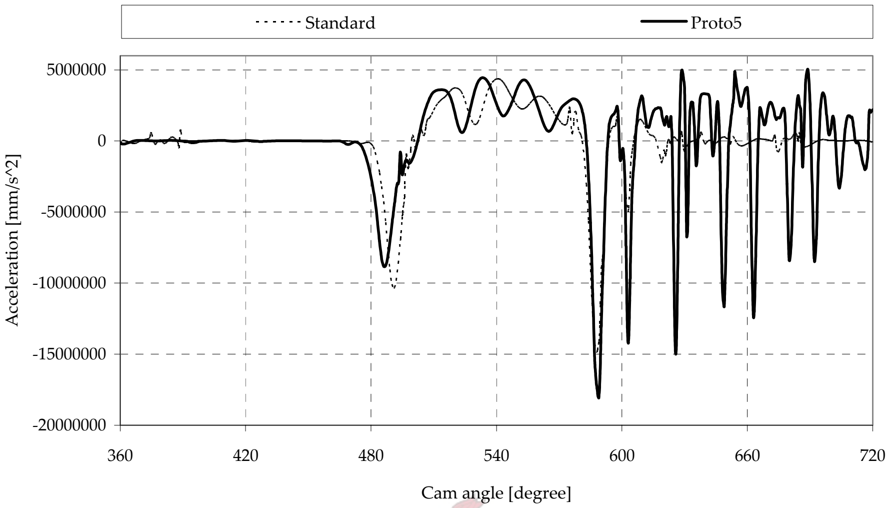

Figure 8.4.5: Valve acceleration at 6000 rpm engine speed.

Upon further study of the acceleration curve, it was noticed that during peak cam lift, between 500 and 590 degrees cam angle, a completely different dynamics oscillation, compared to that of the standard camshaft, existed. (This oscillation was also noticed in the valve velocity curve of figure 8.4.1.)

The oscillation frequency appeared to be slightly higher than that of the standard cam profile. The last oscillation in the acceleration curve in the above cam angle range reached a peak value at the time that the standard cam profile acceleration decreased dramatically. This point, at approximately 588 degrees cam angle, coincided with the drastic increase in the contact force between the cam profile and follower roller.

This difference in oscillation dynamics was present in all engine speeds. The reason for this could be that the Proto5 cam profile contains different cam harmonics than that of the standard cam profile. Figure 8.2.3 shows that the Proto5 cam profile has larger high frequencies amplitudes than the standard cam profile. Therefore the input function to the dynamic system contained a different frequency content and therefore a response of a different frequency could be expected.

It is believed however that the difference in oscillating frequency is caused by the difference in spring length under compression. The Proto5 cam profile compresses the spring 9,5 % more. When referring to the simple oscillating frequency formula for springs, equation 6.2.24, the oscillation frequency of springs is proportional to the spring's stiffness. The instantaneous stiffness of a non-linear valve springs change with spring compression and this could lead to a difference in dynamics oscillation during compression.

Although it is present at all engine speeds, at 6000 rpm the acceleration forces exceed the valve train system contact limit, i.e. the superimposing of all the contact forces and acceleration forces exceed the spring force and the valve train system loses contact.

As a summary of the dynamic differences between the standard cam shaft profile and that of Proto5 the maximum and minimum cam contact forces versus engine speed was analysed , figure 8.4.6 (with a resolution of 500 rpm).

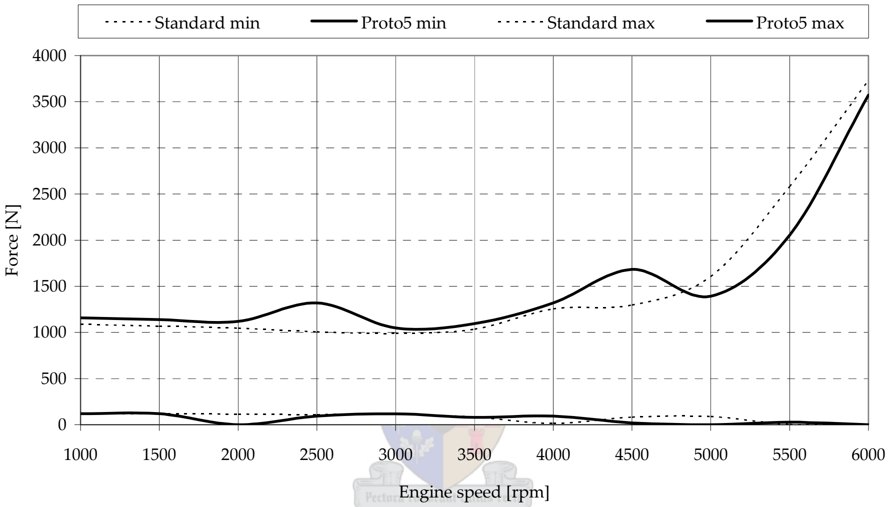

Figure 8.4.6: Comparison of maximum and minimum cam contact forces between the standard and Proto5 camshaft.

A surprise discovery was made at 2000 rpm. The new camshaft is predicted to lose contact at this engine speed. It also loses contact at 5000 rpm and 5500 rpm. Two large "humps" exist in the maximum contact force curve of Proto5 at 2500 rpm and 4500 rpm. The standard camshaft profile never loses contact, although it has a very low contact force at 4000 rpm of 12 N. Another interesting observation was that during the high speed contact loss region of the Proto5 cam profile, the maximum cam contact forces were less than that of the standard cam profile.

8.5 Cam modification actual results

The previous section illustrates that the difference in valve train dynamics caused by the change in camshaft profiles. In essence, the model illustrated some severe problems in the high engine speed region with Proto5. Mechanically the closure of the valve at 6000 rpm was delayed by only a few cam degrees and this would not have caused a drastic effect on engine power output.

The actual engine did perform well. With exhaust system optimisation, as well as the optimisation of the timing between the inlet and exhaust cam lobe, an engine power increase of approximately 20 % was achieved. This meant that together with the increase of engine breathing through the cam profile modification, the engine's volumetric efficiency was also increased. The original objective of increasing engine performance was thus reached.

However, dynamically, the Proto5 valve train system would have been problematic. These problems would have had a drastic effect on the reliability of the engine and more specifically the integrity of the valve train. The common modes of failure of the finger follower valve train arrangement are dislodging of the floating finger follower and failure of the HLA. Both problems are caused by excessive valve train vibrations caused by contact loss between valve train components. Unfortunately the Proto5 camshaft never ran endurance tests and the prediction of reliability problems was never confirmed.

Chapter 9

Conclusion

The primary objective of this project was to model and verify through experiments, the dynamics of valve trains. The objectives were achieved when good correlation was reached between actual measurements and the dynamic model.

The measurements were done on an actual running engine with minimal influence being caused by the measurement equipment. The moving mass of the accelerometer was kept minimal and the integration of the specially developed FWT was seamless with respect to the effect it had on the valve train components.

Measurements were sampled at maximum hardware frequency which ensured that all important dynamics were indeed captured. Data processing was simple and straightforward and digital filters could be adjusted afterwards to measure their influence on the processed data with respect to the raw data. Thus, it was ensured that no information was lost with data capture or analysis.

Various mathematical models were investigated and broad insight into spring dynamics was acquired through these studies. A sophisticated model of the HLA was also studied which resulted in a simplified and accurate model being implemented in the dynamic model of this project.

Much effort was placed on the accurate modeling of all valve train components which contributed to the accuracy of the modelled dynamics. A detailed, well thought through FEM model of the spring was constructed and resulted in very realistic results. The model development was systematically checked with actual measurements, calculations and comparisons between different models themselves, of which the successful comparison between the detailed model and the equivalent model is an example.

The basic technique used in modeling the final spring model was the well known modal analysis of discrete spring masses and additionally superimposing non-linear forces between the masses representing the non-linear behaviour of high speed valve springs. The number of modes used exceeded the number of Craig-Bampton modes specified for capturing all the dynamic effects of valve springs.

Through the verification process real engine mechanisms, such as oil aeration and the effect that oil temperature could have on valve train dynamics, could be identified and explained. The model includes sensitivity to damping and contact between valve train components. The model also allows and identifies valve train dynamic failures due to contact loss between the components.

By employing the dynamic model in a case study, it was discovered that the new design of a camshaft profile could have had dynamic failures at maximum engine speeds. These problems were not identified without the dynamic model.

Some interesting discoveries that were made during this study included the confirmation that the HLA had a major influence on the valve train dynamics and could not be ignored in this analysis. It became clear that the dynamics of the valve train deviate considerably from its kinematic characterisations. Especially at high engine speeds, spring force oscillations dominate the dynamics of valve train systems.

The primary contribution made by this project is the realisation of the importance of including non-linear valve spring dynamics in valve train dynamic analysis. Together with this an accurate dynamic model is now available for valve train dynamic analysis. The model's primary advantage is that different cam profile designs can be easily and time efficiently compared with each other. This could lead to identification of problem areas as well as identifying areas with room for valve train performance increases.

Now that the valve train model for a single cylinder has been completed, the remaining engine could be modeled step wise. Examples of these could be to first include the remaining cylinder's valve train components of which the modeling of the camshaft's dynamics would be the main objective. Afterwards piston dynamics, crankshaft dynamics and cam belt- or cam chain dynamics, could follow. By adding fluid dynamics of inlet and exhaust manifolds, and thermodynamics of combustion, the complete engine could be modeled eventually. The inclusion of mechanical friction into these models could also be an study area on its own.

In conclusion, the objective of the project was reached and some interesting discoveries were made. Valve train dynamics measurement techniques and equipment were developed and used successfully in a running engine. An accurate FEM model, containing all spring dynamics, were constructed and a technique illustrated to simplify the model without losing important dynamic characteristics. The project resulted in a verified, adjustable model of valve train dynamics.

List of References

Akiba, K. and Kakiuchi, T. (1988). A dynamic study of engine valving mechanisms: Determination of the impulse force acting on the valve. *Society of Automotive Engineering (SAE)*, vol. 03, no. 880389, pp. 6.659–6.664. (Cited on page 88.)

Bakonyi, S. (1968). The advantages of overhead camshafts-what are they? *Society of Automotive Engineering (SAE)*, vol. 03, no. 680028. (Cited on page 8.)

Baniasad, S. and Emes, M. (1998). Design and development of method of valve train friction measurement. *Society of Automotive Engineering (SAE)*, vol. 03, no. 980572, pp. 864–879. (Cited on page 88.)

Baruth, H. (1999). *Analytical Dynamics*, pp. 87–90. McGraw-Hill, Singapore. (For information.)

Baxter, M. and Rochester, N. (1948 July). Curvature-acceleration relations for planar cams. *American Society of Mechanical Engineers (ASME)*, pp. 483–489. (For information.)

Boctor, S.A, e.a. (1997). *Electrical Concepts and Applications*, p. 68. West Publishing Company, USA. (Cited on page 126.)

Callister, W. (1996). *Material Science and Engineering, An Introduction*. 4th edn. John Wiley and sons, Inc., USA. (Cited on page 21.)

Charfield, C. (1996). *The Analysis of Time Series*, p. 105. Fith edn. Chapman and Hall, Great Britain. (For information.)

Cook, R. (1995). *Finite Element Modelling for Stress Analysis*, pp. 41–50. John Wiley and Sons, Inc., USA. (Cited on page 65.)

Craig, R. and Bampton, M. (1968 July). Coupling of substructures for dynamic analysis. *AIAA Journal*, vol. 6, no. 7, pp. 1313–1319. (Cited on page 75.)

Fan, C. (1982). *Mechanics and Design of Cam Mechanisms*, pp. 11–14. Pergamon Press, New York. (For information.)

Gerald, C. and Wheatley, P. (1994). *Applied Numerical Analysis*, pp. 338–723. Fith edn. Addison-Wesley, USA. (For information.)

Giorelli, M. (2002 March). *Methodology for Correlating Experimental and Finite Element Modal Analysis on Valvetrains*. Master's thesis, Worcester Polytechnic Institude. (Cited on pages 57 and 72.)

Hamilton, M., e.a. (1987). *Mechanisms and Dynamics of Machinery*. 4th edn. Wiley, Canada. (For information.)

Isaac Du, H. and Chen, J. (2000). Dynamic analysis of a 3d finger follower valve train system coupled with flexible camshafts. *Society of Automotive Engineering (SAE)*, vol. 03, no. 2000-01-0909, pp. 854–861. (Cited on pages 75 and 88.)

Jensen, P. (1965). *Cam Design and Manufacture*, pp. 141–157. The Industrial Press, New York. (For information.)

Koster, M. (1974). *Vibrations of Cam Mechanisms*, pp. 2–5. The Macmillan Press Ltd, Great Britain. (For information.)

Kreuter, P. and Maas, G. (1987). Influence of hydraulic valve lash adjusters on the dynamic behaviour of valve trains. *Society of Automotive Engineering (SAE)*, vol. 03, no. 870086, pp. 4.1–4.9. (Cited on pages 8, 49, and 50.)

Lewandowski, D. (1998). *Experimental and Modelled Effects of Camshaft Manufacturing Errors on the Dynamics of High Speed Valve Trains*. Ph.D. thesis, Department of Mechanical and Aerospace Engineering, North Caroline State University, Raleigh, North Caroline. (For information.)

Norton, R.L., e.a. (1998). Analyzing vibrations in an ic engine valve train. *Society of Automotive Engineering (SAE)*, vol. 03, no. 980570, pp. 856–863. (Cited on page 102.)

Norton, R. (2002). *Cam Design and Manufacturing Handbook*, pp. 162, 399. Industrial Press, Inc., New York. (For information.)

Ortmann, C. and Skovbjerg, H. (2000 November). Part 1: Valve spring. In: *International ADAMS Users Conference*. Mechanical Dynamics, Inc., Rome. (For information.)

Porot, P. and Trapy, J. (1993). A numerical and experimental study of the effect of aeration on valve trains equipped with hydraulic lash adjusters. *Society of Automotive Engineering (SAE)*, vol. 03, no. 930997, pp. 732–744. (Cited on page 41.)

Roberts, J. (1967). *Spring Design and Calculations*. Herbert Terry and Sons Ltd, England. (For information.)

Roskilly, M., e.a. (1986). Valve gear design analysis. *Society of Automotive Engineering (SAE)*, vol. 03, no. 865027. (Cited on page 8.)

Ryti, M. (1974). Calculating procedure for cams. *The Motor Industry Research Association*. (For information.)

Schamel, A. R., e.a. (1989). An efficient model for valve train and spring dynamics. *Society of Automotive Engineering (SAE)*, vol. 03, no. 890619, pp. 1159–1173. (Cited on pages 18, 31, 41, and 81.)

Schamel, A. R., e.a. (1993). Modelling and measurement techniques for valve spring dynamics in high revving internal combustion engines. *Society of Automotive Engineering (SAE)*, vol. 03, no. 930615, pp. 820–836. (Cited on pages 18, 19, and 36.)

Shigley, J. and Mischke, C. (1989). *Mechanical Engineering Design*, p. 71. McGraw-Hill, Singapore. (Cited on pages 53 and 54.)

Simmons, C. and Maquire, D. (1995). *Manual of Engineering Drawings to British and International Standards*, p. 148. Arnold, Great Britain. (For information.)

Smith, P. (1967). *Valve Mechanisms for High-Speed Engines*, p. 138. G.T. Foulis and CO. Ltd, London. (For information.)

Smith, S. (1999). *Digital Signal Processing*. 2nd edn. California Technical Publishing, California, USA. (Cited on pages 17 and 121.)

Speckens, F.W., e.a. (1999). Marked progress in both technique and handling of valve train and valve train drive calculation on commercial platform. *Society of Automotive Engineering (SAE)*, vol. 03, no. 1999-01-056, pp. 843–850. (For information.)

Taylor, G. and Campbell, T. (1989). Design analysis of cam and tappet interaction for wear reduction in marine diesel engines. *Society of Automotive Engineering (SAE)*, vol. 03, no. 894309. (Cited on page 8.)

White, F.M. (1999). *Fluid Mechanics*, pp. 220–221. 4th edn. WCB/McGraw-Hill, Singapore. (Cited on page 57.)

Yuyi, L. (1987 December). General dynamics equations of helical springs with static solution and experimental verification coupling of substructures for dynamic analysis. *American Society of Mechanical Engineers (ASME))*, vol. 54, pp. 910–917. (For information.)

Zou, D. and McCormick, E. (1996). Dynamic model and computer simulation of valve train assemblies with hydraulic lash adjusters. *Society of Automotive Engineering (SAE)*, vol. 03, no. 960351, pp. 4.1–4.9. (Cited on pages 41, 42, 43, and 47.)

Appendices

Appendix A

DSP Theory with Fourier Analysis and Digital Filters

This chapter introduces and discusses the DSP theory used in this project. Fourier series, Fourier transforms and a digital filter were primarily applied in analysing measured data.

A.1 Fourier analysis

Fourier Analysis is a mathematical tool that allows decomposition of time domain waveforms or signals, $x(t)$, into the frequency domain represented by sinusoids. The Fourier analysis is named after the French mathematician and physicist Jean Baptiste Joseph Fourier (1768-1830). The Fourier series and Fourier integral belongs to the Fourier analysis family and will be discussed in the following sections.

A.1.1 Fourier series

Fourier was interested in heat propagation and presented a controversial paper containing claims that any continuous periodic signal could be represented as the sum of properly chosen sinusoidal waves. Fourier's main opposition to this theory came form another famous mathematician, Joseph Louis Lagrange (1736-1813). Lagrange insisted that such an approach could not be used to represent signals with discontinuous slopes, such as square waves. Lagrange was correct, but in fact, the sinusoidal representation of any periodic signal becomes accurate enough in order for the difference to contain zero energy. The phenomenon referred to as the Gibbs effect proves how accurate the Fourier series representation can be.

The Gibbs effect was explained by mathematical physicist Josiah Gibbs in 1899. Figure A.1 illustrates the effect of that using more and more modes have on a Fourier series representing a periodic square wave in the time domain .

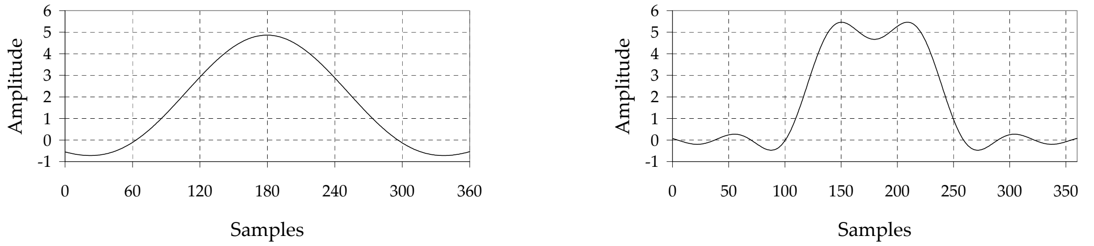

(a) Fourier series with 3 modes.

(b) Fourier series with 10 modes.

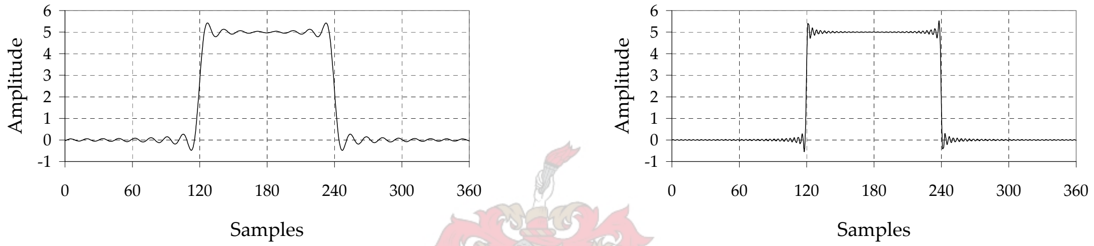

(c) Fourier series with 50 modes.

(d) Fourier series with 200 modes.

Figure A.1: Fourier series representing a square wave, illustrating the Gibbs effect.

With three or even ten modes, figure A.1(a) and A.1(b) respectively, the series does not represent the square wave realistically. The Fourier series becomes more accurate by adding more modes or frequencies of sinusoids. However, there is some overshooting and ringing at the discontinuities. The amplitude of the overshoot does not decrease as the modes or sinusoids approach infinity and remains roughly 9 percent. The width of the overshoot decreases as more modes are added to the point where it technically has zero width.

Gibbs showed that the summation converges to the signal in the sense that the error between the two has zero energy. It should be noted that the objection by Lagrange only applies to continuous signals and that for discrete signals the decomposition is mathematically exact. It is thus accepted today that any continuous periodic signal can be represented by a Fourier series.

While the signal must be periodic, it should also adhere to the Dirichlet conditions. Shortly, this states :

1. If the function $x(t)$ that represents the signal contains discontinuities, their number should be finite in any period,
2. the function $x(t)$ must contain a finite number of maxima and minima during any period, and
3. it must be possible to integrate the function $x(t)$ over any interval.

The general form of the Fourier series for any given function $x(t)$, adhering to the Dirichlet conditions, is

$$x(t) = a_0 + \sum_{n=1}^{\infty} \left(a_n cos(n\omega t) + b_n sin(n\omega t)\right) \tag{A.1}$$

where

$$f = \frac{1}{T_p} \qquad \omega = 2\pi f = \frac{2\pi}{T_p} \tag{A.2}$$

The coefficients a_0, a_n and b_n (with $n = 1, 2, 3, ...$) are given by

$$a_0 = \frac{1}{T_p}\int_0^{T_p} x(t)dt \qquad a_n = \frac{2}{T_p}\int_0^{T_p} x(t)cos(n\omega t)dt \qquad b_n = \frac{2}{T_p}\int_0^{T_p} x(t)sin(n\omega t)dt \tag{A.3}$$

The Fourier series theory of continuous signals can also be applied to signals with N discrete points. The integration of the coefficients a_0, a_n and b_n could be performed with the $\frac{1}{3}$ Simpson's rule numerical integration method. The general equation for the $\frac{1}{3}$ Simpson's rule is given by:

$$\int_b^a x(t)dt \approx \frac{h}{3}\left(x(t_0) + 4x(t_1) + 2x(t_2) + 4x(t_3) + \ldots + 2x(t_{N-2}) + 4x(t_{N-1}) + x(t_N)\right) \tag{A.4}$$

The N point discrete signal spans the interval [a, b] and divides it into uniformly spaced subintervals of size h. The size of h is given by

$$h = \frac{b-a}{N-1} \tag{A.5}$$

The $\frac{1}{3}$ Simpson's rule is a numerical method and therefore deviates from the analytical solution. The integration error is still small and limited in size to the fourth order derivative. The error is given by

$$\mid e_s \mid \leq \frac{(b-a)^5}{180\,h^4} O'''' \tag{A.6}$$

By combining the numerical analysis method of the $\frac{1}{3}$ Simpson's rule with the Fourier series theory, a MATLAB program was written and used in this project. The program's objective was to determine the spectral information of the cam lift motion by decomposing the signal representing the cam curve into its sinusoidal waves. The cam lift motion, and its spectral information, is the input function to the valve train dynamic system and therefore valuable information.

A.1.2 Fourier transforms

The Fourier integral is used to investigate the time and frequency spectra of aperiodic waveforms and is derived from the Fourier series. With the appropriate mathematical manipulation the Fourier series reduces to

$$x(t) = \int_{-\infty}^{\infty} X(f) e^{j2\pi f t} df \tag{A.7}$$

The Fourier coefficients have now become a function of continuous frequency variable f and are given by

$$X(f) = \int_{-\infty}^{\infty} x(t) e^{-j2\pi f t} dt \tag{A.8}$$

These two integrals are referred to as the Fourier transform pair, the former is known as the inverse Fourier transform and the latter as the direct Fourier transform. Fourier transform theory is only applicable on signals with infinite period. A signal given by the function $x(t)$ and subjected to the Dirichlet conditions, can be transformed from a function in time to a function of frequency, $X(f)$ using the direct Fourier transform.

The direct and inverse Fourier transforms are difficult to apply directly without tools. One tool used in this project was the Discrete Fourier Transform, or DFT. The task of applying a Fourier transform requires the evaluation of a closed-form integral. To apply this to digital computers, a numerical integration must be used. There are three distinct problems with computing a Fourier transform digitally.

Firstly, the desired result is a continuous function and a digital solution will only be able to calculate the solution at discrete points. Secondly, the evaluation of the actual integral is a problem. This is calculated numerically by adding together areas of narrow rectangles under the curve (i.e. the $\frac{1}{3}$ Simpson's rule). The last problem is that the result can not be calculated with infinite samples. In DSP, signals and waveforms are measured as finite and discrete signals. Thus, it should be remembered that when using the DFT, only an approximation of the original Fourier transform results.

By using equation A.8 and applying Euler's relation on it, namely $e^{jx} = cosx + j\,sinx$, and separating the real and imaginary parts, we have the analysis equations for the DFT.

$$Re\,X(f) = \int_{-\infty}^{\infty} x(t)cos(2\pi f t)dt \tag{A.9}$$

$$Im\,X(f) = -\int_{-\infty}^{\infty} x(t)sin(2\pi f t) \tag{A.10}$$

Expressing these equations in terms of discrete samples and using numerical integration, the DFT analysis equations used in a MATLAB program in this project were

$$Re\,X[i] = \sum_{n=0}^{N-1} x[n]cos(2\pi in/N) \tag{A.11}$$

$$Im\,X[i] = -\sum_{n=0}^{N-1} x[n]sin(2\pi in/N) \tag{A.12}$$

Index i runs from 0 to $N-1$ and index k runs from 0 to $N/2$.

The discrete Fourier transform changes a N point time domain signal into two $N/2+1$ point output signal. (N could be any positive integer, but a power of two is usually chosen, i.e., 128, 256, 512, etc.) The output signals, $Re\,[\,]$ and $Im\,[\,]$, contain the amplitudes of the component cosine and sine waves respectively.

The horizontal axis of the frequency domain can be referred to in four different ways. It can either be expressed as the sample numbers, a fraction of the sampling frequency (between 0 and 0,5), multiplying the fraction of the sampling frequency by 2π and having the index ω, or natural frequency (between 0 and π radians), or finally expressing it in the analog frequencies used in the particular application. The last mentioned method is used in this project for it presents the frequency data in real world meaning.

The sine and cosine wave notation is called the rectangular notation. The frequency domain was converted into polar notation, consisting of the magnitude and the phase parts, in this project. This was done to have a better visual understanding of the frequency domain. Polar notation directly represents signals in terms of the amplitude and phase of the component cosine waves (Smith (1999)).

$Re\,[\,]$ and $Im\,[\,]$ are replaced by $Mag\,[\,]$ and $Phase\,[\,]$. Both pairs contain the same information and in equation form the two representations are related by

$$A\,cos x + B\,sin x = M\,cos(x+\theta) \tag{A.13}$$

A.1.3 Digital filters

Digital filters can be used to separate combined signals, such as in the case of making sense of noisy measured signals or distinguishing between different harmonic frequencies. The filter used in this project will now be discussed in this section.

Digital filters are carried out by standard convolution. Convolution is the mathematical method of combining two signals to form a third. Convolution is a mathematical operation, such as addition and multiplication. It is the single most important technique in DSP and provides the framework for it. Unfortunately, the explanation of convolution goes beyond the scope of this project and is not discussed further.

Figure A.2 illustrates the concept behind the low-pass filter used. In figure A.2(b) the frequency response of the ideal filter is illustrated. All frequencies below the cut-off frequency, f_c (in this case f_c is 25 % of the sampling frequency, f_s), are passed with unit amplitude and all frequencies above it are blocked.

When taking the inverse Fourier transform of this ideal frequency response, the ideal filter kernel is produced, illustrated in figure (A.2(a)). This curve is referred to as the sinc function and has the general form of $sin(x)/x$. For discrete signals it is given by

$$h[i] = \frac{sin(2\pi f_c i)}{i\pi} \tag{A.14}$$

The sinc function continues to both positive and negative infinity without dropping to zero amplitude. To solve this problem the sinc function is truncated to $M+1$ points, symmetrically chosen around the main lobe, with M being any even number. All samples outside this $M+1$ points are set to zero or ignored. Secondly, the function is shifted to the right by $M/2$ points so that the kernel runs from 0 to M. It is now represented as positive indexes only (refer to figure A.2(c)).

M is chosen arbitrarily and this causes the truncated function to end abruptly and become discontinuous at the point of truncation. To solve this, the signal is multiplied by a Blackman window (figure A.2(d)) to smooth the kernel. The result is the windowed-sinc filter kernel, figure A.2(e). Figure A.2(f) shows the frequency response of the windowed-sinc filter.

In designing the windowed-sinc filter for a specific application, two parameters should be selected; the cutoff frequency, f_c, and the length of the filter, M. The cutoff frequency is expressed as a fraction of the sampling rate and therefore must be between 0 and 0,5. The value of M sets the frequency roll-off according to the approximation

$$M \approx \frac{4}{BW} \tag{A.15}$$

BW is the width of the transition band, measured from where the curve in figure A.2(f) just leaves one to where it almost reaches zero. Thus, the filter length, M, directly determines how sharp the filter will cut off frequencies. Figure A.2(g) and A.2(h) illustrates the effect the filter length has on the roll-off bandwidth. In essence, the more points used in the filter kernel, the narrower the bandwidth becomes, which improves the filter performance. High M values do have a computation time penalty and designing filters are usually a trade-off between filter sharpness and computation time.

In this project the windowed-sinc filter was used in order to pass the useful frequencies of acceleration measurements and cut the higher, noisy frequencies off.

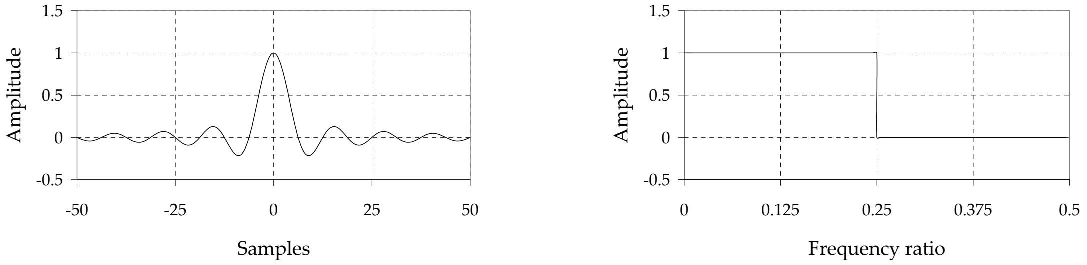

(a) The sinc function and ideal filter kernel.

(b) Ideal filter kernel frequency response.

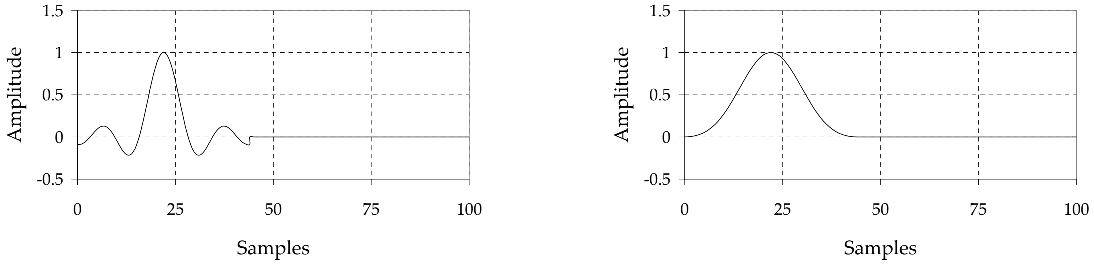

(c) The sinc function truncated and shifted. M=44.

(d) Blackman window for smoothing truncated sinc function.

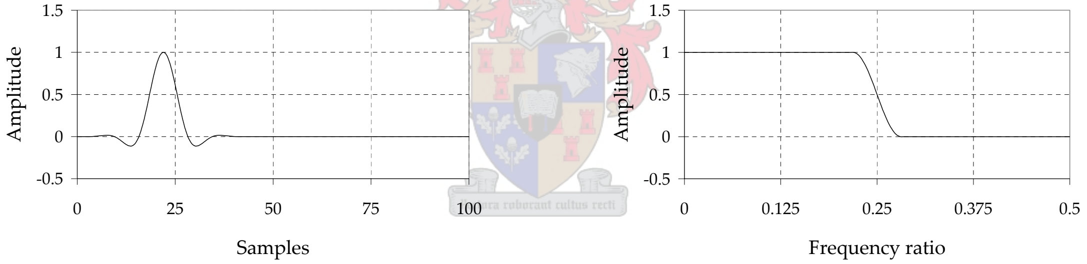

(e) The windowed-sinc filter.

(f) Windowed-sinc filter frequency response.

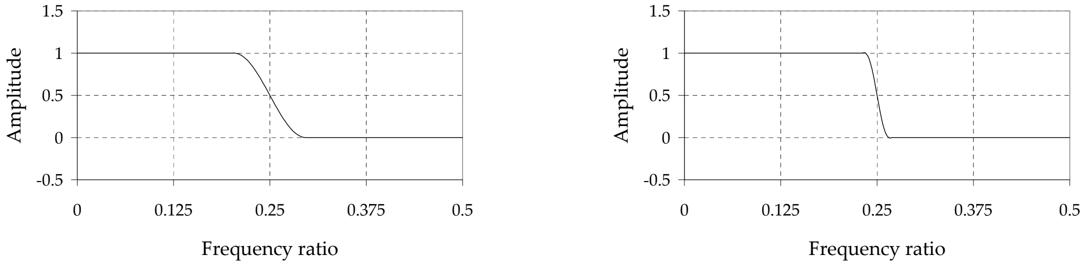

(g) Filter length halved, $M = 22$.

(h) Filter length doubled, $M = 88$.

Figure A.2: Illustration of the low-pass filter concept.

Appendix B

Discrete Taylor Differentiation

One method of performing differentiation numerically is the forward-difference formula. The formula being discussed here is the three point forward-difference formula. The formula is derived by using a central-difference formula. The central-difference formula is calculated from two Taylor series expansions of the functions around points $x(t_i + h)$ and $x(t_i - h)$.

Recall from calculus that the Taylor series of a given function $x(t)$ about a chosen point t_0 is defined as the infinite series

$$\begin{aligned} x\,|_{t_0} &= x(t_0) + \frac{\dot{x}(t_0)}{1!}(t - t_0) + \frac{\ddot{x}(t_0)}{2!}(t - t_0)^2 + ... \\ &= \sum_{0}^{\infty} \frac{x^n(t_0)}{n!}(t - t_0)^n \end{aligned} \tag{B.1}$$

By simplifying this expression, including the error of estimation, and defining $h = x_{i+1} - x_i$ for evenly spaced discrete data, we have

$$x(t_i) = x(t_i) + \dot{x}(t_i)(h) + \ddot{x}(t_i)\frac{h}{2} + O'''\frac{h^3}{3!} \tag{B.2}$$

Similarly to equation B.2 for the Taylor series expansion of $x(t)$, the Taylor series expansion is derived for $x(t_i + h)$ and $x(t_i - h)$.

$$\begin{aligned} x(t_i + h) &= x(t_i) + \dot{x}(t_i)h + \ddot{x}(t_i)\frac{h}{2} + O'''\frac{h^3}{3!} \\ x(t_i - h) &= x(t_i) - \dot{x}(t_i)h + \ddot{x}(t_i)\frac{h}{2} - O'''\frac{h^3}{3!} \end{aligned} \tag{B.3}$$

By subtracting the two Taylor series expansions of equation B.3 from each other and writing $x(t_i + h)$ and $x(t_i - h)$ as x_{i+1} and x_{i-1} respectively, we have the first order, discrete Taylor derivative, $\dot{x}(t)$.

$$\dot{x}_i = \frac{x_{i+1} - x_{i-1}}{2h} - O''' \frac{h^2}{6} \tag{B.4}$$

This formula is sometimes called the *three point formula* because of the use of three data points. Proceeding in a similar fashion, the three point forward-difference formula for $\ddot{x}(t)$ is found to be (without the error term)

$$\ddot{x}_i = \frac{x_i - 2x_{i+1} + x_{i+2}}{h^2} \tag{B.5}$$

The velocity and acceleration of discrete, evenly-spaced displacement data, could be calculated with equations B.4 (ignoring the error term) and B.5.

Appendix C

Wheatstone Bridge

When an element is connected between point *b* and *d* in the circuit shown in figure C.1, the element is said to bridge the two branches. This particular circuit, called the *Wheatstone bridge*, is very useful in measurement systems. It provides the most accurate technique for measuring the value of electrical resistance (Boctor, 1997).

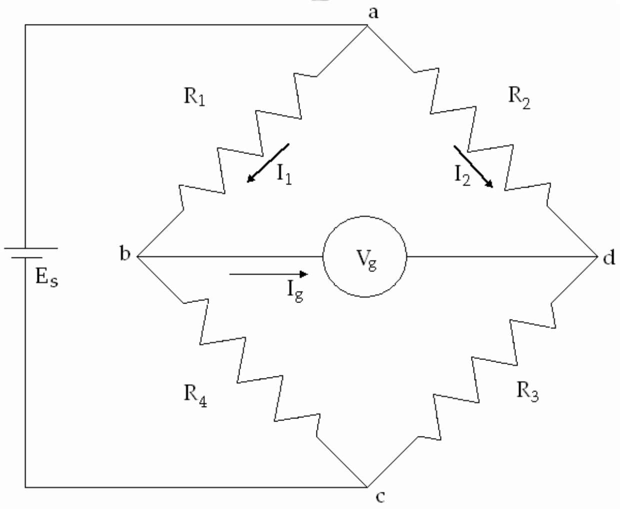

Figure C.1: Wheatstone bridge arrangement.

The situation corresponding to zero current flow in the bridge arm, I_g, is called the *bridge balance condition*. Under this condition, current I_1 flows in resistors R_1 and R_4, while current I_2 flows in resistors R_2 and R_3. Thus resistors R_1 and R_4 are in series, as is resistors R_2 and R_3. These two series branches are in parallel with the voltage source E_s.

Using KVL, we have

$$\begin{aligned} V_{db} &= V_{dc} - V_{bc} \\ &= I_2 R_3 - I_1 R_4 \\ &= \frac{E_s}{R_2 + R_3} R_3 - \frac{E_s}{R_1 + R_4} R_4 \end{aligned} \tag{C.1}$$

At bridge balance condition, $V_{db} = 0$, thus we have

$$\frac{R_3}{R_2 + R_3} = \frac{R_4}{R_1 + R_4} \tag{C.2}$$

Inverting each side of this equation and simplifying yields the *touching arm ratio*.

$$\frac{R_2}{R_3} = \frac{R_1}{R_4} \tag{C.3}$$

Appendix D

Flow between Parallel Plates

Consider the two dimensional incompressible plane ($\partial/\partial z = 0$) viscous flow between two parallel plates a distance h_g apart, as shown in figure D.1. The assumption is that the flow is essentially axial, $u \neq 0$ but $v = w = 0$.

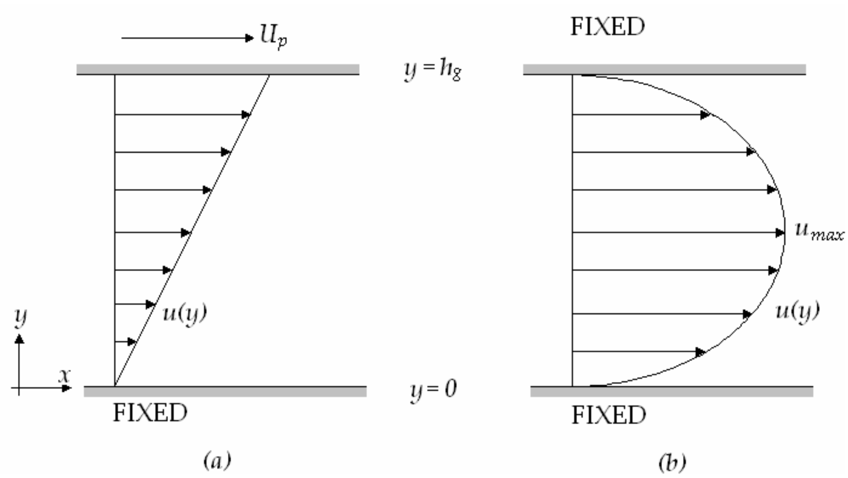

Figure D.1: Flow between parallel plates caused by (a) a moving upper boundary wall, and (b) a pressure gradient.

In the case of flow through the annular slot created by the gap between the plunger and the housing, the flow could be divided into two cases. Firstly, the case where there is no pressure gradient, but the upper plate is moving at velocity of U_p, and secondly, where there is no relative wall velocity between the plates, but the fluid flow is driven by a pressure drop, *dp/dx*.

Two of the basic differential equations for fluid motion are the continuity and momentum equation:

$$\frac{\partial \rho}{\partial t} + \boldsymbol{\nabla} \cdot (\rho \boldsymbol{V}) = 0 \tag{D.1}$$

$$\rho \frac{d\boldsymbol{V}}{dt} = \rho g - \boldsymbol{\nabla} p + \boldsymbol{\nabla} \cdot \tau_{ij} \tag{D.2}$$

Flow with constant ρ and μ_{mix} is a basic simplification. The above two equations of motion reduces to

$$\boldsymbol{\nabla} \cdot \boldsymbol{V} = 0 \tag{D.3}$$

$$\rho \frac{d\boldsymbol{V}}{dt} = \rho g - \boldsymbol{\nabla} p + \mu_{mix} \nabla^2 \boldsymbol{V} \tag{D.4}$$

From the continuity equation, equation D.3, we have

$$\frac{\partial u}{\partial x} + \frac{\partial v}{\partial y} + \frac{\partial w}{\partial z} = \frac{\partial u}{\partial x} + 0 + 0 = 0 \quad \text{or} \quad u{=}u(y) \text{ only} \tag{D.5}$$

Thus, there is a single non-zero axial velocity component that varies only across the width of the channel when the flow is said to be fully developed. Substituting $u{=}u(y)$ into the momentum equation (equation D.4) for two dimensional (x, y) flow we have:

$$\rho \left(u \frac{\partial u}{\partial x} + v \frac{\partial v}{\partial y} \right) = \rho g - \left(\frac{\partial p}{\partial x} + \frac{\partial p}{\partial y} \right) + \mu_{mix} \left(\frac{\partial^2 u}{\partial x^2} + \frac{\partial^2 u}{\partial y^2} \right) \tag{D.6}$$

Most of the terms drop out and the momentum equation is reduced to

$$\frac{d^2 u}{dy^2} = 0 \qquad \text{or} \qquad u = C_1 y + C_2 \tag{D.7}$$

The two constants, C_1 and C_2, are found by applying the no-slip condition at the upper and lower plates.

At $y = 0$ $\qquad u = 0 = C_2$

At $y = h_g$ $\qquad u = U_p = C_1 h_g$

$$C_1 = \frac{U_p}{h_g} \qquad \text{and} \qquad C_2 = 0 \tag{D.8}$$

Therefore the solution for flow between plates with a moving upper wall and no pressure gradient, is

$$u = y\frac{U_p}{h_g} \qquad 0 \leq y \leq h_g \tag{D.9}$$

This is *Couette* flow due to a moving wall; a linear velocity profile with no-slip at each wall, as anticipated and sketched in figure D.1(a).

For the second case of flow between parallel plates, where there is no relative wall velocity between the plates, the fluid flow is driven by a pressure drop, *dp/dx* (refer to figure D.1(b)). Pressure varies in the x-direction, but velocity U_p is zero. If $v = w = 0$, the continuity equation leads to the same conclusion as in the first case, namely, that $u = u(y)$. The momentum equation (equation D.4) for two dimensional flow changes only because the pressure is varying.

$$\mu_{mix}\frac{d^2u}{dy^2} = \frac{\partial p}{\partial x} + \frac{\partial p}{\partial y} = \frac{dp}{dx} \qquad \left(\frac{\partial p}{\partial y} = 0\right) \tag{D.10}$$

As in equation D.7, the solution is accomplished by double integration:

$$u = \frac{1}{\mu_{mix}}\left(\frac{dp}{dx}\right)\frac{y^2}{2} + C_1 y + C_2 \tag{D.11}$$

Again, the two constants are found by applying the no-slip condition at the upper and lower plates.

At $y = 0$ $\qquad u = 0 = C_2$

At $y = h_g$ $\qquad u = 0 = \frac{1}{\mu_{mix}}\left(\frac{dp}{dx}\right)\frac{h_g^2}{2} + C_1 h_g$

$$C_1 = \frac{U_p}{h_g} \qquad \text{and} \qquad C_2 = 0 \tag{D.12}$$

Therefore the solution for flow between plates with a pressure gradient and no moving upper wall, is

$$u = \frac{1}{2\mu_{mix}}\left(\frac{dp}{dx}\right)(y^2 - yh_g) \tag{D.13}$$

This flow forms a *Poiseuille* parabola of constant negative curvature. The maximum velocity occurs at the centerline $y = h_g/2$.

To calculate the volume flow rate due to the fluid motion, $\dot{Q}_{moving}$, the solution for the flow velocity (equation D.9) is integrated over the height of the annular slot and multiplied by the width, b:

$$\begin{aligned}\dot{Q}_{moving} &= \int_0^{h_g} u(y)b\,dy \\ &= \frac{U_p}{h_g} b \int_0^{h_g} y\,dy \\ &= U_p h_g \frac{b}{2}\end{aligned} \tag{D.14}$$

The calculation of the annular slot width, b, needs consideration of the height at which fluid flow momentum would be balanced. In the case of the *Couette* flow, (figure D.1(a)), resultant momentums would be balanced at a height of $\frac{2}{3}h_g$. (Analogous to the centre point of gravity of a right angle triangle). Thus, the width of the annular slot is calculated to be

$$b = 2\pi R = 2\pi(r_p + \frac{2}{3}h_g) \tag{D.15}$$

where r_p is the outside radius of the plunger in the case of the HLA. Substituting equation D.15 into the solution of equation D.14, the first part of equation 5.3.10's volume flow rate is found to be

$$\dot{Q}_{moving} = \pi U_p h_g \left(r_p + \frac{2}{3}h_g \right) \tag{D.16}$$

Similarly, to calculate the volume flow rate due to the pressure gradient, $\dot{Q}_{prsgrad}$, the solution for the flow velocity (equation D.13) is integrated over the height of the annular slot.

$$\begin{aligned}\dot{Q}_{prsgrad} &= \int_0^{h_g} u(y)b\,dy \\ &= \frac{1}{2\mu_{mix}} \left(\frac{dp}{dx} \right) b \int_0^{h_g} (y^2 - y h_g)\,dy \\ &= -\frac{h_g^3}{6\mu_{mix}} \left(\frac{dp}{dx} \right) \frac{b}{2}\end{aligned} \tag{D.17}$$

The calculation of the annular slot width, b, again needs consideration of the height at which fluid flow momentum would be balanced. In the case of the *Poiseuille* flow, (figure D.1(b)), resultant momentums would be balanced at the centre of the gap. Thus, the width of the annular slot is calculated to be

$$b = 2\pi R = 2\pi(r_p + \frac{h_g}{2}) \tag{D.18}$$

Substituting equation D.18 into D.17 the second part of equation 5.3.10's volume flow rate is found.

$$\dot{Q}_{prsgrnd} = -\frac{\pi}{6\mu_{mix}} h_g^3 \left(\frac{dp}{dx}\right) \left(r_p + \frac{h_g}{2}\right) \tag{D.19}$$

By adding the volume flow rate contributions from equations D.16 and D.19 together, the volume flow rate of oil passing through the annular slot caused by the gap between the plunger and housing, $\dot{Q}_{pas}$ (equation 5.3.10), is found.

$$\dot{Q}_{pas} = \pi U_p h_g \left(r_p + \frac{2}{3} h_g\right) - \frac{\pi}{6\mu_{mix}} {h_g}^3 \left(\frac{dp}{dx}\right) \left(r_p + \frac{h_g}{2}\right)$$

Appendix E

Valve Train Components Details

Table E.1: Breakdown of valve train components.

Component	m	ρ	I		
			I_{xx}	I_{yy}	I_{zz}
	$[kg]$	$[kg/mm^3]$	$[kg/mm^2]$	$[kg/mm^2]$	$[kg/mm^2]$
Inlet valve seat	1.349E-02	7.850E-06	2.644	2.644	5.197
Inlet valve	5.000E-02	7.461E-06	5.495	54.81	54.81
Valve guide	2.772E-02	7.850E-06	8.396	4.223	4.223
Spring retainer	6.000E-03	6.339E-06	0.154	0.154	0.276
HLA oil base	1.432E-02	7.137E-06	0.389	1.052	1.052
HLA oil reservoir	7.675E-03	7.137E-06	0.087	0.562	0.562
Camshaft assembly	3.697E-01	7.850E-06	30.94	271.8	273.6
Finger follower assembly	7.604E-02	7.970E-06	4.207	0.562	0.562
Spring	3.400E-02	7.375E-06	4.214	8.315	8.323

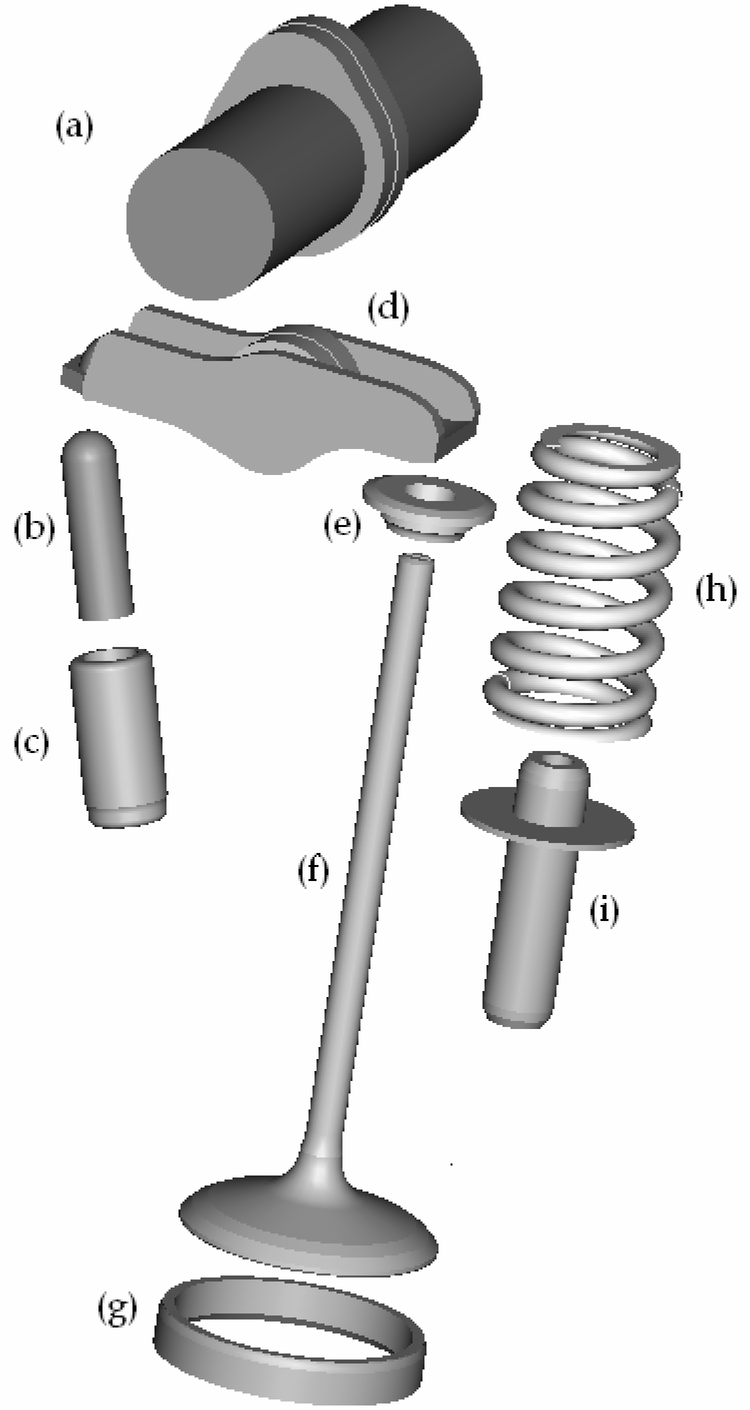

Figure E.1: Exploded view of the complete valve train model assembly. (a) camshaft assembly, (b) HLA oil reservoir, (c) HLA oil base, (d) finger follower assembly, (e) spring retainer, (f) inlet valve, (g) inlet valve seat, (h) spring and (i) valve guide.

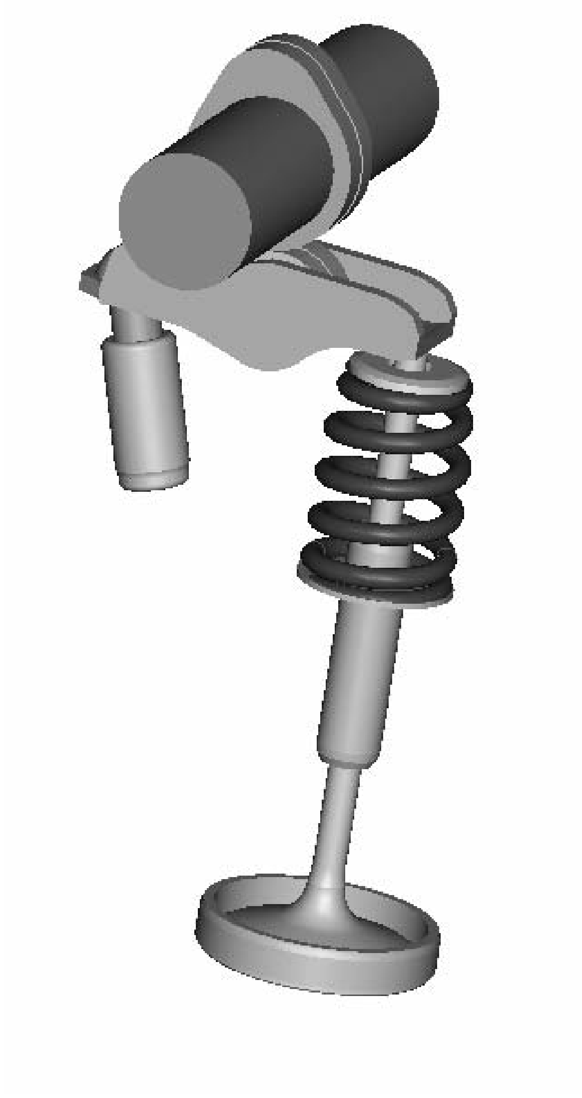

Figure E.2: Assembled view of the complete valve train model assembly (with compressed spring).

Appendix F

Constant Strain Triangle and Linear Strain Triangle Plane Elements

FE theory makes extensive use of stress-strain relations. These are used to obtain a strain field from a displacement field. Referring to figure F.1 we have

$$\epsilon_x = \frac{\triangle u}{\triangle x} \qquad \epsilon_y = \frac{\triangle v}{\triangle y} \qquad \gamma_{xy} = \frac{\triangle u}{\triangle y} + \frac{\triangle v}{\triangle x} \tag{F.1}$$

for small strains and rotations.

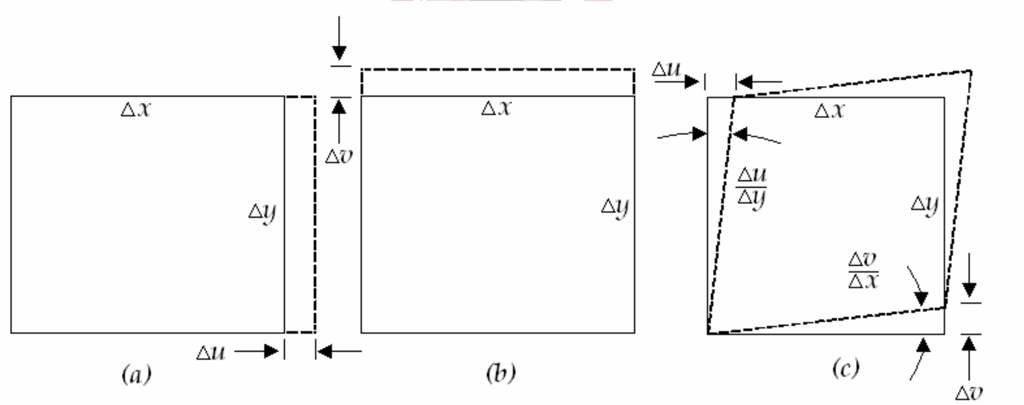

Figure F.1: A rectangle of incremental size subjected to (a) x-direction strain, (b) y-direction strain, and (c) shear strain.

In a plane problem the x-direction displacement, u, and the y-direction displacement, v, are both functions of coordinates $u = u(x, y)$ and $u = u(x, y)$. This constitutes the use of partial derivatives. Doing so, and passing to the limit, we write

$$\epsilon_x = \frac{\partial u}{\partial x} \qquad \epsilon_y = \frac{\partial v}{\partial y} \qquad \gamma_{xy} = \frac{\partial u}{\partial y} + \frac{\partial v}{\partial x} \tag{F.2}$$

Referring to figure F.2, the x- and y-direction components of the displacement of an arbitrary point within the CST are restricted to be a linear polynomial in x and y.

$$u = \beta_1 + \beta_2 x + \beta_3 y \tag{F.3a}$$

$$y = \beta_4 + \beta_5 x + \beta_6 y \tag{F.3b}$$

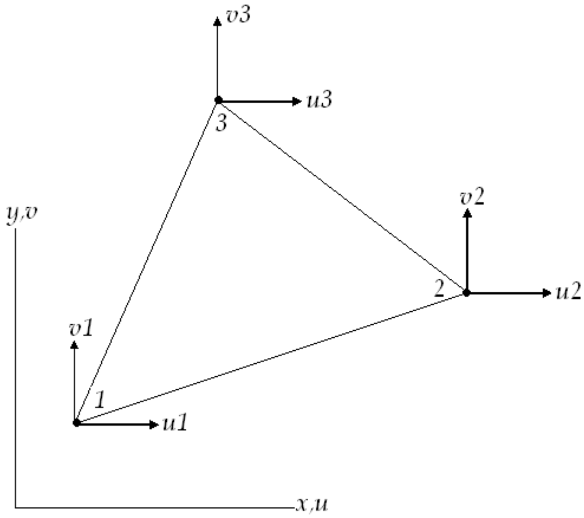

Figure F.2: Constant strain triangle (CST).

where the β_i are called the *generalised coordinates*. The general coordinates can be described as displacement amplitudes. For example, in equation F.3a, β_1 is the rigid-body displacement, and β_2 and β_3 are amplitudes of linearly varying displacements, all in the x-direction.

Expressing β_i in terms of nodal displacements u_1, v_1, u_2, v_2, u_3 and v_3, the following substitutions are made in equation F.3, again referring to figure F.2.

$$\begin{array}{llllllll} u = u_1 & \text{and} & v = v_1 & \text{at} & x = 0 & \text{and} & y = 0 \\ u = u_3 & \text{and} & v = v_2 & \text{at} & x = a & \text{and} & y = 0 \\ u = u_3 & \text{and} & v = v_3 & \text{at} & x = 0 & \text{and} & y = b \end{array} \tag{F.4}$$

By solving the resulting six equations for u_1, v_1, u_2, v_2, u_3 and v_3, the alternative form for equation F.3 is found to be

$$u = (1 - \frac{x}{a} - \frac{y}{b})u_1 + \frac{x}{a}u_2 + \frac{y}{b}u_3 \tag{F.5a}$$

$$v = (1 - \frac{x}{a} - \frac{y}{b})u_1 + \frac{x}{a}v_2 + \frac{y}{b}v_3 \tag{F.5b}$$

In either equation F.3 or F.5, the displacement field $u = u(x, y)$ and $u = u(x, y)$ has six d.o.f.. The six β_i in equation F.3 and the three u_i and the three v_i in F.5. Substituting equation F.3 into F.2 the strain-displacement relations for the CST is found to be

$$\begin{aligned} \epsilon_x &= \tfrac{\partial u}{\partial x} \quad \text{hence} \quad \epsilon_x = \beta_2 \\ \epsilon_y &= \tfrac{\partial v}{\partial y} \quad \text{hence} \quad \epsilon_y = \beta_6 \\ \gamma_{xy} &= \tfrac{\partial u}{\partial y} + \tfrac{\partial v}{\partial x} \quad \text{hence} \quad \gamma_{xy} = \beta_3 + \beta_5 \end{aligned} \tag{F.6}$$

As shown in equation F.4, none of the strains vary over the element and therefore the name of *constant strain triangle*. The physical consequence is that the element is too stiff in bending because an applied bending moment is resisted by spurious shear stress as well as by the expected flexural stresses. The element can thus not represent the linear strain field of pure bending.

The LST is shown in figure F.3. It consists of mid-side nodes in addition to vertex nodes. The d.o.f. are u_i and v_i at each node for a total of 12 d.o.f.

In terms of the generalised coordinates β_i its displacement field is

$$u = \beta_1 + \beta_2 x + \beta_3 y + \beta_5 x^2 + \beta_5 xy + \beta_6 y^2 \tag{F.7a}$$

$$v = \beta_7 + \beta_8 x + \beta_9 y + \beta_{10} x^2 + \beta_{11} xy + \beta_{12} y^2 \tag{F.7b}$$

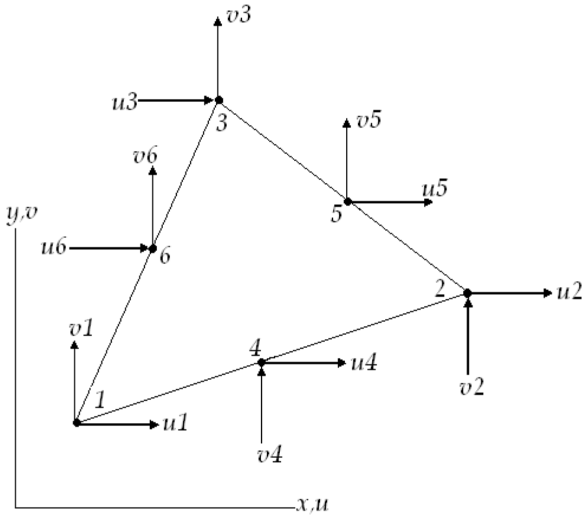

Figure F.3: Linear strain triangle (LST).

and from equation F.2, the resulting strain field is

$$\begin{aligned} \epsilon_x &= \beta_2 + 2\beta_4 x + \beta_5 y \\ \epsilon_y &= \beta_9 + \beta_{11} x + 2\beta_{12} y \\ \gamma_{xy} &= (\beta_3 + \beta_8) + (\beta_5 + 2\beta_{10})x + (2\beta_6 + \beta_{11})y \end{aligned} \tag{F.8}$$

The strain field can vary linearly with x and y within the element, hence the name *linear strain triangle*. The LST can be used to obtain exact solutions for deflection and stress of pure bending problem.

Appendix G

FE Spring Model Properties

Table G.1: Detail spring model discretisation.

Section	Linearisation Force [N]	Section stiffness [N/mm]	Section mass [10^{-3} kg]
1	96	2733.65	2.94
2	176	481.44	1.22
3	288	383.97	1.25
4	512	478.27	1.33
5	576	528.08	1.33
6	656	606.05	1.36
7	672	617.74	1.40
8	704	643.23	1.41
9	672	613.53	1.41
10	640	584.50	1.41
11	672	608.48	1.41
12	704	643.28	1.41
13	720	654.75	1.41
14	640	589.40	1.41
15	624	570.62	1.41
16	704	639.72	1.41
17	768	690.72	1.41
18	768	673.72	1.41
19	752	678.76	1.41
20	480	603.78	1.41
21	288	680.83	1.41
22	256	3789.34	3.42

Table G.2: Equivalent model beam element properties.

Section	Element length [mm]	Sectional area [$10^{-3} mm^2$]	Element density [10^{-3} kg/mm^3]
1	2.36	29.34	42.44
2	1.32	2.88	322.34
3	1.71	2.98	245.97
4	2.01	4.36	151.50
5	2.03	4.86	134.61
6	2.03	5.58	120.74
7	2.02	5.69	121.75
8	2.03	5.92	117.87
9	2.03	5.65	123.58
10	2.03	5.38	129.70
11	2.02	5.60	124.61
12	2.03	5.92	117.86
13	2.03	6.03	115.78
14	2.03	5.43	128.63
15	2.02	5.25	132.88
16	2.03	5.89	118.52
17	2.03	6.36	109.76
18	2.03	6.20	112.53
19	2.00	6.16	114.87
20	1.68	4.62	182.11
21	1.29	3.99	274.12
22	2.29	39.45	37.90